JOINT INSTITUTE FOR NUCLEAR RESEARCH

The Report on Project
“MPD. MultiPurpose Detector”

<u>02-0-1065-2007/2023</u>

LEADER *V.M.Golovatyuk, V.D.Kekelidze*

Submitted

LHEP Science and Technology Council

THE LIST OF PARTICPANTS FROM JINR AND MEMBER-STATES

Joint Institute for Nuclear Research, Dubna, RUSSIA (FTE=114)

K.Afanaciev, S.Afanaciev, G.Agakishiev, S.Andreeva, T.Andreeva, N.Anfimov, A.Aparin, V.Astakhov, G.Averichev, A.Averyanov, V.Babkin, I.Balashov, M.Barabanov, D.Baranov, A.Baskakov, P.Batuyk, A.Bazhazhin, S.Bazylev, A.Belyaev, E.Belyaeva, D.Blaschke, D.Bogoslovsky, I.Boguslavski, M.Buryakov, A.Butenko, A.Butorin, S.Buzin, V.Chalyshev, V.Cheplakova, V.Chepurnov, Vl.Chepurnov, G.Cheremukhina, P.Chumakov, B.Dabrovska, D.Dementiev, V.Didishko, A.Dmitriev, V.Dodokhov, A.Dolbilov, D.Dąbrowski, D.Donetz, A.Drapeza, A.Dubrovin, P.Dulov, N.Dunin, V.Dunin, V.Dziatlau, A.Efremov, D.Egorov, E.Streletskaya, V.Elsha, N.Emelianov, O.Fateev, Y.Fedotov, J.Fedotova, A.Fedunin, I.Filippov, M.Gaganova, O.Gavrishuk, S.Gerasimov, K.Gertsenberger, V.Golovatyuk, N.Gorbunov, A.Guskov, A.Isupov, A.Ivanov, V.Jejer, S.Kakurin, M.Kapishin, L.Kartashova, A.Kechechyan, G.Kekelidze, V.Kekelidze, G.Khodzhibagiyan, V.Kireyeu, Y.Kiriushin, I.Kiryutin, A.Kolesnikov, V.Kolesnikov, A.Kolozhvari, V.Komarov, A.Kovalenko, V.Kramarenko, L.Krasnova, Y.Krechetov, I.Kruglova, S.Kukarnikov, S.Kuklin, R.Lednicky, A.Litomin, A.Litvinenko, E.Litvinenko, G.Litvinova, V.Lobanov, Y.Lobanov, S.Lobastov, A.Loseu, J.Lukstins, D.Madigozhin, V.Maksimenkova, A.Malakhov, I.Malikov, L.Malinina, D.Melnikov, S.Mertz, I.Meshkov, V.Mialkovski, I.Migulina, Y.Minaev, S.Mituxin, N.Molokanova, I.Moshkovskiy, A.Moskovsky, S.Movchan, A.Mudrokh, Y.Murin, G.Musulmanbekov, A.Nechaevskiy, V.Nikitin, I.Olexs, A.Olshevski, O.Orlov, S.Pargicky, V.Pavlyukevich, V.Penkin, V.Peresedov, E.Pervyshina, M.Peryt, D.Peshekhonov, A.Pilyar, S.Piyadin, A.Potanina, Y.Potrebenikov, D.Prahina, S.Razin, N.Ridinger, O.Rogachevsky, V.Rogov, K.Roslon, M.Rumyantsev, A.Rybakov, Z.Sadygov, V.Samsonov, C.Ceballos Sanchez, A.Savenkov, S.Savitskiy, T.Semchukova, A.Semenov, I.Semenova, S.Sergeev, N.Sergeeva, E.Serochkin, A.Shabunov, B.Shchinov, A.Shchipunov, A.Sheremetiev, A.Sheremetieva, M.Shitenkov, K.Shtejer Diaz, A.Shunko, A.Shutov, V.Shutov, A.Sidorin, A.Skulkin, I.Slepnev, V.Slepnev, I.Slepov, A.Sorin, T.Strizh, N.Sukhov, S.Sukhovarov, N.Surkov, V.Svalov, N.Tarasov, V.Tchekhovski, A.Terletskiy, O.Teryaev, V.Tikhomirov, A.Timoshenko, V.Toneev, N.Topilin, V.Trofimov, G.Trubnikov, I.Tyapkin, S.Udovenko, V.Vasendina,S.Vereshagin, N.Vladimirova, N.Vlasov, A.Vodopyanov, S.Volgin, O.Volodina, A.Voronin, G.Yarigin, V.Yurevich, M.Zaiceva, N.Zamyatin, S.Zaporozhets, A.Zinchenko, D.Zinchenko, V.Zruyev, A.Zubarev

A.I.Alikhanyan National Science Laboratory, ARMENIA

H.Grigorian, A.Ayriyan, V.Abgaryan, A.Piloyan

National Nuclear Research Center, AZERBAIJAN

A.Rustamov, R.Satarov

University of Plovdiv, BULGARIA

B.Dabrowska, P.Dulov, N.Geraksiev, M.Ilieva, D.Suvarieva, V.Tcholakov, L.Yordanova

Universidad Tecnica Federico Santa Maria, Valparaiso, CHILE

S.Kovalenko, S.Kuleshov, L.L.N.Paredes, R.R.Caballero, E.F.R.Calderon, P.A.U.Poblete, N.V. Maria, J.A.Zamora Saa

Central China Normal University, CHINA

F.Liu, X.Sun, Y.Wang

Huzhou University, CHINA

F.Wang, J.Wang, X.Zhu

Institute of High Energy Physics, CHINA

M.Huang, M.Wei, K.Xu

Institute of Modern Physics of the Chinese Academy of Sciences, Lanzhou, CHINA

Z.Li, X.Niu, Y.Wang , N.Xu, H.Yang, Yapeng Zhang, Yuezhao Zhang, C.Zhao, W.Zhou

Shandong University, CHINA

C.Feng, J.Jiao, Q.Xu, C.Yang, D.Liu

Fudan University, CHINA

Y.Ma, D.Fang, W.He

Three Gorges University, CHINA

S.Feng, K.Wu, X.Yuan, S.Li

Tsinghua University, Beijing, CHINA

Z.Deng, G.Gong, B.Guo, D.Han, Y.Huang, Y.Li, H.Miao, C.Shen, Y.Wang, Z.Xiao, Z.Xu, X.Zhu, P.Zhuang, Z.Zou

University of South China, CHINA

X.Wang

University of Science and Technology of China, Hefei, CHINA

Z.Tang, W.Zha, Z.Li, P.Lu

Nuclear Physics Institute of Czech Academy of Sciences, CZECH Republic

A.Kugler, V.Kushpil, S.Kushpil, V.Mikhaylov, O.Svoboda, P.Tlusty

Palacky University, Olomouc, CZECH Republic

J.Kvita, M.Maslan, L.Nožka, T.Rössler

Tbilisi State University, Tbilisi, GEORGIA

T.Babutsidze, G.Kachlishvili, A.Machavariani, M.Nioradze, R.Shanidze

Benemérita Universidad Autónoma de Puebla, MEXICO

E.Moreno Barbosa, M.Rodríguez Cahuantzi, G.Tejeda Muñoz, V.Z.Reyna Ortíz, C.H.Zepeda Fernández

Centro de Investigación y de Estudios Avanzados, MEXICO

M.A.Ayala Torres, L.M.Montaño Zetina, M.A.Fontaine Sánchez

Instituto de Ciencias Nucleares de la Universidad Nacional Autónoma de México, MEXICO

M.Alvarado, A.Ayala, W.Bietenholz , L.Díaz, M.E.Patiño

Universidad Autónoma de Sinaloa, MEXICO

I.Domínguez Jiménez, P.A.Nieto Marín

Universidad de Colima, MEXICO

M.E.Tejeda-Yeomans

Universidad de Sonora, MEXICO

L.Valenzuela Cazares, A. Guirado Garcia, J. C.Maldonado Gonzalez, I.A.Maldonado Cervantes, L.Rebolledo, E.Cuautle

Institute of Applied Physics, Chisinev, MOLDOVA

M.Baznat, D.Baznat, A.Khvorostukhin

Jan Kochanowski University, POLAND

P.Kankiewicz, M.Rybczynski, G.Stefanek, Z.Wlodarczyk

National Center for Nuclear Reseach, Otwock – Swierk, POLAND

A.Bancer, M.Bielewicz, A.Chłopik, A.Dudziński, M.Grabowski, K.Grodzicki, E.Jaworska, S.Mianowski, M.Pietrzak, J.Rzadkiewicz, P.Sibczyński, Ł.Świderski, A.Syntfeld

University of Warsaw, POLAND

W.Dominik, I.Skwira-Chalot, T.Matulewicz, M.Kuich, K.Piasecki, D.Wójcik

Warsaw University of Technology, Warsaw, POLAND

M.Czarnynoga, D.Dąbrowski, G.Kasprowicz, A.Kisiel, M.Ławryńczk, M.Linczuk, M.Peryt, S.Plamowski, J.Pluta, K.Poźniak, P.Rokita, R.Romaniuk, K.Rosłon, T.Starecki, T.Traczyk, P.Wieczorek, D.Wielanek, W.Zabołotny

University of Wroclaw, POLAND

D.Blashke, N.-U.Bastian, U.Shukla

Belgorod National Research University, RUSSIA

A.Klyuev, A.Kubankin, R.Nazhmudinov, K.Vokhmyanina

Institute for Nuclear Research of the Russian Academy of Sciences, Moscow, RUSSIA

A.Botvina, M.Golubeva, F.Guber, A.Ivashkin, A.Izvestnyy, N.Karpushkin, A.Kurepin, S.Morozov, O.Petukhov, A.Strizhak, V.Volkov

National Research Nuclear University MEPhI, Moscow, RUSSIA

E.Alpatov, E.Atkin, N.Barbashina, A.Demanov, O.Golosov, E.Kashirin, P.Kulyamin, G.Nigmatkulov, V.Nikolaev, P.Parfenov, A.Povarov, V.Samsonov, I.Selyuzhenkov, V.Shumikhin, M.Strikhanov, A.Taranenko

Moscow Institute of Physics and Technology, RUSSIA

T.Aushev

North Ossetian State University, Vladikavkaz, RUSSIA

N.Pukhaeva, Y.Kasumov , A.Eremina, A.Korsunov, D.Kibizov, Z.Persaeva, R.Esenov

National Research Center "Kurchatov Institute" – Institute of Theoretical and Exprimental Physics, Moscow, RUSSIA

V.Kulikov, M.Martemianov, M.Matsyuk, S.Bulychjov

National Research Center "Kurchatov Institute", Moscow, RUSSIA

D.Blau, D.Peresunko

Petersburg Nuclear Physics Institute, Gatchina, RUSSIA

A.Ezhilov, O.Fedin, V.Guzey, D.Ivanishchev, A.Khanzadeev, L.Kochenda, D.Kotov, P.Kravchov, E.Kryshen, A.Kyrianova, M.Malayev, V.Maleev, Y.Naryshkin, D.Pudzha, Y.Riabov, V.Samsonov, V.Solovyev, A.Vasilyev, M.Vznuzdaev, M.Zhalov, V.Riabov

Skobeltsyn Institute of Nuclear Physics, Lomonosov Moscow State University, RUSSIA

N.Baranova, G.Bogdanova, E.Boos, M.Cheremnova, G.Eyyubova, D.Karmanov, P.Kharlamov, O.Kodolova, M.Korolev, V.Korotkikh, A.Kryukov, V.Kukulin, D.Lanskoy, I.Lokhtin, L.Malinina, M.Merkin, M.Platonova, G.Romanenko, A.Solomin, T.Tretyakova, V.Volkov, E.Zabrodin

Saint Petersburg State University, RUSSIA

I.Altsybeev, E.Andronov, S.Belokurova, E.Boykova, V.Chulikov, V.Chulikov, A.Erokhin, G.Feofilov, S.Igolkin, V.Il'in, V.Kakichev, V.Kondratev, V.Kovalenko, T.Lazareva, N.Makarov, N.Maltsev, A.Merzlaya, D.Nauruzbaev, D.Nesterov, D.Prokhorova, N.Prokofiev, A.Puchkov, A.Rakhmatullina, V.Sandul, A.Seryakov, K.Sevastianova, O.Sobol, M.Tkachev, S.Torilov, F.Valiev, V.Vechernin, A.Zarochentsev, V.Zherebchevsky

TABLE OF CONTENTS

1 Introduction

The project "Multipurpose detector MPD for studying the properties of hot and dense baryon matter at the collider complex NICA" is devoted to a detailed exploration of the QCD phase diagram and search for the signals of deconfinement phase transition and the critical endpoint [1]. Comprehensive investigations in the unexplored region of the phase diagram of strongly interacting matter will be performed by a careful energy and system-size scan with ion species ranging from protons to Au^{79+} over the energy range $4 < \sqrt{s_{NN}} < 11$ GeV. The goal of the Project is to design and build a multifunctional detector to measure heavy-ion collisions and investigate the basic Quantum Chromo Dynamics structure of matter. A vast research program in heavy-ion collisions (HIC) has been carried out over last 20 years and a number of new phenomena were discovered. There is a strong evidence for a deconfinement phase transition in central HIC at low SPS energies [2]. Extensive experimental data collected by the RHIC experiments [3] suggest formation of a new state of dense partonic matter - strongly interacting Quark-Gluon Plasma (sQGP). However, it is commonly believed that a next generation of heavy ion experiments is required for much more sensitive and detailed study of the QCD phase diagram in the region of large baryochemical potential μ_B [4]. Several accelerator centers have recently started new programs with heavy ions: SPS at CERN [5], RHIC at BNL[6] and CBM at FAIR [7] may be considered as complementary programs aimed at the study of relevant physics problems of hot and dense baryonic matter.

The main advantages of the NICA/MPD project is that the NICA accelerator facility will provide a vast choice of beams (from protons to gold ions) in the energy range which brackets onset of deconfinement (center-of-mass energy from 4 to 11 GeV). A high luminosity of NICA (L = 10^{27}cm^{-2}s^{-1}) allows small enough energy steps and provide high interaction rate. The key feature of the proposed MPD detector design that allows studying of nuclear collisions with high precision are:

- High event rate (up to 6 KHz) allows very subtle measurements of the energy and centrality dependence of any phenomenon under interest
- MPD has full azimuthal coverage and will measure most of the momentum range in the pseudo-rapidity interval $-2 < \eta < 2$.
- Tracking and particle identification system including TPC for energy loss and TOF for time-of-flight measurements complemented by an electromagnetic calorimeter for photons and electrons with good time and energy resolution.

The first MPD concept was presented in Letter of Intend issued in February 2008, the first version of the Conceptual Design Project was issued in December 2009 [8].

The existing international collaboration aimed in the Project realization consists of about 450 scientists from 16 Institutions from Russia and abroad. This document is organized as follows. The main physics goals of the MPD experiment are summarized in the next Section. In Section 3, a general concept of the MPD detector is presented and the main components of MPD are described in some details. In the following section the first results of detector performance studies are presented. The document concludes with tables for the cost estimate and the construction schedule.

References

[1] A.N. Sissakian and A.S. Sorin, J. Phys. G: Nucl. Part. Phys. 36 (2009) 064069.

[2] C.Alt et al.Phys.Rev.C 77, 2008, 024903.

[3] Nucl.Phys. A757 (2005), 1-283

[4] Searching for a QCD mixed phase at the NICA (NICA White paper). Draft v2.01,

30 September 2009. http://nica.jinr.ru/

[5] NA61 experiment. CPOD07 (2007),023. Eprint=0709.1646.

[6] G.S.F. Stephans, J. Phys., G32 (2006), S447-S454.

[7] P.Senger, J. Phys. G30 (2004), S1087-S1090.

[8] The MultiPurpose Detector (MPD). Conceptual Design Report, v1.0.

http://nica.jinr.ru/

A vast research program in heavy-ion collisions (HIC) has been carried out over recent years and a number of new phenomena were discovered. The diversity of the experimental landscape of HIC data, obtained at the AGS, SPS, RHIC and LHC, is already quite rich and impressive. One may start here with referring to the studies of NA49 collaboration at SPS in investigations of the phase diagram of strongly interacting matter and there is a strong evidence for a deconfinement phase transition in central HIC at low SPS energies [1]. Extensive experimental data collected by the RHIC experiments [2] suggest formation of a new state of dense partonic matter - strongly interacting Quark-Gluon Plasma (sQGP). Recently, the main scientific goals of the Beam Energy Scan (BES) program included the search for the onset of the deconfinement and scan of the phase diagram with variable collision energy from 200 GeV down to a few GeV. The BES program at RHIC produced a wealth of results to describe the bulk properties of the medium created in Au+Au reactions for collision energies of 7.7, 11.5, 19.6, 27, 39, 62.4 and 200 GeV by measuring hadron production at midrapidity. However, it is commonly believed that a next generation of heavy ion experiments is required for much more sensitive and detailed study of the QCD phase diagram in the region of large baryochemical potential μ_B. In Fig. 2.1 (left panel), the dynamical trajectories at two collisions energies are shown for central (b = 2 fm) Au + Au collisions. The highly non-equilibrium part of trajectories are calculated within the kinetic Quark Gluon String Model (shown by open symbols) and the subsequent evolution (filled symbols) is evaluated within the 3D relativistic hydrodynamics [3].

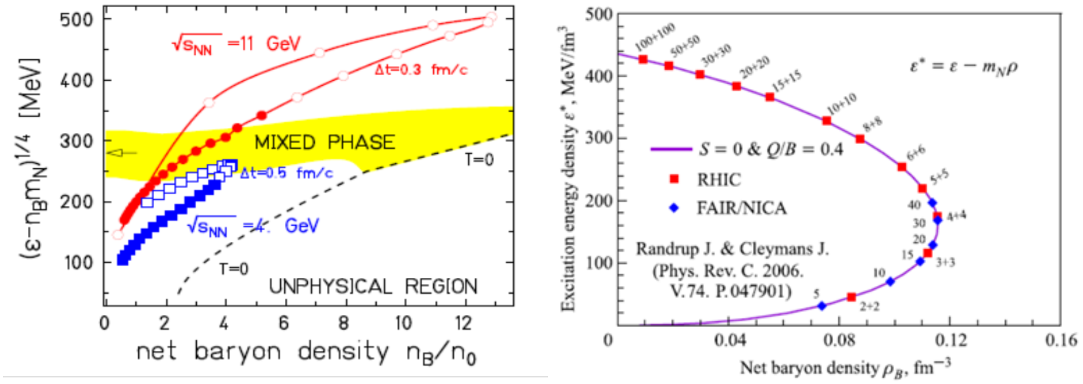

Fig. 2.1: (Left) The phase diagram in terms of the reduced energy density and net baryon density. The highlighted region is a quark-hadron mixed phase estimates according to the phenomenological two-phase equation of state [3]. The dashed curve separates the unphysical region by condition T = 0. (Right) Correlation of the net baryon density and the excitation energy density in central Au+Au collisions [4].

The fascinating particularity of this region is that the nuclear matter at highest net baryon density is achieved (see Fig. 2.1, right panel) [4], as well as new states of matter beyond the deconfinement and chiral transitions.

At present, several complementary experimental programs throughout the world are planned to further study heavy-ion reactions at lower energies. In particular, nucleus-nucleus collisions at the NICA accelerator complex at JINR (Dubna, Russia) permit the exploration of the nuclear matter properties in the region where the baryon density increases substantially. The new experimental program planned at high intensity NICA beams will bring deeper insight into the dynamics of hadronic interactions and multiparticle production mechanisms in the expected high baryonic density regime [5]. Furthermore, the investigation of the properties of nuclear matter inside neutron stars is the key goal of modern astrophysics. The recent observation of the neutron star merger both via gravitational waves [6] began the new era of mutli-messenger astronomy. Recent model calculations reveal that in the neutron star merger process nuclear matter reaches densities and temperatures expected in the heavy-ion collision in the NICA energy range. Therefore, the MPD experimental NICA offers unique opportunity to study such processes in the laboratory.

The global scientific goal of the NICA/MPD project is to explore the QCD phase diagram in the region of highly compressed and hot baryonic matter. In particular, the fundamental QCD phenomena, such as confinement, properties of the QCD vacuum and QCD Lagrangian symmetries, quantitative understanding of which is still lacking, will be addressed. In particular, the NICA/MPD project will be focused on the study of the in-medium properties of hadrons and the nuclear matter Equation Of State (EOS), including a search for possible signals of decofinement and/or chiral symmetry restoration phase transitions, as well as the QCD critical endpoint (CEP) in the region of the collider energies $\sqrt{s_{NN}} = 4 - 11$ GeV. The basic experimental strategy will to measure a large variety of signals systematically changing collision parameters (energy, centrality and system size). Reference data (i.e. pp and pA collisions) will be taken in the same experimental conditions. A tentative list of experimental observables includes:

a) the yields, spectra, and ratios for multiple probes from gammas to light nuclei;

b) event-by-event fluctuations and correlations;

c) collective flow of identified hadron species;

d) strangeness production in dense baryon matter, including multistrange hyperons and hypernuclei;

e) femtoscopy; d) electromagnetic probes (electrons and gammas). The hadrons containing heavy strange quarks and anti-baryons are of particular interest.

According to lattice QCD calculations a phase transition from the hadronic phase to the phase composed of deconfined quarks and gluons is suggested at energy density exceeding a value of about 0.5~GeV/fm^3. Microscopic model calculations indicate such a density can be achieved in the center of the fireball created in head-on collisions of gold ions at center-of-mass energies above 4-5 GeV. The deconfinement transition is found to be a crossover at zero net-baryon density [7], while arguments based on effective models predict that it becomes a first-order transition at some finite chemical potential [8]. It implies the existence of a critical end point (CEP) in the phase diagram of the QCD matter separating both phase transition types [9]. The potentially rich structure of the QCD phase diagram at high net-baryon densities requires experimental verification. The QCD phase diagram structure might be tested by measuring abundances of different hadron species, while different regions of the diagram are accessible by varying the collision energy. Existing experimental results on hadron abundances in the range from AGS to LHC energies indicate that the final state of HIC is close to chemical equilibrium, thus the yields are fitted by the statistical thermal model with two free parameters: temperature T and baryochemical potential μ_B. Assuming that the measured multiplicities are preserved throughout final hadron-resonance cascade expansion, their analysis reveals the hadronization point along the QCD parton-hadron boundary line. Moreover, the analysis of hadron abundances might (potentially) allow to address the much debated onset of deconfinement problem. If HIC dynamics within the NICA energy range crosses the phase transformation line starting from a particular (threshold) energy, then, below this value, the actual hadronic multiplicity would not stem from the QCD hadronization phase transition (responsible for chemical equilibration among the species) and we would expect a sizeable change in the observed hadronic freeze-out pattern, such as a sequential chemical freeze-out in inverse order of inelastic cross-section.

Study of (anti)hyperon production is of particular interest because of several reasons. First of all, the strangeness enhancement in heavy-ion collisions relative to proton induced reactions has been proposed as a signature for the deconfinement. The expected increase of the strange particle production in a QGP phase is due to both the lower threshold of the s-sbar pair production and the addition of gluon fragmentation channels [10]. It was also established experimentally that this strangeness enhancement is stronger for particles with higher strangeness content [11,12]. Secondly, since the hadronic cross-sections of multi-strange hyperons are small, additional re-scattering effects in the dense hadronic matter for strange hadrons are not as important as for other hadrons. Thus, measured phase-space distributions of strange hyperons reveal important characteristics of the fireball at the early stages of the system evolution. Moreover, it has recently been observed by the STAR experiment that the characteristic azimuthal anisotropy pattern (e.g. the elliptic flow coefficient v_2 as a function of transverse momentum p_t) for anti-baryons (including those with strangeness) is different from the one for baryons in mid-central Au+Au collisions at center of mass energies < 11GeV [13]. Antibaryons are strongly affected by the commoving baryon density in the course of the reaction: there is interplay between particle production and subsequent absorption in the medium. Therefore, new experimental data on (anti)hyperon production, to be taken at NICA as a function of the collision energy and beam atomic mass number, will provide a valuable insight into the reaction dynamics.

Collective flow phenomena in heavy ion collisions are important signatures of the physics dynamics at the reaction early stage. The anisotropic collective flow, as manifested by the anisotropic emission of particles in the plane transverse to the beam direction, is one of the important observable sensitive to the transport properties of the strongly interacting matter: the EOS, the speed of sound, as well as the specific shear and bulk viscosities [14]. Anisotropic flow measurements at the RHIC and the LHC have provided strong evidence for the formation of a strongly coupled Quark-Gluon Plasma (sQGP), a new state of matter with partonic degrees of freedom and low specific shear viscosity [15]. The azimuthal anisotropy of produced particles can be quantified by the Fourier coefficients v_n in the expansion of the particles azimuthal distribution, where *n* is the order of the harmonic. Relativistic viscous hydrodynamics has been successful in describing the observed anisotropy of the flow coefficients for the produced particles in the collisions of heavy-ions at RHIC and LHC [16]. Moreover, the predicted first-order phase transition between hadronic and sQGP phases can be characterized by a dramatic drop in the pressure, or a softening of the EOS [17]. In particular, the rapidity-odd component of directed flow (v1) can probe the very early stages of the collision as it is generated during the passage time of the two colliding nuclei. Both hydrodynamic and transport model calculations indicate that the directed flow of charged particles, especially baryons at midrapidity, is very sensitive to the EOS [17,18]. The slope of the rapidity dependence dv_1/dy near midrapidity is a convenient way to characterize the overall magnitude of the rapidity-odd component of directed flow signal [19]. A minimum in dv_1/dy at y=0 could be related to the softening of equation-of-state due to the first order phase transition between hadronic matter and sQGP [17,19]. In addition, according to the typical ideal hydrodynamic scenario, a non-monotonic energy dependence of the elliptic of parameter v_2 is predicted because of softening of the EOS near the critical temperature of quark-hadron phase transition [20]. Besides the integral elliptic flow measurements, study of v_2 as a function of transverse momentum for various hadron species are of a great interest. In particular, observed at RHIC energies an approximate independence of v_2/nq as a function of p_t/n_q for many hadron species (n_q is the number of constituent quarks for the given hadron type) can be explained in terms of the elliptic flow formation on a partonic level [21]. The breaking of such constituent quark scaling at lower energies may carry information on the changes in the properties of created dense matter. Since at NICA energies the energy dependence of flow coefficients for hadrons is not established, more detailed measurements are required. It is expected that the high-accuracy and high-luminosity measurements of differential anisotropic flow for various hadron types over the full MPD/NICA energy range will provide important constraints on the early dynamics of heavy ion reactions under conditions where a first order quark-hadron phase transition may occur.

The study of hyperon flow is of particular interest due to the small hadronic cross-sections of strange and multi-strange hyperons, additional re-scattering effects in the dense hadronic matter for strange hadrons are not as significant as compared to other hadrons. Hyperon measurements may reveal key characteristics of the fireball at the early stages of the system evolution. Moreover, as observed by the STAR experiment, the elliptic flow as a function of transverse momentum for anti-baryons is different from the one for baryons in mid-central gold-gold collisions at CM energies < 11A GeV, the wide range of collision systems at NICA will provide a valuable insight into the reaction dynamics on hyperon production and flow.

Intensity interferometry, usually referred to as "femtoscopy" is used extensively in heavy-ion collision studies to determine the size of the particle-emitting region as well as the details of the spatio-temporal dynamics of the system evolution [22-24]. The technique of the correlation function used in the measurements is, to the first order, insensitive to single particle acceptance effects, so it does not have strict requirements on the precision of the calibration process. At the same time, it provides critical and sensitive probe of the two-particle tracking and PID efficiency. As a result, measurement of the two-pion femtoscopic correlation functions is usually among the first performed at accelerator complexes immediately after their turn-on and as such, are excellent candidates for "First Physics" measurements. Femtoscopy measurements have been performed for several decades, as a function of collision energy, colliding system, collision centrality, pair transverse momentum, reaction plane orientation and more [25,26]. A dependence of pion interferometry sizes on collision energy is of particular interest here. It has been argued [27] that a first-order phase transition will extend the lifetime of the system created in a heavy-ion collision. An expanding system living longer, will naturally reach larger size at freeze-out. This size is measured by pion femtoscopy. Therefore, measuring the size of the colliding system, in the NICA collision energy range is a crucial ingredient of the search for the existence and nature of the phase transition deconfined and hadronic matter.

If the system during its evolution passes the vicinity of the critical region and remains there for long enough time, one expects an increase in fluctuation pattern for several observables, i.e. event-by-event multiplicity, transverse momentum, particle ratio, and baryon number fluctuations are expected to grow [28]. The MPD detector has a big advantage in these measurements over any fixed target configuration experiment because of uniform high acceptance, high event rate, and powerful particle identification system.

At sufficiently high temperature and/or baryon density, which could be realized in heavy ion collisions at NICA the deconfinement phase transition might be accompanied by restoration of chiral symmetry due to melting of the quark condensate at the transition temperature [29,30]. The correlated e+e- or μ+ μ pairs (dileptons), especially those from decays of vector mesons (ρ,ϕ,ω) are the best candidates to relate medium modifications of hadronic spectral function to the restoration of the chiral symmetry in A+A collisions [31,32] since their decay products (i.e. electrons and positrons) interact only electromagnetically, thus escaping the interaction region unaffected by subsequent strong interactions in dense hadronic matter and carrying to the detectors information about the conditions and properties of the medium at the time of their creation. Leptons and photons produced during the whole evolution of the created matter, such that higher e+e- pair invariant mass stands for earlier generating time while higher direct photon transverse momentum stands for earlier production time. By choosing different kinematics of these EM probes, the properties of the formed matter throughout its entire evolution can be studied. Production of low-mass dileptons (M_{e+e-}<1.2 GeVc^2) in heavy-ion collisions have been studied at the CERN-SPS at center-of-mass energy of 8.8A, 17A and 19A GeV [33-36]. The CERES Collaboration has observed a strong excess in the invariant-mass spectrum of electron-positron pairs in the region 0.2<M_{e+e-}<0.7 GeV/c^2 above the expectations from the superposition of known hadron decay channels based on their vacuum properties [33,34]. Moreover, a stronger enhancement observed at 8.8A GeV indicates sensitivity of the physics signal to the baryon density attained in the reaction. Until now, no dilepton measurements have been performed at AGS and low SPS energies (results on dileptons from the RHIC BES program at energies below 20 GeV have not yet been published) and the NICA-MPD dilepton program is aimed to close this gap. The chosen range of collision energies (4-11A GeV) is very promising for such a measurement since the effect is expected to be sensitive to the baryon density, while the latter happens to reach the maximum in central Au+Au collisions at NICA [4].

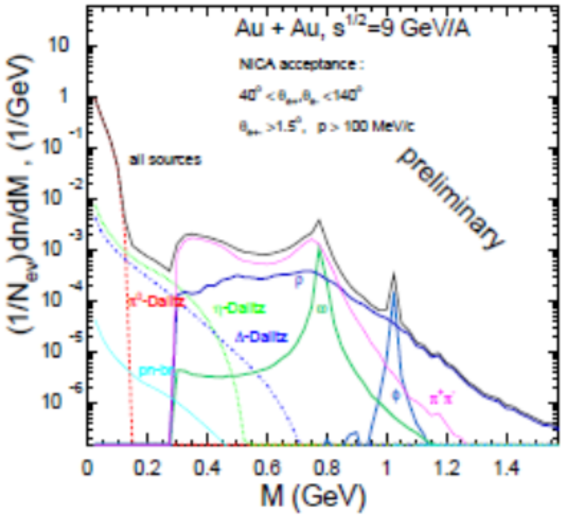

Fig. 2.2: Dielectron spectrum in central Au + Au collisions at √SNN = 9 GeV. Calculations are made by the QGSM code.

Spectra of dielectrons from decays of pseudoscalar and vector mesons in central Au+Au collisions generated by the QGSM event generator for the MPD acceptance are shown in Fig. 2.2.

Relativistic HIC where many strange particles (kaons and hyperons) are produced, offer a unique possibility to create exotic nuclear objects with strangeness – hypernuclear [37]. Hypernuclei offer the opportunity to study the properties of hyperon interactions in dense medium, thus allow unveiling the structure and evolution of stellar objects - neutron stars [38]. For example, the presence of hyperons in the collapsed stellar core, appearing in degenerated neutron matter due to the strangeness-changing reactions, produces a softening of the corresponding EoS, consequently, violates the mass-radius relationship for neutron stars resulting in the stellar maximum mass not compatible with measured neutron star masses (“hyperon puzzle”). The problem lies, however, in proper description of the underlying hyperon-nucleon (YN) and hyperon-hyperon (YY) interactions in dense medium, which are rather uncertain and poorly known because YN and YY scattering experiments are difficult to perform. In this respect, a systematic and detailed study of hypernuclei at NICA would offer the possibility of increasing the experimental information on YN and YY interactions. The energy range of the NICA research program covers the region of the maximal baryon density where the production rates of nuclear clusters with strangeness (see Fig.2.3) are predicted to be enhanced considerably [39]. With a typical event rate of 6 kHz for the design NICA luminosity of 10^{27} cm^{-2} c^{-1} a detailed study of the production mechanism of single hypernuclei as well an observation of double hypernuclei at NICA looks feasible.

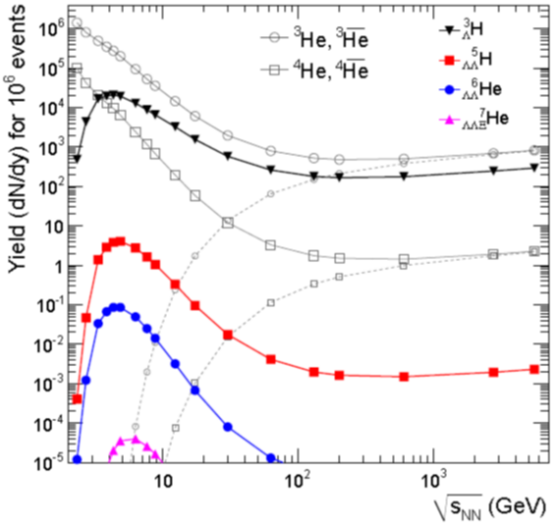

Fig. 2.3. The yields of nuclei and hypernuclei from central Au+Au collisions. The numbers are obtained from thermal model calculations [39].

REFERENCES

[1] C.Alt et al. (NA49 Collab.), Phys. Rev. C 77, 024903 (2008).

[2] RHIC Experiment White Papers, Nucl. Phys. A757, 1-283 (2005).

[3] A.S.Khvorostukin et al., Eur. Phys. J. C48 (2006), 531-543.

[4] J. Randrup and J. Cleymans Phys. Rev. C 74 (2006) 047901.

[5] V. D. Kekelidze, R. Lednicky, V. A. Matveev, I. N. Meshkov, A. S. Sorin and G. V. Trubnikov, Eur. Phys. J. A52, 211 (2016).

[6] Abbott, B. P. et al. (LIGO Collab.), Phys. Rev. Lett. 119, (2017), 161101.

[7] Aoki Y., Endrodi G., Fodor Z., Katz, S. D., SzaboK. K., Nature 443 (2006) 675-678.

[8] Asakawa M., Yazaki K., Nucl. Phys. A504 (1989), 668-684.

[9] Berges J. and Rajagopal K., Nucl. Phys. B538 (1999), 215-232.

[10] J. Rafelski and B. Muller, Phys. Rev. Lett. 48, 1066 (1982)

[11] F. Antinori et al. (WA97 Collaboration), Eur. Phys. J. C 11, 79 (1999)

[12] F. Antinori et al. (NA57 Collaboration), J. Phys. G 32, 427 (2006)

[13] L. Adamczyk et al. (STAR Collaboration) Phys. Rev. C88, 014902 (2013)

[14] Snellings R., J. Phys. G41 (2014) 124007.

[15] Busza W., Rajagopal K., W. van der Schee, Ann. Rev. Nucl. Part. Sci. 68 (2018) 339.

[16] Gale Ch., Jeon S., Schenke B., Tribedy P., Venugopalan R., Phys. Rev. Lett. 110 (2013) 012302.

[17] Stoecker H., Nucl. Phys. A750 (2005) 121-147.

[18] Rischke D. H., Nucl. Phys. A610 (1996) 88C-101C.

[19] Singha S., Shanmuganathan P., Keane D., Adv. High Energy Phys. 2016 (2016), 2836989.

[20] P. Kolb, J. Solfrank and U. Heinz, Phys.Rev.C 62 (2000), 054909.

[21] S.A. Voloshin, J.Phys.Conf.Ser. 9 (2005), 276.

[22] Kopylov G. I. and Podgoretsky M. I., Sov. J. Nucl. Phys. 15 (1972) 219.

[23] Lednicky R., Phys. Atom. Nucl. 67 (2004) 72-82.

[24] Lisa M. A., Pratt S., Soltz R., Wiedemann U., Ann. Rev. Nucl. Part. Sci. 55 (2005) 357.

[25] Aamodt K. et al. (ALICE Collab.), Phys. Lett. B696 (2011) 328.

[26] Adler C. et al. and others (STAR Collab.), Phys. Rev. Lett. 87 (2001) 082301.

[27] Wielanek D. et al. Acta Phys. Polon. Supp. 9 (2016) 341.

[28] M. Stephanov, K. Rajagopal, and E. Shuryak, Phys. Rev. Let. 81, 1998, 4816.

[29] R. Rapp and J. Wambach, Adv. Nucl. Phys. (2000) 25, 1.

[30] T. Hatsuda and S.H. Lee, Phys. Rev. C 46 1992, R34.

[31] R. Rapp, G. Chanfray and J. Wambach, Phys. Rev. Let. 76 (1996) 368.

[32] G.E. Brown and M. Rho, Phys. Rev. Let. 66 (1991) 2720.

[33] D. Adamova et al. (CERES Collaboration) Phys. Rev. Let. 91 (2003) 042301.

[34] D. Adamova et al. (CERES Collaboration) Phys. Let. 666 (2008) 425.

[35] R. Arnaldi et al. (NA60 Collaboration), Phys. Rev. Let. 96 (2006) 162302.

[36] A. Adare et al. (PHENIX Collaboration) Phys. Rev. C81 (2010) 034911.

[37] A. K. Kermann and M. S. Weiss, Phys. Rev. C 8 (1973) 408.

[38] Lattimer J. M., Prakash M., Science 304 (2004) 536.

[39] A. Andronic et al., Phys. Lett. B 697 (2011) 203.

3. MPD detector

3.1 Introduction

The MPD apparatus has been designed as a 4π spectrometer capable of identifying charged hadrons, electrons and photons in heavy-ion collisions in the energy range of the NICA collider and measuring their momenta. To reach this goal, the detector will comprise a precise 3-D tracking system and a high-performance particle identification (PID) system based on the time-of-flight measurements and calorimetry. The basic design parameters has been determined by physics processes in nuclear collisions at NICA and by several technical constrains guided by a trade-of of efficient tracking and PID against a reasonable material budget. At the design luminosity, the event rate in the MPD interaction region is about 6 kHz; the total charged particle multiplicity exceeds 1000 in the most central Au+Au collisions at $\sqrt{s_{NN}}$ = 11 GeV. As the average transverse momentum of the particles produced in a collision at NICA energies is below 500 MeV/c, the detector design requires a very low material budget. The general layout of the MPD apparatus is shown in Fig.3.1.1. The whole detector setup covering ±2 units in pseudorapidity (η).

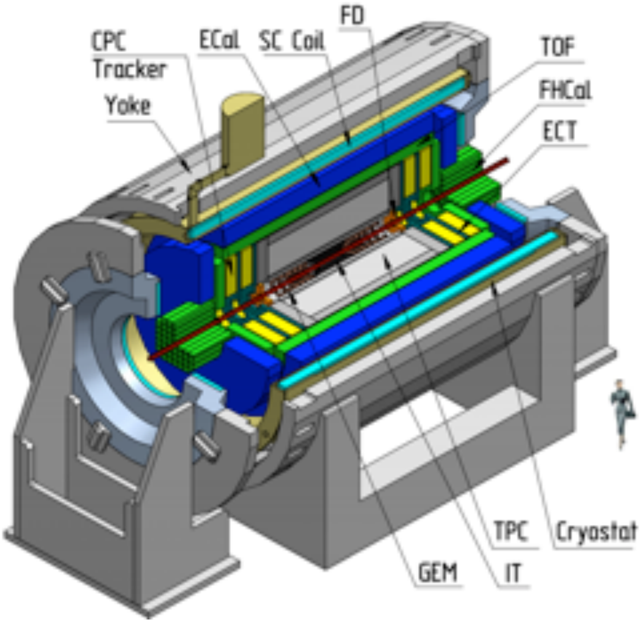

Fig. 3.1.1: Full Configuration of the MPD consists of Magnet Yoke (Yoke) and Solenoid (SC Coil), Time Projection Chamber (TPC), Time of Flight System (TOF), Fast Forward Detector (FFD), Forward hadron Calorimeter (FHCal), Forward Tracker (CPC and ECT) and Inner tracker System (IT)

As soon as construction of such detector requires long period of time, large group of physicists, engineers and technicians and large funds there was decision to build it in two stages.

The aim of this Project is to build the first stage of the MPD setup (Fig.3.1.2), which consists of the Magnet based on superconducting solenoid, Time-Projection Chamber (TPC), barrel Time-Of-Flight, Forward Calorimeter (FHCal) and Fast Forward Detector (FD).

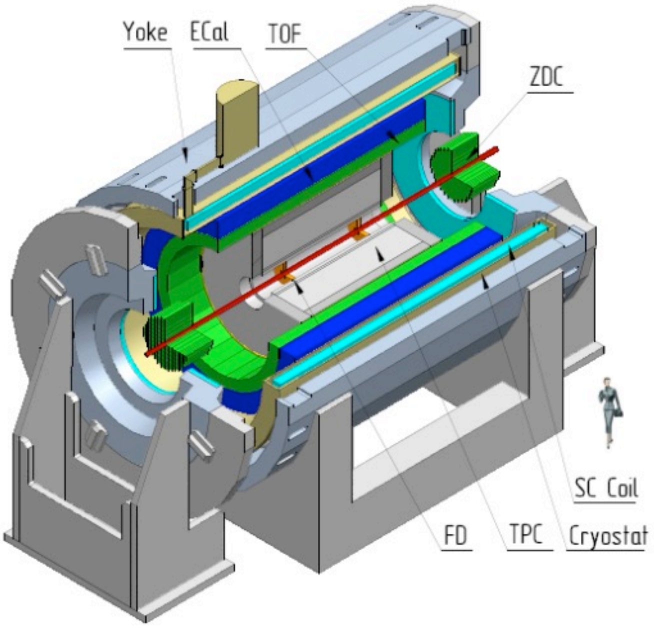

Fig. 3.1.2: The MPD setup in the first Stage. It consists of Magnet Yoke, Solenoid, Time Projection Chamber (TPC), Time of Flight detector (TOF), Electromagnetic Calorimeter (ECal), Fast Forward Detector (FFD) and Forward Hadron Calorimeter (FHCal)

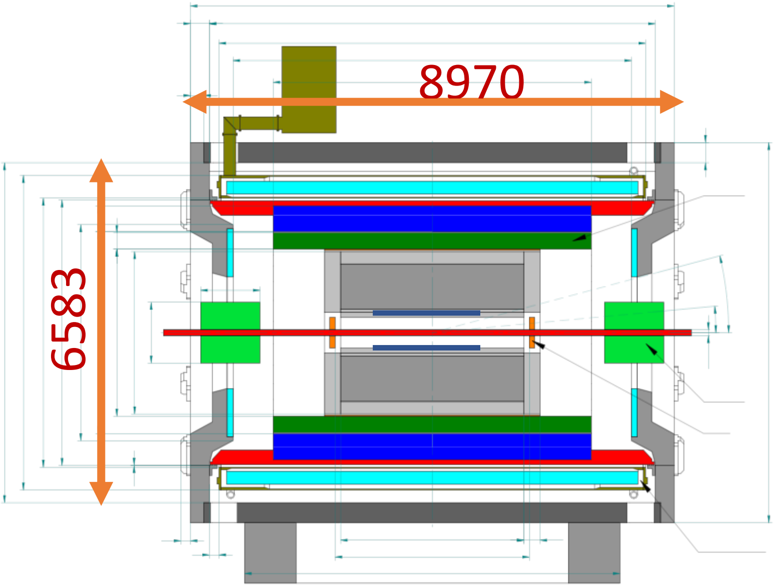

Fig. 3.1.3: Cutaway side view of the MPD in a basic Configuration with main dimensions.

The MPD is a 9 m long cylinder of about 6,6 m in diameter. The cross-sectional view of the MPD Detector in base configuration is shown in Fig. 3.1.3.

3.2 Superconducting magnet

The magnet of the MPD detector is intended to provide a homogeneous magnetic field with a rated value of magnetic field of 0.5 T inside its aperture. The required volume average inhomogeneity in the drift volume of TPC (of about 2.4 m in diameter and 3,4 m long) - Integral(Br/Bz)*dz$\leq 1,5mm$. The superconducting magnet of MPD is intended for providing a highly homogeneous magnetic field of 0.57 T ensure the transverse momentum resolution within the range of 0.1–3 GeV/c at NICA. A constituent part of the MPD is a solenoid with a superconducting NbTi coil and a steel flux return yoke.

The MPD magnet consists of (Fig. 3.2.1):

- a cryostat with a superconducting coil and a control Dewar;
- a flux return yoke with two support rings, 28 bars, and two poles with trim coils;
- magnet support cradles;
- auxiliary platforms for moving the poles;
- roller skates for movement of the magnet and its poles.

In addition, there are power supplies for the superconducting solenoid and for the trim coils in the poles, a SC coil quenching protection system, a cryogenic system with the cryogenic pipeline, a vacuum system, helium refrigerator and a magnet control system.

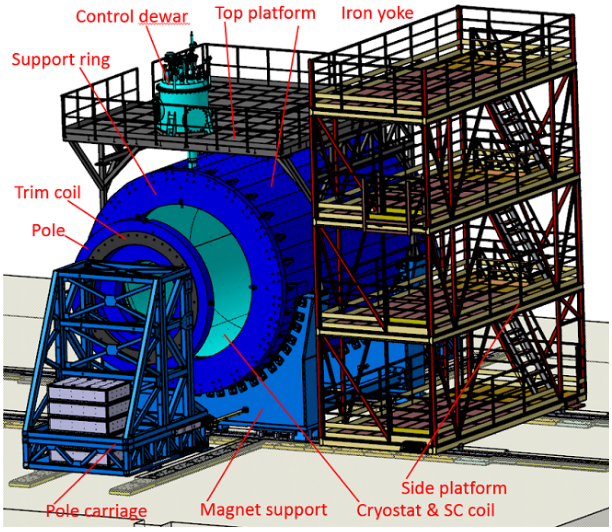

Fig. 3.2.1. Overall view of the magnet.

3.2.1 Solenoid

Rated current of the magnet is 1790 A (it corresponds to a field in the aperture of 0.5 T). The maximum magnet field at which the specified value of the integral of the radial component of the induction in the area of TPC Int $\leq$ 1.5 mm is maintained, and which can be achieved with a maximum level of technological deviations from the optimized geometry of the magnetic system, is 0.57 T.

In 2015 the manufacturer company has been defined for production of the Solenoid and its auxiliary equipment such as power supplies, control and protection system, vacuum system etc. Then, in the end of 2015 related contract has been signed with ASG Superconductors s.p.a (Italy).

The complete assembly of the solenoid has been finished by September 2019 (Fig. 3.2.2). Since that moment the solenoid is ready for transportation to JINR's premises.

Fig.3.2.2 . Completely built solenoid.

3.2.2. Magnet Yoke

In 2012, the geometry of the MPD detector was adopted in the final version (Fig. 3.2.3). The length of the magnetic circuit was 8970 mm, the outer diameter - 6.63 m. The total weight of the magnetic circuit, consisting of 2 support rings, 2 poles and 28 beams, is 630 tons. The weight of the MPD detector in the design configuration is 980 tons.

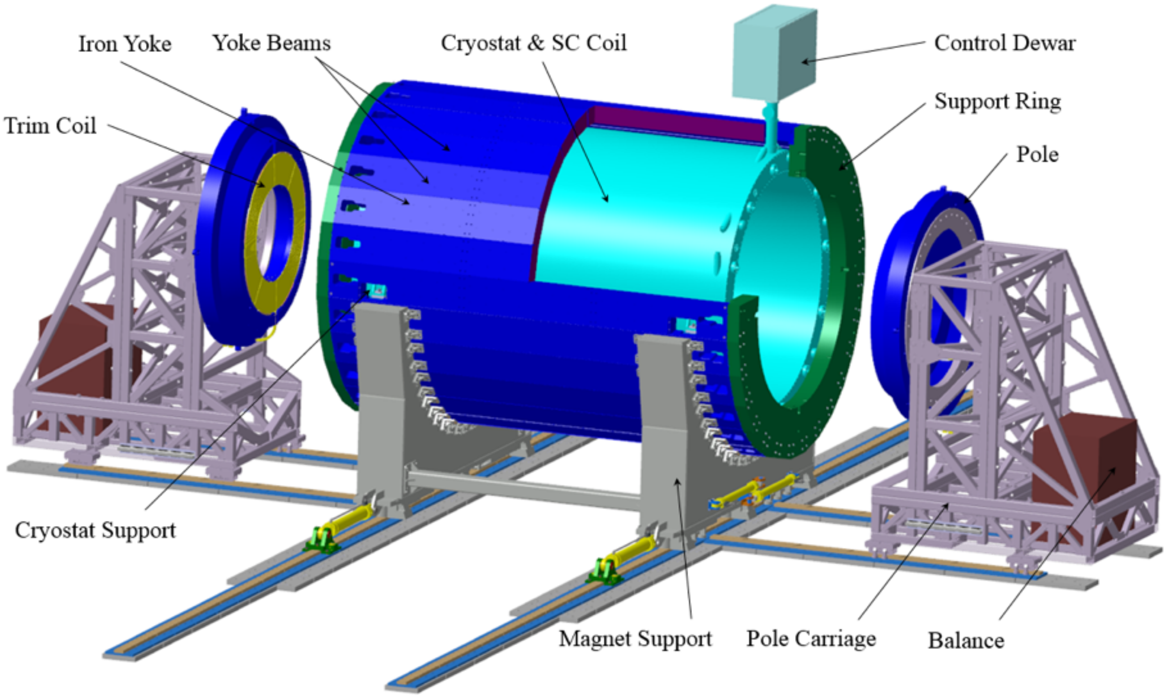

Fig. 3.2.3. MPD magnetic circuit with poles on transport supports.

3.3 Time Projection Chamber - TPC

The Time-Projection Chamber (TPC) is the main tracking detector of the MPD central barrel. It is a well-known detector for 3-dimensional tracking and particle identification for high multiplicity events. The TPC/MPD will provide:

- the overall acceptance of $\eta < 1.2$;
- the momentum resolution for charge particles under 3% in the transverse momentum range $0.1 < p_t < 1$ GeV/c;
- resolution of two tracks of about 1 cm;
- hadron and lepton identification by *dE/dx* measurements with a resolution better than 8%.

These requirements must be satisfied at the NICA design luminosity with event rate about 6 kHz. Max charged particle multiplicity - up to 1000 tracks in central Au-Au collisions.

3.3.1. TPC design

TPC consists of four cylinders (C1-C4) manufactured by the Russian industry from composite materials. This approach provides sufficient cylinders strength along (in the worst case, the deformation at load of F = 80 kG in the middle is less than 100 µm) and a small radiation thickness (0.4 g/cm^2). All four cylinders are interconnected by two aluminum flanges. The gap between C1–C2 and C3–C4 is blow through by nitrogen N_2 for protection against a high-voltage discharges and prevention of H_2O and O_2 diffusion into the drift volume of the TPC.

The central high-voltage electrode-membrane divides the drift volume into two parts and creates the electric field strength which is necessary for the drift of the generated electron-ion clusters to the TPC end-caps (see Fig. 3.3.1, pos. 2). The membrane is produced with the 110 µm Mylar film. The non-uniformity of magnetic field have to be not worse than Br/Bz~10^{-4}. The Field cage (see Fig. 3.3.1, pos. 3) has a symmetrical design, each part of which is located on both sides of the high-voltage electrode and consists from 112 pairs (outer and inner structures) of 13 mm wide mylar strips stretched on special rods with the same pitch and accuracy of 50 µm. The high-voltage electrode is connected to the nearest mylar strip by a resistor and each subsequent strip is connected by a resistor to the next one. This chain forms a HV divider from -24 kV (high voltage electrode) to zero (TPC end-caps).

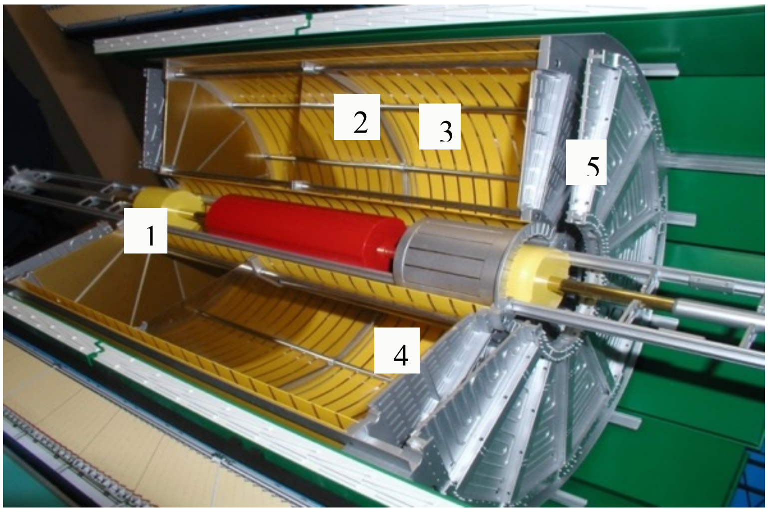

Fig. 3.3.1. Central part of the MPD (mock up). 1- MWPC; 2 - HV electrode; 3 - field cage; 4 – flange with MWPCs and FEE electronics; 5 - end cap thermal screen.

The main subsystems of TPC include:

- Readout Chambers (ROC)
- Gas System
- Laser Calibration System
- Cooling System
- FEE, Readout and DAQ
- DCS
- HV and LV systems

The basic design parameters of the TPC are summarized in Table 3.3.1.

Table 3.3.1

The basic parameters of the TPC

Item	Dimension
Length of the TPC	340 cm
Outer radius of vessel	140 cm
Inner radius of vessel	27 cm

Outer radius of the drift volume	133 cm
Inner radius of the drift volume	34 cm
Length of the drift volume	163 cm (of each half)
HV electrode	Membrane at the center of the TPC
Electric field strength	140 V/cm
Magnetic field strength	0.5 Tesla
Drift gas	90% Ar+10% Methane
Gas amplification factor	10^4
Drift velocity	5.45 cm/μs
Drift time	< 30 μs
Temperature stability	< 0.5°C
Number of readout chambers	24 (12 per each end-plate)
Segmentation in φ	30°
Pad size	5x12 mm^2 and 5x18 mm^2
Number of pads	95232
Pad raw numbers	53
Zero suppression	up to 90%
Maximal event rate	< 7 kHz (Lum. 10^{27})
Electronics shaping time	180-190 ns
Signal-to-noise ratio	30:1
Signal dynamical range	10 bit
Sampling rate	10 MHz
Sampling depth	310 time buckets
Resolution of two tracks	1 cm

3.3.2 Readout Chamber (ROC)

For the startup period of operation a ROC based on Multi-Wire Proportional Chambers (MWPC) with cathode pad readout and gate grid was chosen (see Fig. 3.3.1, pos.1). The gap between the anode wire plane and the cathode pad plane is the same as the gap between the anode wire and the cathode wire planes and is 3.0 mm. The anode wire pitch is set equal to S=3 mm and it is multiple to the pad length. Cathode wire pitch is 1.5 mm. The gate grid is placed 3 mm above the cathode wires and it wire pitch is 1.25 mm. Gate grid is used to stop the flow of ions from MWPC to TPC drift volume. To ensure the gas gain at the level of $G = 10^4$ with moderate anode wire potential, the 20-μm diameter gold-plated tungsten−rhenium anode wire with tension 50 gram is used. The

75-μm diameter copper−beryllium wire wound under an 80-g force is used for the cathode plane. The pad geometry is selected based on the pad response function calculation and measurements to provide the required spatial resolution, and the number of pad rows is determined by the momentum resolution requirement. There are 27 rows of 5×12 mm pads in the inner area of the pad plane and 26 rows of pads with dimensions 5×18 mm in the outer area. The total number of registration channels of the TPC is 95232. Pad plane is produced by multilayer printed circuit board technology. It has 4 layers: a layer with pads, a layer with a ground plane, a layer with signal routing and a layer with connectors that are 1 mm apart from each other for a parasitic capacity minimization, which together give a total board thickness of 3 mm.

3.3.3 Gas system

The design of TPC gas system is based on the experience of the gas systems construction for STAR and PHENIX experiments at Brookhaven National Laboratory, USA. The system consists of two recirculation loops: inner and outer. It operates nominally as a closed circuit with the majority of mixture recirculation through the TPC in the inner loop. During normal operation a small amount of fresh mixture is added and an equivalent quantity (including TPC leakage) of the existing mixture is vented with the outer recirculation loop. The gas system can operate in an open configuration for purging the detector.

Gas mixture for the TPC at the correct pressure, temperature and composition are (10 ± 0.1%) CH_4 in Ar at internal TPC pressure 2±0.01 mbar with fresh gas flow 200 – 3 000 l/h.

Structurally, the gas system can operate as in the closed version for a long term experiment as in the opened one for purging of the TPC. Since the distance between the TPC and the gas system location is about 70 meters, the gas scheme contains two circulating loops: outer - with the compressors and inner - with the blowers. These loops are assembled into two racks as shown in Fig. 3.3.2.

Fig. 3.3.2. Assembled rack 1 and rack 2 for gas system

3.3.4 TPC laser calibration system

Laser calibration system needed to minimize the error in the absolute measurement by the TPC. It takes into account both static and time-depend distortions in the electron drift path and determines drift velocity. The system is based on the two UV 266 nm wavelength lasers with short pulse (5 ns) and pulse power up to 130 mJ. Laser beam splitter provides 224 straight rays to simulate 1 mm diameter tracks – enough to have information about whole TPC volume.

Schematic view of laser beam and technical drawing of 28 "tracks" of 1 mm in diameter calibration system which is under realization presented in Fig. 3.3.3 and Fig. 3.3.4.

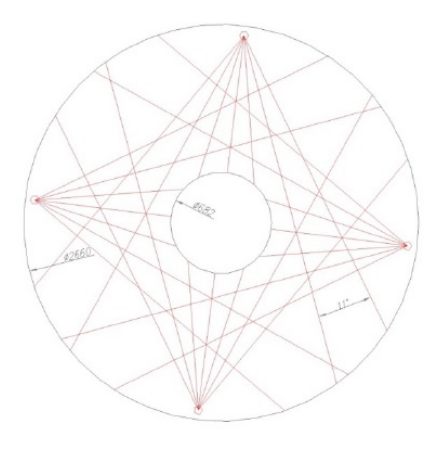

Fig. 3.3.3. Schematic view of 28 "tracks" of 1 mm in diameter

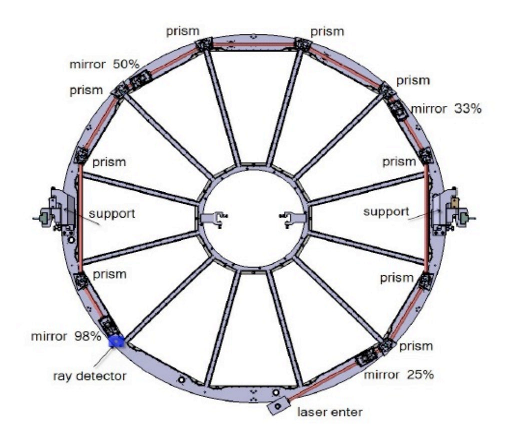

Fig. 3.3.4. Technical drawing of laser beams inside of TPC support ring

3.3.5. Cooling system

Temperature stabilization will include a thermometric system using 180 Pt100 sensors placed on the detector body providing temperature measurements with an accuracy of 0.1°C and a thermal stabilization system (see Fig. 7, pos. 5) using distilled water as a thermal agent. The goal of design is a stability of the gas temperature inside the TPC volume within 0.5°C. TPC barrel thermal screen and the samples of cooling panels are shown in Fig. 11.

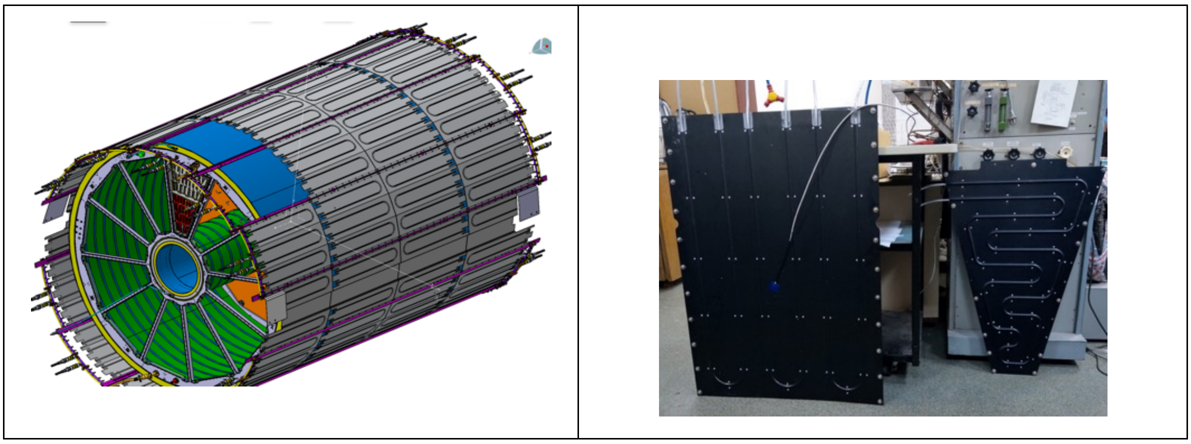

Fig. 3.*3.5 TPC barrel thermal screen and cooling panels samples*

3.3.6 Front-End Electronics (FEE) and data readout system

The TPC FEE is based on ASIC[3], FPGAs and high-speed serial links (see Fig. 3.3.6). To protect the FPGA firmware from SEU, standard proprietary methods are suggested.

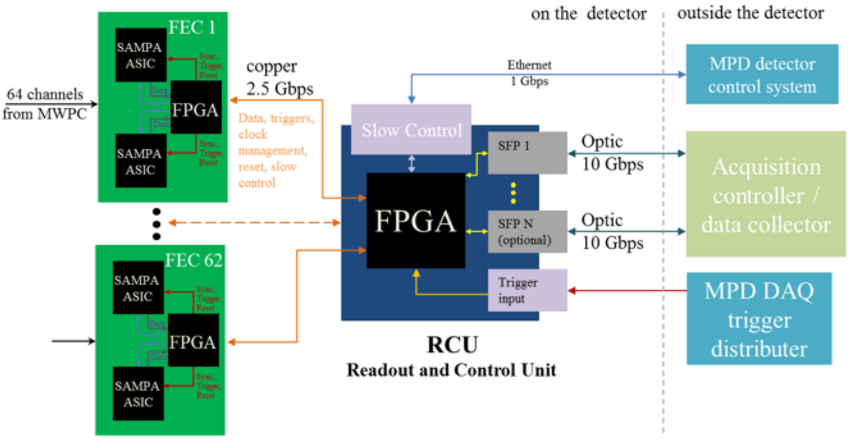

Fig. 3.3.6. Block diagram of data readout for one from 24 ROC chamber.

Each of 62 Front-End Cards (FECs), which are the basic elements of the data acquisition system from each ROC are controlled by common Readout and Control Unit (RCU). Each FEC has a separate bidirectional communication interface with the controller (cooper link, up to 2.5 Gbps), which is used for card management, data receiving, FEC condition monitoring and providing of synchronization, triggering and reset signals (Fig. 3.3.6). Each of the 62 FECs operate in parallel and independently of each other, which provide overall system throughput at this level. The base functions of the RCU are the following: FECs management, data receiving from FECs, FECs synchronization, slow control, transfer of data to data collector via the optical interface, communication with the general MPD detector control system via an Ethernet port.

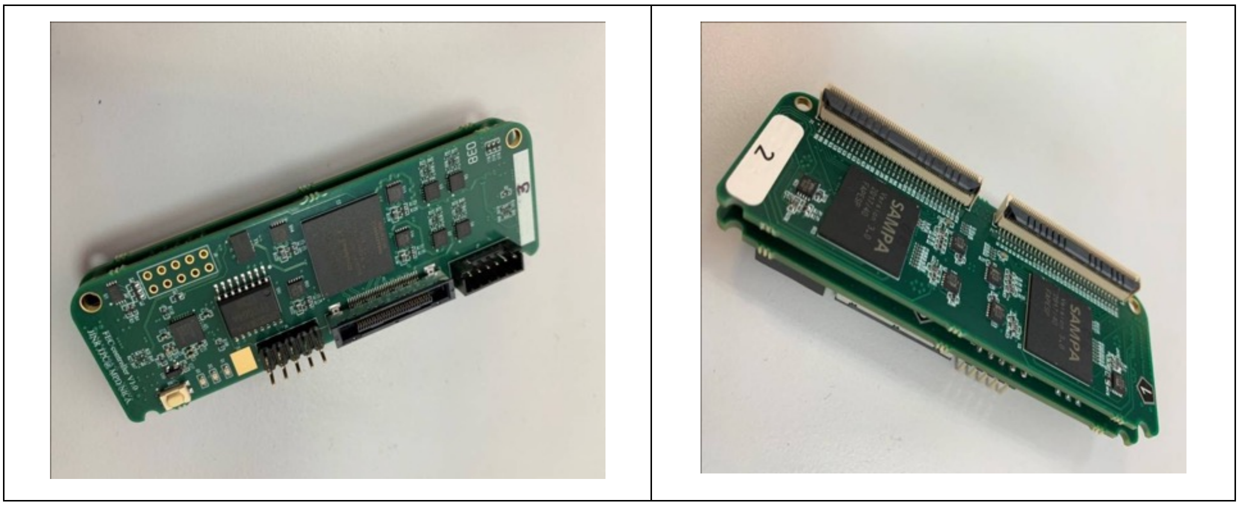

Fig. 3.3.7. FEC for TPC: top view (service side), left and bottom view (to padplane connected side), right.

Each of the 1488 FECs includes two ASICs called SAMPA which was developed by USP Brazil electronics group mainly for upgrade ALICE experiment at CERN. The SAMPA usage on cards made it possible to significantly reduce FEC size and due to it the radiation length of cards is about 3% X/X_0 (+ about 3% new cooling system). Another significant advantage of the new FEC is their ability to work with both positive and negative polarity of input signals. This feature will be useful in the future with a planned upgrade of ROCs from MWPC to GEM detectors.

Necessity not only to reduce the amount of material at the TPC end-caps, but also to distribute it evenly, has been forced to develop a new card from two boards (Fig. 3.3.7). The first board (Fig. 3.3.7, right) contains two SAMPA chips giving in total of 64 independent registration channels. The SAMPA amplifies the analog signal from the TPC pads, digitizes it with a 10-bit sampling ADC with a frequency of 10 MHz, processes it when the signal processor is enabled and transmits via serial links.

The second board (see Fig. 3.3.7, left) is a FEC controller. It is based on CYCLONE V GX FPGA. The FPGA performs the following main functions: high-speed bidirectional serial interface with the controller (up to 2.5 Gbps), SAMPAs management and configuration, data receiving from SAMPAs, FEC slow control features.

The first tests of the FECs showed their suitability for usage as TPC electronics. FPGA utilization in the data acquisition system provides us with great opportunities to further improvement of the system. The implementation of the FEC in the form of a double-desk board also gives us additional flexibility in the future upgrade of the system. If necessary, the controller part of the FEC can be replaced with another card, for example, with a flash-based FPGA (if it will be necessary due to radiation hard conditions of electronics operation).

3.3.7 TPC assembly and infrastructure

Since the TPC field cage containment cylinders are not differ significantly each form other in size the TPC assembling will be done at horizontal position of each elements. The arrangement for TPC assembling is shown schematically in Fig. 3.3.8. The pair of precisely positioned rails placed on at surface, the strong "arm" I-beam with adjustable module, a system of three mobile and a special mobile platform create mechanical structure for step-by-step assembling of the TPC field cage elements.

The special assembly tooling was manufactured at Mechanical and Instrument Engineering Corporation (Bryansk, Russia) and was delivered to LHEP (see Fig. 3.3.9).

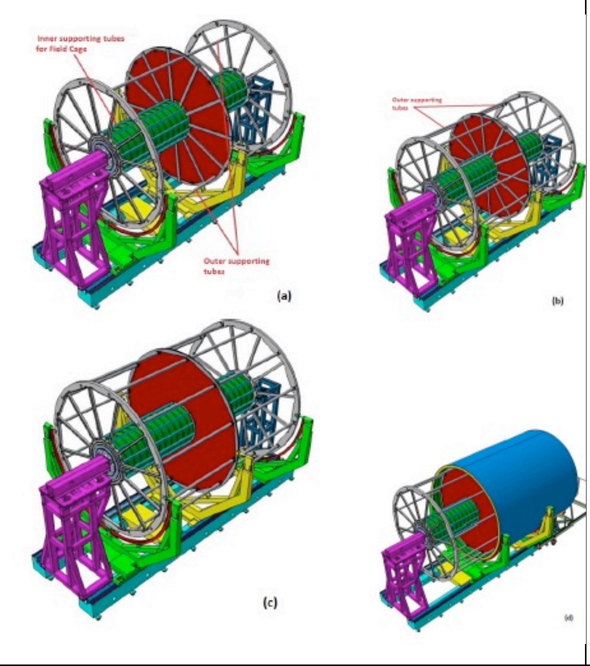

Fig. 3.3.8. TPC assembly steps

Fig. 3.3.9. Manufactured TPC assembly tooling

TPC assembly hall has been built for TPC assembly and testing. The common view of Bld.217 and general layout of the TPC assembly hall are shown in Fig. 3.3.10.

Fig. 3.3.10. Building 217 common view and TPC gas supply system

The hall has the clean area for the TPC assembling and two rooms for experimental equipment such as gas supply and regeneration system, cooling system, high voltage and the LV power supplies and so on. The clean room has square about 7 m x 12 m = 84 m^2 and air purity class 1000/ISO6.

3.4 TOF identification system

The Time-of-Flight detector is basic charged hadrons identification system of multipurpose detector. In base configuration, the TOF will be represented as a barrel – cylinder length of about 6 meters and diameter of 3 meters assembled of 28 modules (Fig. 3.4.1). Each module contains 10 MRPC detectors (Fig. 3.4.2). The TOF detector system is organized in a modular way in order to minimize the number of components and cost. In addition to the TOF modules, the system includes the following service subsystems: low and high voltage power supplies, gas system, data acquisition electronics, cooling and slow control. Start configuration of the TOF system should be commissioned in 2020.

3.4.1 Multigap resistive plate chambers

Each TOF module consists of 10 identical multigap resistive plate chambers with 24 readout channels each. Development and testing of MRPC prototypes were performed in period of 2013 – 2017. We tested several different versions of MRPCs with cosmic rays and deuteron beam of Nuclotron. The final version of MRPC made of commercial float glass with a thickness of 280 um. It has 15 gas gaps and provides time resolution around 50 ps.

During 2017-2018, all materials for the production of such MRPCs were purchased. Before mass production began, we had more than 90% of all necessary materials. Mass production of detector and modules started at the beginning of 2019. At the end of 2019, the production of 120 detectors and 10 modules will be completed. All modules production should be completed in 2020.

From the beginning of 2020, all TOF modules will be tested on cosmic rays stand, which was designed and commissioned especially for this goal in 2019.

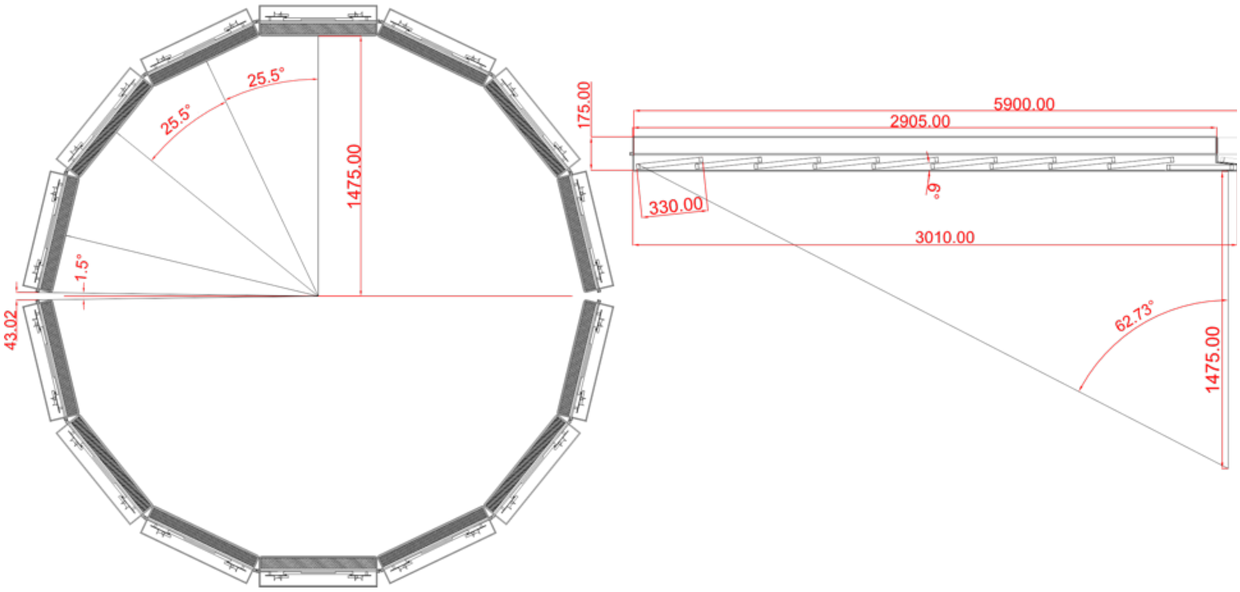

Fig. 3.4.1. Scheme of the TOF system barrel with overall dimensions.

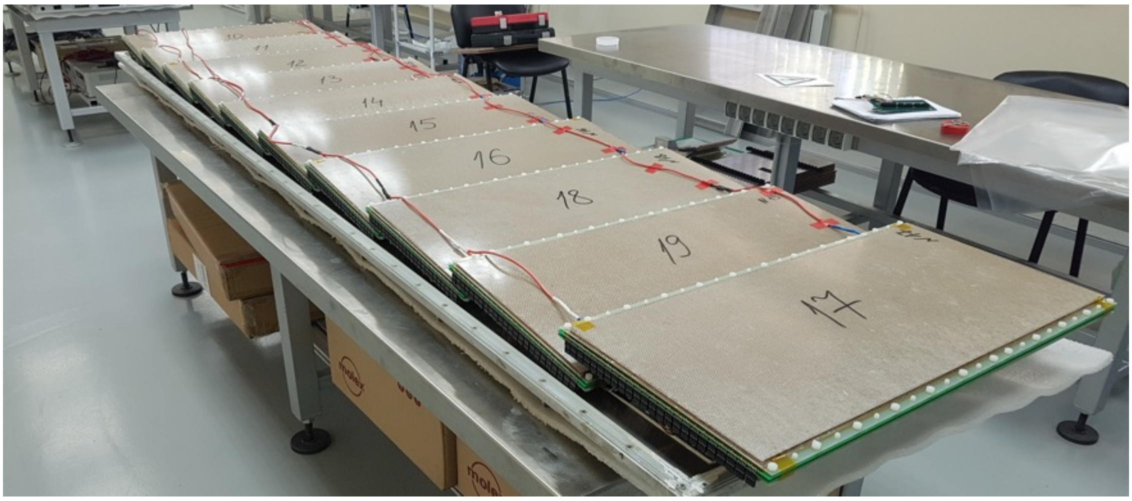

Fig. 3.4.2. Arrangement of MRPC detectors in the TOF module.

3.4.2 *Front-end electronics*

For the TOF MPD the 24-channel NINO based preamplifier board was developed [3] during 2015 – 2017. This preamplifier board is especially adapted for the two-side strip readout in MRPC at the MPD experiment. Overall dimensions of the preamplifier are 196.5 x 89 mm^2 (Fig.3.4.3). Distinctive features of the MPD TOF preamplifier board are stabilized voltage supply of the NINO, the input impedance matched to impedance of the MRPC, capacitors at the inputs for two-side strip readout, the threshold remote monitoring and control, and the board and the gas space thermal monitoring.

The production and testing of all necessary (560 pcs) preamplifiers is completed at the end of 2019.

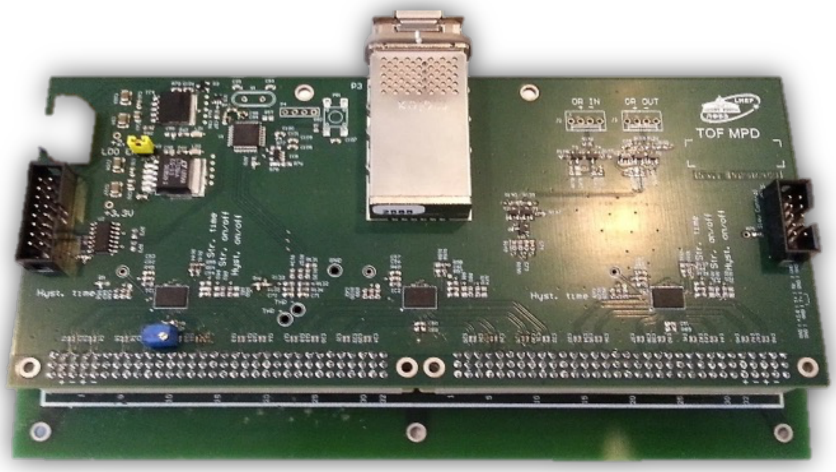

Fig. 3.4.3. 24-channel NINO based preamplifier board with the CXP output connector.

3.4.3 *Readout and data acquisition electronics*

New VME64x VXS time-to-digital converter TDC72VHLv4 based on HPTDC chip was designed for MPD TOF and FFD readout. It is used for digitizing LVDS signals coming from the output of the NINO amplifier using cables Molex P/N 11102512xx with connectors Molex 76105-0585. Time sampling of the TDC72VHLv4 is 24.4 ps per bin. The TDC72VHLv4 provides the ability of the precise “White Rabbit” synchronization with other timing devices. The total necessary amount of the TDC for the TOF MPD is 196 (14 modules per each of 14 VME crates).

All VME crates was purchased and delivered in 2017-2019. The TDC72VHLv4 boards are in production from the beginning of 2019. Currently, 51 TDC boards are available and tested. Production, calibration and testing of readout electronics is planned to be completed by mid-2020. Signal cables are delivered un full in 2018.

3.4.4 Closed loop gas supply system

The TOF detectors will be operated with a non-flammable Freon rich gas mixture containing 90% $C_2H_2F_4$ + 5% i-C_4H_{10} + 5% SF_6. The total gas volume of the barrel is approximately 3000 liters taking into account the volume occupied by detectors. It was decided to use a closed-circuit gas supply system, due to large gas volume.

Design and production of the gas system lasted from 2017 to 2019. At the moment, the system is in operation and is used for the TOF test stand on cosmic rays. After checking all the modules by the end of summer 2020, it is planned to transfer the system to building 17 and make minor changes to its design.

3.4.5 Slow control system

The Time-of-Flight system of the MPD is necessary to monitor several parameters of different subsystems such as temperature monitoring, voltage and current monitoring, gas flow monitoring, etc. At present, most of the slow control system has been developed and continues to develop. Some of the slow control equipment will be acquired already during the assembly of the TOF in MPD.

The development of the SCS of the TOF is planned to be done in the period 2018 – 2021.

3.4.6 Integration in MPD

The installation of the TOF will begin after the finishing of the ECal installation. Each module will be inserted in their position on both sides of the yoke of magnet. This will be done by means of a mobile support structure. The structure is equipped with adjustable rails of the same kind used inside the MPD barrel. To insert a module into the barrel it is enough to suspend the support structure with the hall crane in front of the chosen services sector and connect the rails together to form a unique sliding line that will allow pushing the module into the right position.

The design of part of integration equipment if finished. The production and assembling of integration devices in the MPD hall should be finished in summer 2020.

3.5. The Status of the FFD

The Fast Forward Detector (FFD) is important part of the MPD facility at the NICA collider [1] and its aim is to provide fast trigger of nucleus – nucleus collisions in center of the MPD setup and T0 pulse for TOF detector. The concept and technical details of the FFD are described in FFD TDR.

The block scheme of the FFD system, shown in Fig. 3.5.1, consists of two identical sub-detectors FFD_E and FFD_W based on 20 Cherenkov modules each, two units of sub-detector electronics (SDU) processing detector pulses, a trigger vertex electronics unit (VU), readout electronics, a picosecond laser calibration system, HV power supply, a detector control system (DCS), a cable system, a cooling system.

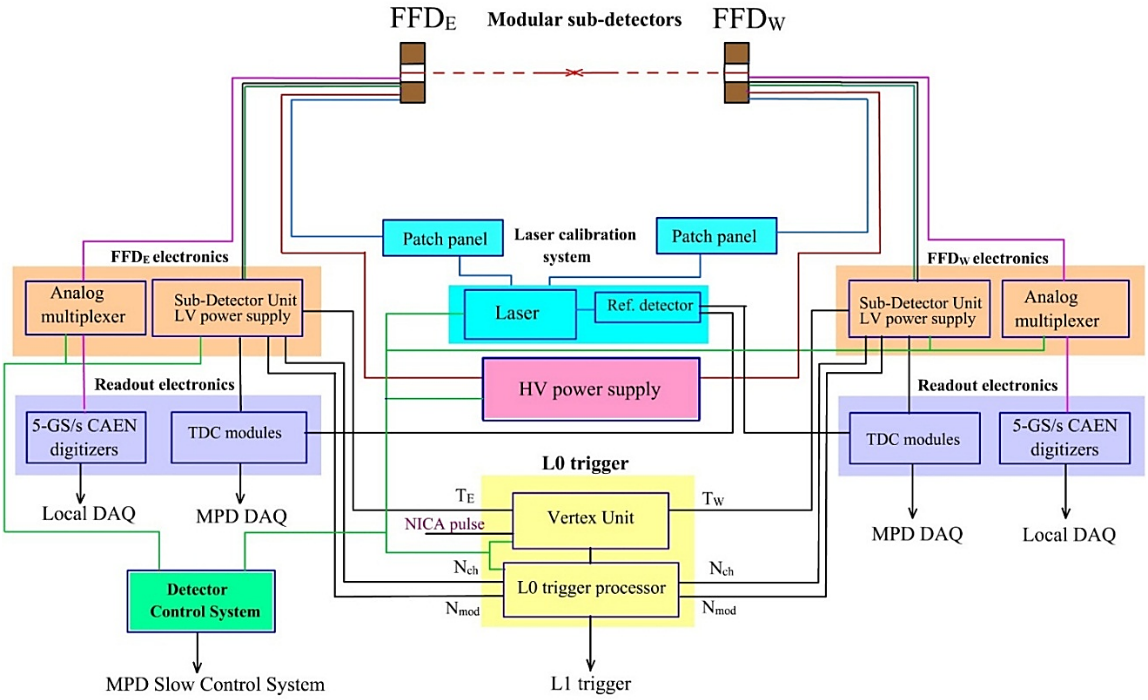

Fig. 3.5.1. A block-diagram scheme of the FFD system.

3.5.1 FFD sub-detectors

Each FFD sub-detector consists of 20 identical Cherenkov modules with 100- channel granularity. Each module consists of a 10- mm lead plate converter, four quartz bars of radiator, a photodetector MCP-PMT XP85012/A1, front-end electronics board, HV divider, module housing with connectors and cables.

In period of 2013 – 2017 several different versions of prototypes of FFD modules were developed and tested with LED, cosmic rays, deuteron beam of Nuclotron and in magnetic field up to 0.9 T. As a result of these studies, we define a final choice of quartz radiator dimensions, front-end electronics scheme, a regime of MCP-PMT operation, type and length of cables, and a housing design. A view of the module is shown in Fig. 3.5.2.

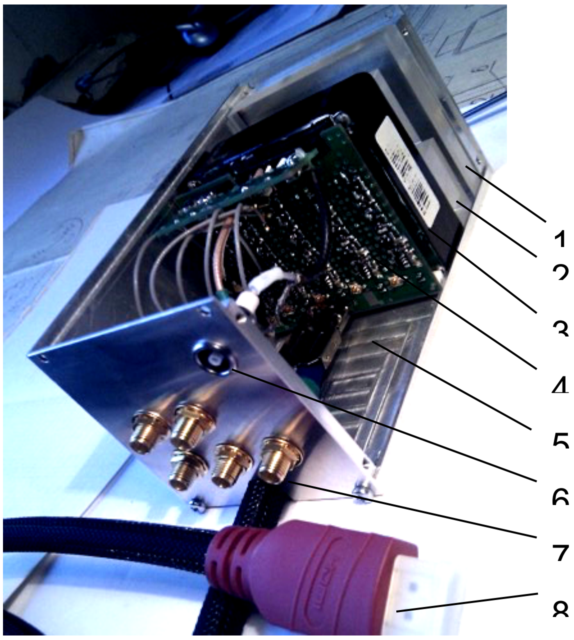

Fig. 3.5.2. A view of FFD module: 1 – the lead plate, 2 – the quartz bars, 3 – MCP-PMT XP85012/A1, 4 – the FEE board, 5 – the module housing, 6 – the HV connector, 7 – the SMA outputs of analog signals, 8 – the HDMI cable.

The obtained time resolution of individual channel of FFD module with cables and electronics used in MPD is $\sigma_{FFD} \approx 44$ ps and it is better than 50 ps required for TOF system. Some results of the test measurements have been reported and published.

All main elements of the modules were purchased and produced including MCP-PMT XP85012/A1 (41 units), quartz radiators (160 units), and lead converters (40 units).

2018 – 2019 is a period of module production. It includes design, production and tests of front-end electronics boards, HV dividers, module housings and cables. Some special mechanical elements of the modules are produced with 3D printer in our group.

A view of sub-detector design is shown in Fig. 3.5.3

2020 is period of assembly of FFD sub-detectors and test measurements with a stand created in 2019 for final tests with cosmic rays. The stand consists of four scintillation planes 50 ×50 cm^2 with silicon photomultiplier readout, lead absorber, trigger electronics and readout electronics.

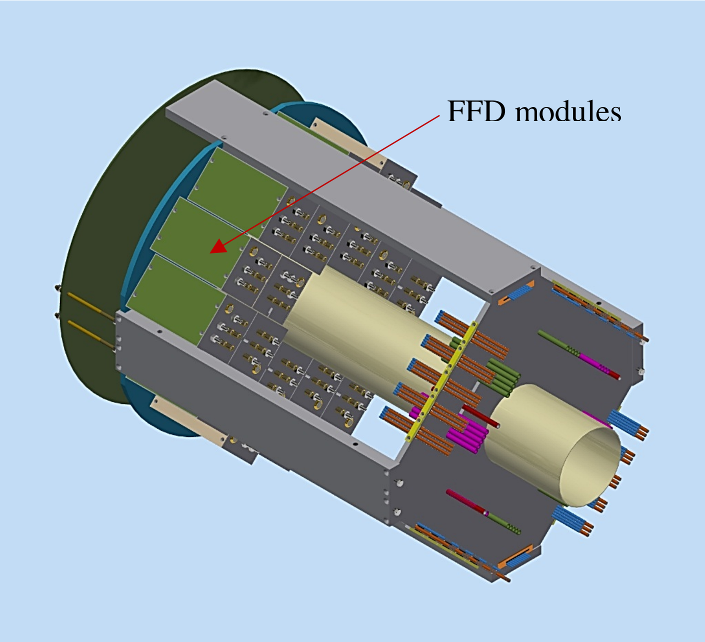

Fig. 3.5.3. Design of the FFD sub-detector

3.5.2 Sub-detector electronics

The SDU has a modular structure; it contains a set of modules placed in a VME crate having a custom back-plain. The set of modules includes a LV power supply Module (LVM), a Signal Processing Module (SPM), a Central Processing Module (CPM) and an Interface Module (IM). To provide fast FPGA configuration file downloading each module containing FPGA is equipped with the FPGA Configuration Loading Module (CLM) connected directly to a serial link interface. The backplane contains a parallel bus to control all modules located in the SDU crate using full-duplex multi-drop RS485 serial line and inter-module connections for fast signals and LV power lines between LVM and SPM.

Analog Multiplexer Modules (AMMs) are used for monitoring FFD channel operation. The inputs are connected to individual analog channels and output pulses are fed to digitizers.

Final project of the SDU was developed in 2016 – 2018. This year is period of module prototyping and tests. Also, two VME crate with power supplies were purchased. 2020 is period of module production and final tests.

3.5.3 Vertex electronics

The Vertex Unit (VU) uses preprocessed data coming from the both SDUs (SDUE, SDUW). The VU consists of a Vertex Unit Module (VUM) and an Interface Module located in a VME crate with a custom backplane. Concept of this unit was developed in 2016 – 2018. Production and tests will be made in 2020 – 2021.

3.5.4 . Readout electronics

The main readout electronics of FFD is based on TDC72VHL sitting in VME crates of TOF detector. The LVDS pulses are fed from SDUs to TDC inputs using cables Molex P/N 11102512xx with connectors Molex 76105-0585.

The FFD local DAQ, used for FFD regime adjustment and monitoring, is based on 5- GS/s 16-inputs digitizers, CAEN mod. N6742. It consists of 2 NIM crates with 4 digitizer modules in each; optical cables AY2730 and PC optical link CAEN A3818C. All this equipment was purchased and delivered in 2017. Tests of readout electronics with FFD sub-detectors will be done in 2020.

3.5.5. Calibration system

A special system based on PiLas laser with 30-ps pulse width and 405- nm wavelength is used for precision time calibration of FFD channels and monitoring the detector operation. Main parts of the system are a PiLas control unit, a box with laser head and optical system, quartz fiber bundles, patch boxes and optical cables, a reference photodetector with MCP-PMT PP0365G. A view of the elements (besides the optical fiber bundles) is shown in Fig. 3.5.4.

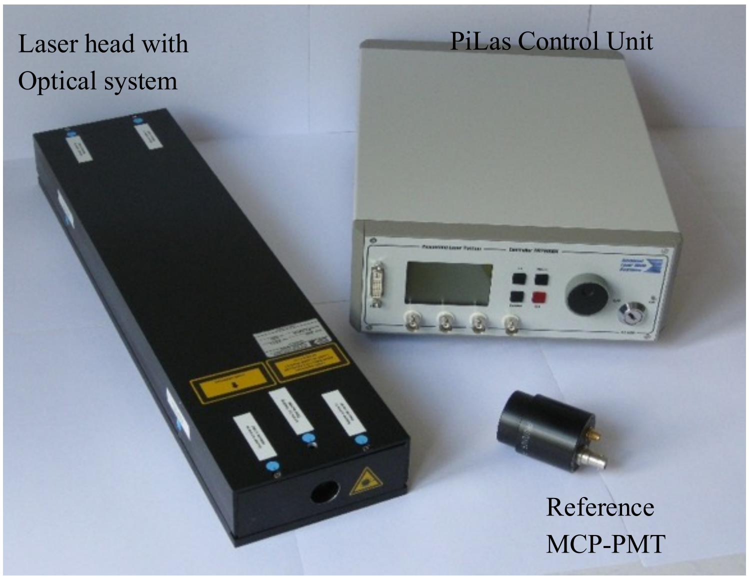

Fig. 3.5.4. A view of the PiLas control unit, the box with laser head and optical system, and the photodetector MCP-PMT PP0365G.

In period 2013 -2019 all elements of the system were purchased and produced. In 2019 we began test measurements with the laser system and final tests will be done in 2020 with FFD sub-detectors.

3.5.6. **Integration in MPD**

The installation of the FFD sub-detectors is made together with silicon detectors of ITS and vacuum tube using a special support cylinder for mechanical hardness. The design is in progress. The location of crates with SDU electronics and optical patch boxes must be close to cable outlets of MPD magnet and to TOF crates. Other FFD crates and equipment are located in a rack on the second floor of MPD overpass.

The deadline of production of FFD sub-detectors and all sub-systems is the end of 2020 and 2021 is the period of final tests and installation.

3.6 Forward Hadron Calorimeter (FHCal)

JINR and INR RAS (Moscow). This detector is one of the basic elements of MPD setup and is intended for the measurements of the geometry of heavy ion collisions. The main purpose of the FHCal is to provide an experimental measurement of a heavy-ion collision centrality (impact parameter) and orientation of its reaction plane. Precise event by-event estimate of these basic observables is crucial for many physics phenomena studies to be performed with the MPD experiment.

FHCal consists of two identical arms placed upstream and downstream the beam collision point. The modular structure of one FHCal arm is presented in Fig. 3.6.1. Since the heavy fragments escape into beam holes, it is not possible to discriminate the central and peripheral collisions using only the deposited energies in FHCal. The subdivision of the calorimeter into two, inner and outer parts (see Fig. 1), and the calculation of the energy depositions E_{in} and E_{out} separately in these calorimeter parts allows the construction of new observable, energy asymmetry: $A_E = (E_{in} - E_{out})/(E_{in} + E_{out})$. Taking the two-dimensional correlation between the energy asymmetry, A_E and full energy deposition in calorimeter, it is possible to resolve the ambiguity in central and peripheral events, respectively.

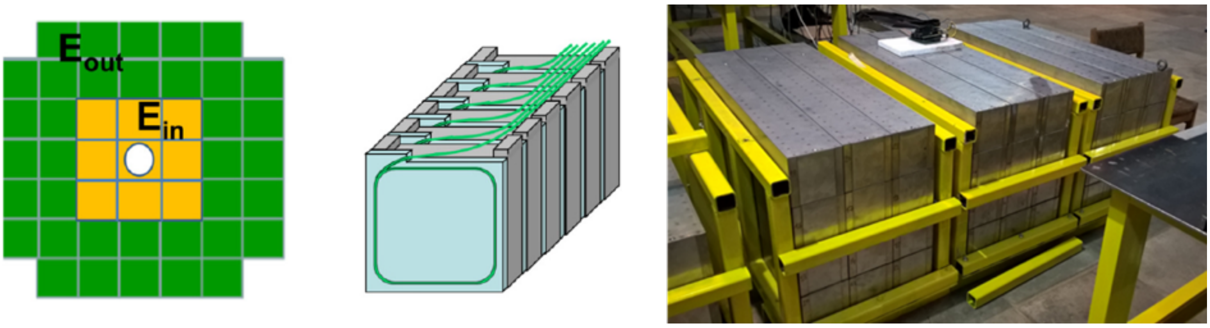

*Fig. 3.6.1. Left— Front view of FHCal structure. It is subdivided into two (inner/outer) parts for the measurements of centrality. Center — structure of the individual module. Right – stack of produced modules ready for deliv*ery to JINR.

3.6.1 FHCal module design

The FHCal module transverse sizes of 15 × 15 cm2 were chosen to match the size of the hadron showers. Each FHCal module includes 42 lead-scintillator sandwiches with a sampling ratio 4:1 (the thickness of lead plates and scintillator tiles is 16 mm and 4 mm, respectively).

Light readout is provided by WLS-fibers embedded in the grooves in the scintillator tiles, this ensures high efficiency and uniformity of the light collection over the scintillator tiles within a few percent. WLS fibers Y-11(200) with double cladding and a 1 mm diameter produced by Kuraray Co. were used for the FHCal assembling. To avoid the loss of light the bending radius of the WLS fiber must be larger than 5 cm. Spiral grooves in the scintillator tiles provide slightly better parameters than the circular ones, that is why they were selected to design the FHCal modules. One end of the WLS-fiber inside the scintillator grove is mirrored by silver paint, this improves the light collection by about 30%.

Each scintillator tile is covered with a white reflector (TYVEK paper) to improve light collection. WLS-fibers from each of 6 consecutive scintillator tiles are collected together in the optical connector at the end of the module and polished to improve the optical contact with the photodetector. The longitudinal segmentation in 7 sections requires the same number of optical connectors and compensates the nonuniformity of the light collection along the module caused by different lengths of the WLS-fibers.

All 42 layers of lead/scintillator sandwiches of the FHCal module are loaded into the box made of 0.5 mm stainless steel sheet and tied together in one block with a length of about 90 cm (4 nuclear interaction lengths) by a 0.5 mm stainless steel tape. After assemblage the module is covered by another similar stainless steel box and these two up and down boxes are spot-welded providing a mechanically stable construction. The weight of each module is about 200 kg.

Each module of hadron calorimeter consists of 42 lead–scintillator tile sandwiches with the sampling ratio 4 : 1 (thickness of the lead plates and scintillator tiles are 16 and 4 mm, respectively) that satisfies the compensation condition. According to simulation, the sampling fluctuations provide the energy resolution of calorimeter as: $\sigma_E/E \sim \surd\ 55\%/E$ (GeV) The beam tests of the calorimeter with the same sampling confirm the results of simulation.

To optimize the light collection efficiency from the scintillators some R&Ds on the groove shapes were performed. Namely, a few types of the scintillator tiles were produced with circular and spiral grooves. The tests of all tiles were performed with ^{90}Sr β-source and trigger counter below the scintillator tile to detect electrons passed through the scintillator. The outer end of WLS fiber was glued into special optical connector that was viewed by Hamamatsu MPPC. The measurements of the light amplitude were done with the step of 2 cm along the diagonal of the scintillator. The results of measurements are shown in Fig. 3.6.2. One can see that both circular and spiral grooves give similar results with the light yield of about 20 photoelectrons with 5% average space nonuniformity in the light collection. The spiral groove provides slightly better parameters and have been selected for the design of FHCal modules. The tiles are wrapped in reflector TYVEC.

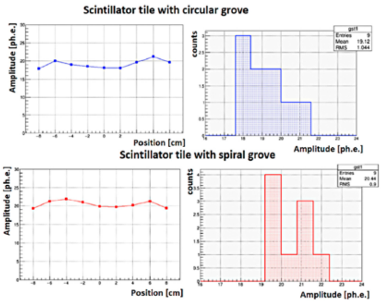

Fig. 3.6.2. The light yield along the diagonal of scintillators with different types of the groves. TYVEC reflector was used for the measurements.

3.6.2. Readout of the FHCal modules

The longitudinal segmentation of the calorimeter modules requires 7 compact photodetectors coupled to the optical connectors at the rear side of the module. The use of silicon photomultipliers, SiPMs, is an optimum choice due to their remarkable properties such as high internal gain, compactness, low cost and immunity to magnetic fields. SiPMs have no nuclear counter effect due to their pixel structure. Hamamatsu MPPC S12572-010C/P with a pixel size of 10x10 mm^2 were selected to ensure a high dynamic range of detected energies. The Front-End-Electronics (FEE) used for the MPPC readout includes an amplifier and a shaper with differential output signals. Due to the shaper, the signal length is about 0.2 □s which is a few times longer than the original signal width after the phtotodetectors. The necessity of a longer signal is related to the relatively low sampling frequency of the pipe-line ADC that digitizes the signal waveform. At present, a 64-channel 62.5 MS/s ADC64s2 board manufactured by the Dubna company AFI Electronics is used. The described readout scheme was used in beam tests of the FHCal modules at low proton energies.

3.6.3. FHCal energy calibration

The individual calibration of longitudinal sections is essential for the monitoring of the light yield behavior. After module assembling, the light yield of all longitudinal sections was measured by using cosmic muons crossing all 7 sections in a module (Fig. 2.2.1.43 (a)). Unfortunately, the statistics of such horizontal muons is very pure that requires a few days of data acquisition. Therefore, other types of muons tracks passed through two or three neighbor sections were considered. The double or triple signal coincidences allow the reliable identification of muon tracks in the presence of electronic noises compared with the muon signal in a single section.

Fig. 2.2.1.43 (b) shows the light outputs for all sections of one of the modules. One can see a higher light yield for the last section, where the length of the WLS-fibers is the shortest. The observed dependence is a simple reflection of the light attenuation during the transportation in WLS-fibers. As seen, muons deposit about 40 photoelectrons/section making it possible to calibrate the energy scale of FCHal modules during calorimeter operation in MPD setup.

At present, all 90 FHCal modules are assembled at INR (Moscow) and are ready for the delivery to JINR, see Fig. 3.6.3 right. A few spare modules are in production now.

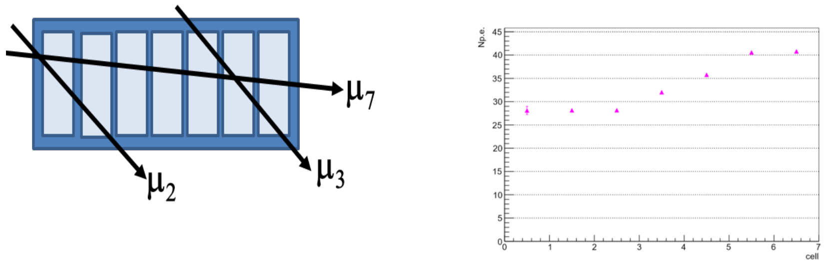

(a) (b)

Fig. 3.6.3. (a) – scheme muon tracks selected for the tests. Lower index denotes the number of sections passed by muons. (b)-light output in each of longitudinal section for one of modules.

3.7 ECal detector

The main goals of the calorimeter are the participation in particles identification (namely - final cleaning of the selected e+- sample) and measurements of the photons flux as well as reconstruction of some decays with participation of the photons. The final result depends on performances of other MPD detectors like TPC and TOF.

3.7.1 Design of the ECal

Large-sized (6-meters-long and 4.5-meters in diameter) electromagnetic barrel calorimeter (ECal) is an important part of the Multy-Purpose Detector (MPD) at heavy-ion NICA collider that covers the central pseudorapidity region of $|\eta|<1.2$ (Fig. 27). ECal is optimized to provide precise spatial and energy measurements for photons and electrons in the energy range from about 40 MeV to 2-3 GeV. To deal with a high multiplicity of secondary particles from Au-Au reaction, ECal has a fine segmentation and consists of 38 400 cells -"towers", (Fig. 3.7.1). Taking all requirements (high energy resolution, large enough distance to the vertex, small Moliere radius, ability to work in the high magnetic field, high time resolution, resistance to radiation, and reasonable price) into consideration, a "shashlyk"-type electromagnetic calorimeter was selected. Each "tower" has a sandwich structure of 210 polystyrene scintillator and 210 lead plates with 16 Wave Length Shifting (WLS) fibers that penetrate the plates to collect the scintillation light; the thickness of each scintillator plate is 1.5 mm, and the thickness of lead plate is 0.3 mm (Fig. 3.7.2).

Design of the ECal was done on the basis of many MC studies that were performed during last years. As the result of MC studies, a decision was taken to build the calorimeter with the projective geometry (Fig. 2.2.1.46) which is more complicated to construct than the simple structure that was planned in the beginning of ECal project (in the 2014). The main advantage of the new design is reduction of dead zones, increase of detector efficiency, improvement of linearity and energy resolution of the calorimeter measurements in conditions of high multiplicity of secondary particles from collisions of heavy ions. In the same time, the new design of the calorimeter is more

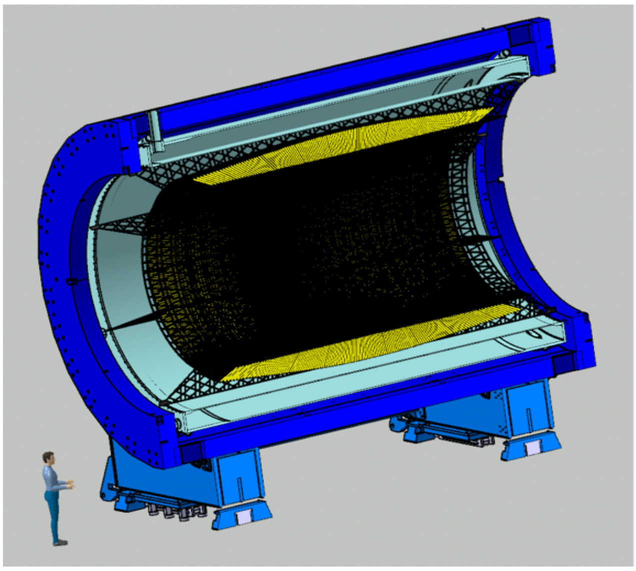

Fig. 3.7.1. View of the ECal inside of the Solenoid

complicated and demands more engineering efforts. Calorimeter modules production become more complex and time-consuming, and requires more manpower. The above-mentioned problems resulted in some delay in the preparation of the mass production of the calorimeter modules.

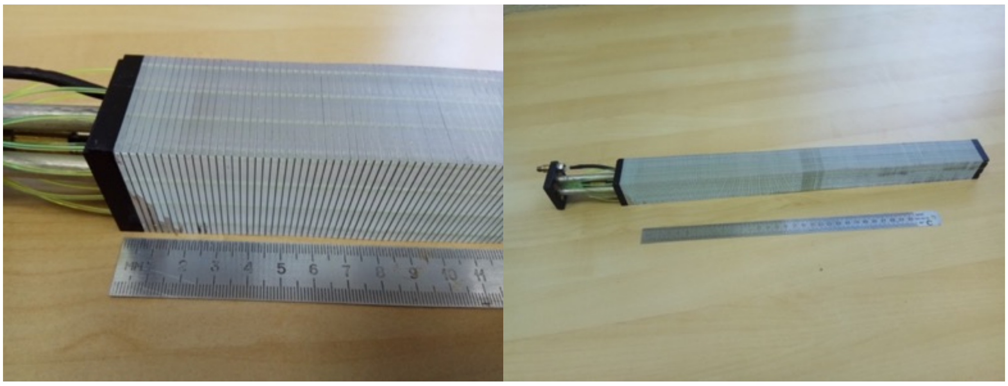

Fig. 3.7.2. Foto of the tower for ECal

Design of the ECal was done on the basis of many MC studies that were performed during last years. As the result of MC studies, a decision was taken to build the calorimeter with the projective geometry (Fig. 3.7.3) which is more complicated to construct than the simple structure that was planned in the beginning of ECal project (in 2014). The main advantage of the new design is reduction of dead zones, increase of detector efficiency, improvement of linearity and energy resolution of the calorimeter measurements in conditions of high multiplicity of secondary particles from collisions of heavy ions. In the same time, the new design of the calorimeter is more complicated and demands more engineering efforts. Calorimeter modules production become more complex and time-consuming, and requires more manpower. The above-mentioned problems resulted in some delay in the preparation of the mass production of the calorimeter modules.

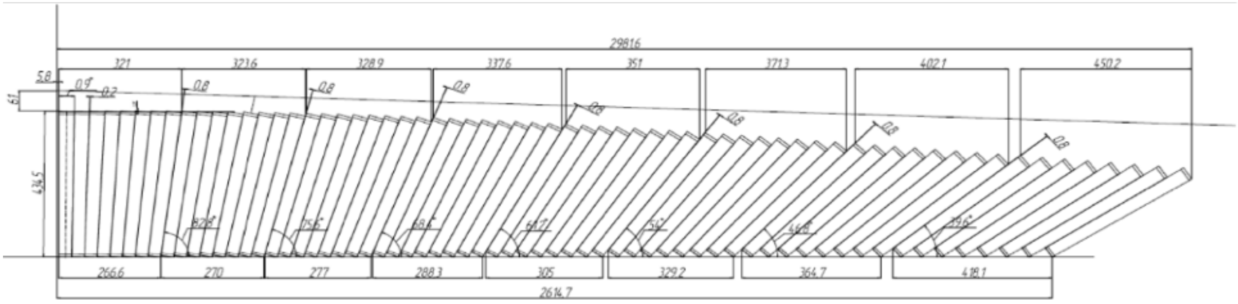

Fig. 3.7.3. Arrangement of the towers in the half-sector of the electromagnetic calorimeter with the projective geometry.

Each electromagnetic calorimeter module consists of 16 towers that are glued together. The geometry of each module depends on the module Z-coordinate location in respect to the beam interception point. To detect scintillation light that is collected by the 16 Wave Length Shifting (WLS) fibers that are passing through the holes in the scintillator and lead tiles, Hamamatsu S13360-6025 MAPD units were selected (with 6×6 mm^2 sensitive area). Few modules of the new design (Fig. 3.7.4) have been produced and carefully tested using test beams and cosmic rays (Fig. 3.7.5). Results of the tests are in the reasonable agreement with MC predictions.

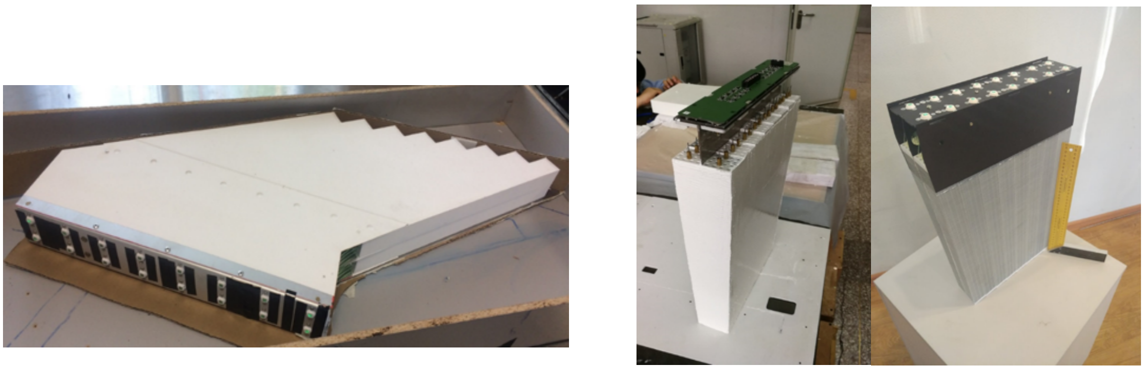

Fig. 3.7.4. Prototype modules. On the bottom-left panel, the readout electronics board is shown.

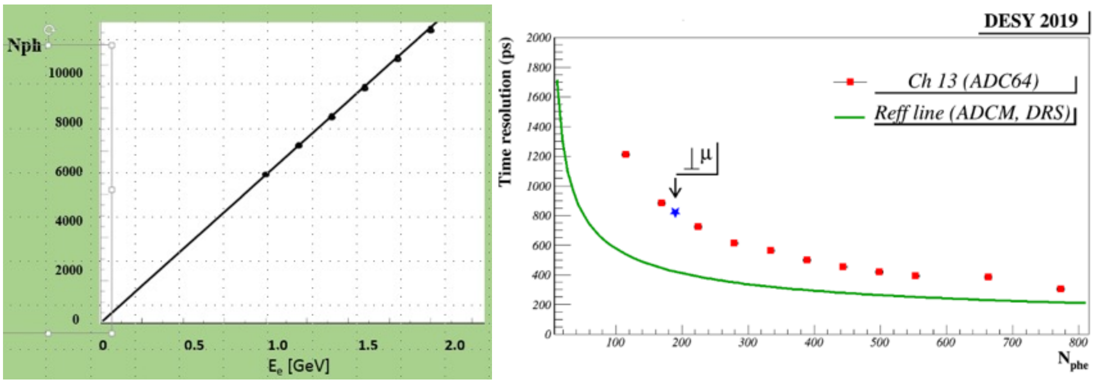

Fig. 3.7.5. Linearity of the light output (left panel) and the time resolution (right panel) of the ECal module prototype. Results from the prototype modules tests with electron beam and cosmics.

Now, all engineering documentation for the mass production of the eight types of the calorimeter modules is completed and sent to the manufacturers of ECal modules. Two companies (Polypak in Dubna and Uniplast in Vladimir) produced 10 million scintillation plates that is 100% of the total ECal need. Polipak produced a complete set of tightening covers for module towers and crowns (to form output windows of WLS fibers) to cover the total ECal need. WLS fibers to cover Russian quota of the modules production were purchased from Kuraray company. A glue-paint for gluing the towers into the modules was developed, and its production is managed. A technology for reflective coating application on lead plates was developed and adopted by two companies.

Russian quota of modules production (25%) should be completed in one year (viz., in the middle of 2020). The production of remaining modules in China cannot be finished before the end of 2020.

Geometrically, ECal is organized into 25 sectors or 50 half-sectors. Each half-sector (Fig. 3.7.6) contains 48 modules (of 8 different types) that are glued into a fiberglass container (basket) as well as correspondent readout and slow-control electronics with total mass of about 1.5 ton. Model calculations demonstrate that the cell structure of the basket with 2-mm-thick walls provides enough strength and rigidity to keep all possible deformations of the half-sector under its own weight under 0.5 mm for all possible orientations of half-sector in space. At the moment, a contract of production of 52 baskets is in the stage of final signing; we expect that 16 baskets will be delivered to JINR by October 2020, and whole number of baskets is expected to be delivered by Summer 2021.

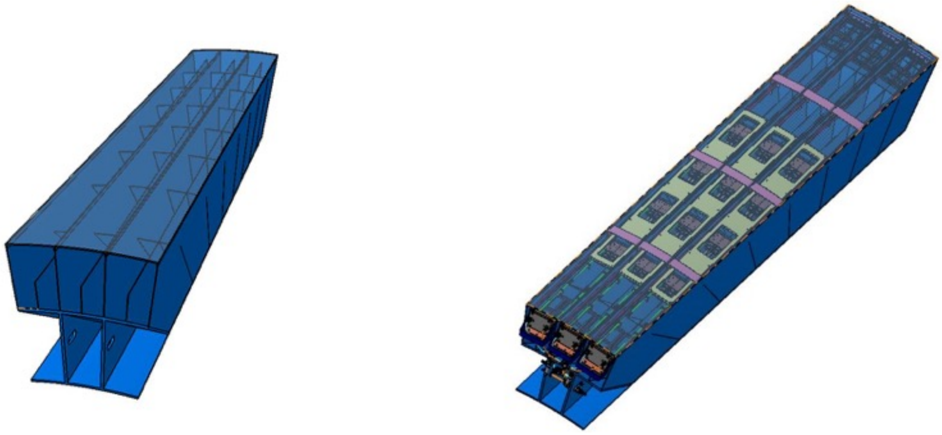

Fig. 3.7.6. ECal basket (left panel). Right panel shows the basket with installed readout electronics.

3.7.2 FE electronics

Front-End (FE) electronics will be located directly on the calorimeter. This solution is chosen due to the listed bellow advantages:

- small path of analog signal to FE means less signal distortion and pickup noises;
- much simpler transport of digital signal from the calorimeter to the event building electronics; number of connectors between FE boards and electronics outside detector falls from 1536 (number of channels per sectors) in case of analog signal transport falls to 24 (number of channels per sector / number of channels in ADC board (64)) in case of digital signal transport. In the latter case we use very thin optical cable;
- very high event read out rate can be reached by using zero suppression and even signal processing directly on the FE board;
- one disadvantage of this solution is the need to extract the heat from the FE electronics out of MPD detector.

As a FE electronics unit we have designed and constructed ADC 64 channel board (Fig. 3.7.7).

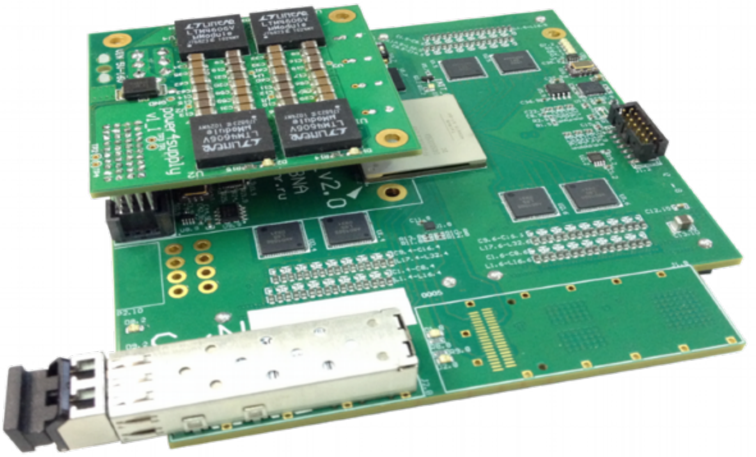

Fig. 3.7.7. ADC64s2 – Front-End board with ADCs amplifiers and Ethernet communicator.

ADC board is a waveform digitizer. It quantizes analogue input signal and samples it at fixed time intervals. Zero suppression logic is based on baseline estimation and threshold value. Signal shaping is performed in digital form with FIR filters. It allows to reduce the number of waveform points required for digital signal representation with minimum loss of accuracy. The ring type memory allows the read back of last 30 µs of waveforms. It sets the limit on trigger latency to this value.

ADC board allows to be integrated to the White Rabbit system. White Rabbit provides sub-nanosecond accuracy and picoseconds precision of synchronization for large distributed systems.

3.7.3 ECal integration

Originally, the electromagnetic calorimeter was planned as a self-supporting structure, where each sector contributes as a power element to the whole structure. But after splitting of the ECal modules production between Russian and Chinese sites (with different time schedules), ability to install and re-install calorimeter sectors (half-sectors) without whole calorimeter and MPD dismantle was requested. To meet this demand, we plan to use special support frame (about 8-meters-long and about 4.5-meters in diameter) made of carbon-fiber composite material that can hold whole load from MPD detectors without support from ECal sectors (Fig. 3.7.8). This frame will consist of inner (20-mm-thick) and outer (15-mm-thick) cylindrical shells with 25 bulkheads (10-mm-thick) in between them to form 25 cells for calorimeter sectors installation. Rigidity calculations for the simplified frame model were performed and demonstrates that the planned total load of 120 tons will cause maximum frame deformations of about 2-3 mm that meets our demand to have deformations below 5 mm to keep ability of installation and re-installation of ECal half-sectors. Strength calculations assures the frame ability to hold the load about 10 times higher than our maximal expectations, and durability calculations and tests assures 15-year frame operation. At the moment, a contract of the frame design and production is in the stage of final signing; we expect the frame delivery to JINR by the November 2020.

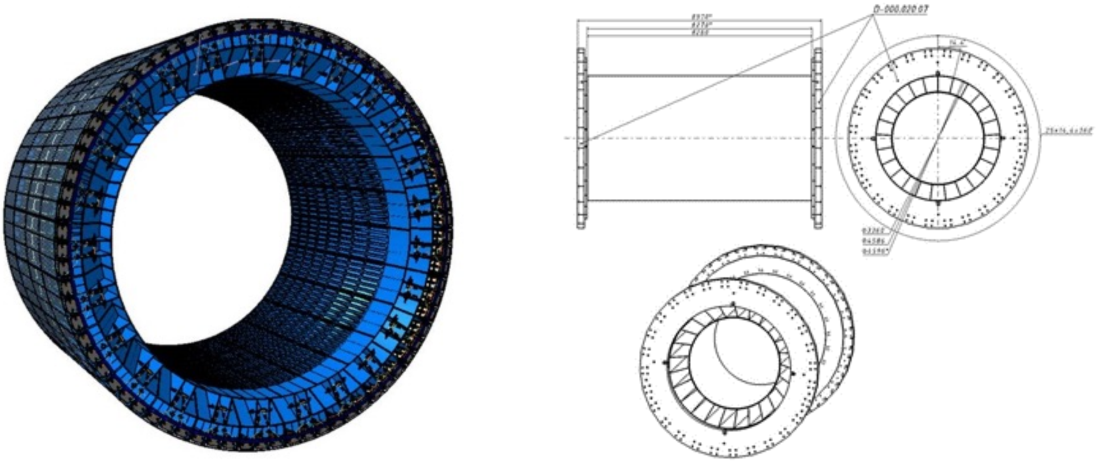

Fig. 37.8. The power frame of MPD. On the left panel, installed half-sectors are shown. The drawing on the right panel shows the frame fastening on the magnet support rings.

Readout and slow-control electronics have been developed at JINR. Prototype modules were produced and tested. Mass production of electronics will start in following months to be completed to the time of the calorimeter assembling in the second half of 2020. Production is distributed among Russian (readout electronics) and Chinese (slow control and preamplifiers) companies. Now, big efforts of the ECal group are concentrated on the development of an innovative system for installation and replacements of the calorimeter electronics without the calorimeter dismantle. In this system, all heating parts of electronics are located inside the cooling boxes with ventilation, preamplifier boards with SiPMs outside the boxes use them as support structures, and these three-meters-long boxes are mounted on the rails in the half-sectors and can be moved in and out the calorimeter. Most complicated engineering problem in this design is to match reliably and with high precision (better than 0.5 mm) output windows of WLS bundles on the calorimeter modules with correspondent SiPMs on the preamplifier boards. Prototype of moving box with precise positioning for electronics is under test now at JINR. Water cooling system for the ECal electronics is designed and under expertise of the MPD electronics group.

3.8 The Inner Tracking System ITS

The Inner Tracking System *(the ITS)* had been always considered as an important subsystem of the MPD which, however, due to its technical complexity and large cost could not have been included in the list the MPD sub-systems of the basic configuration. Such shaky status of the MPD ITS lasted until the moment the Protocol # 134 between CERN and JINR stating the legal terms for transaction of CERN developed novel technology and the know-how for building the MPD-ITS on the basis of Monolithic Active Sensors *(the MAPS*) ALPIDE was signed in 2018. This document laid a clear road towards the MPD ITS, probably, to be the most technologically sophisticated among all the detector systems being built at JINR.

The Multi-Purpose Detector (*the MPD*) is being constructed to study the properties of extremely dense nuclear matter formed in relativistic nucleus-nucleus collisions at NICA energies. The yields of strange and charmed particles are the important observables sensitive to critical phenomena in phase transitions of the QGP-matter at high net-baryon density. Highly efficient registration of such short-lived products of nuclear interactions using a vertex silicon detector will play a key role in the analysis of the possible onset of deconfinement enforced by fluctuations of dense nuclear matter under critical conditions. Without the MPD ITS studies of processes within the charmed sector are impossible.

The conceptional layout of the MPD ITS (Fig. 3.8.1) repeats the one used by the ALICE ITS2 but with number of layers of the ALIDE sensors reduced from seven (ALICE ITS2) to five (MPD ITS) due to much smaller diameter of the bore of the MPD TPC (500 mm). The MPD ITS will consist of two barrels with layers of different thickness and quite different construction of the support/cooling structure of the Outer (OB) and the Inner (IB) barrels.

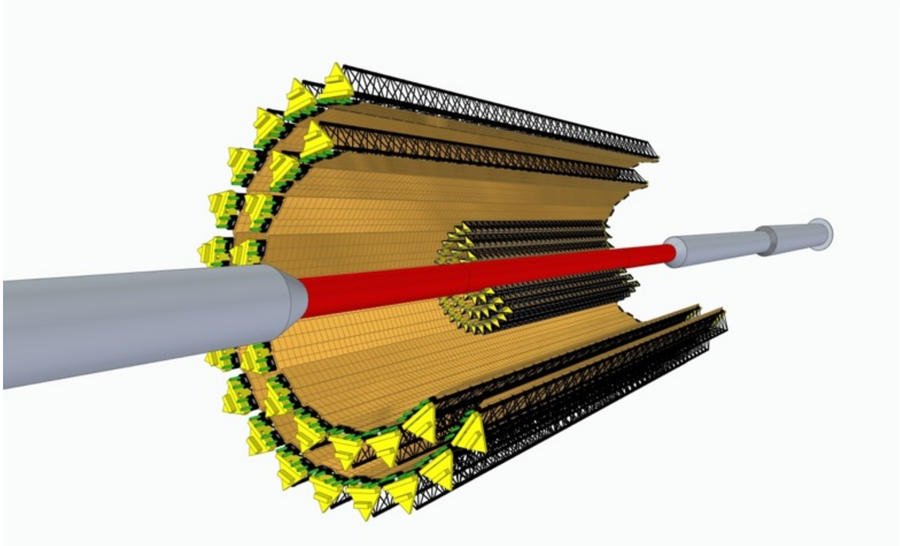

Fig. 3.8.1. The conceptional layout of the ITS around a thin-wall MPD beampipe

The IB barrel comprises three most thin layers of MAPS. The design of the IB is proposed to be a subject of CERN and JINR joint R@D effort scheduled for 2020 -2023. The expected thickness of these layers is 50 um of Si equivalent.

It is well known that two basic parameters i.e. the distance from the interaction point to the first layer and the thicknesses of the first three layers of tracker determine the ability of tracker to resolve secondary vertices of the decaying charmed particles. The smaller these parameters are the higher the resolution of the decay vertex from the primary one.

The requirement for reduction of the beampipe diameter contradicts the collider designers’ natural wish to operate during the commissioning of the NICA with beampipes of increased diameter. This allows them more easily to tune a new machine. After a long series of debates a compromise was found between the MPD ITS and NICA accelerator contradictory work plans. The joint plan put forward was as follows for the MPD ITS:

- installation of the OB only with the beampipe of 64 mm diameter in 2022-2023;
- exchange of the beampipe to smaller diameter after the collider tuning time will be over (2024-2025);
- adding of the IB to the existing configuration with the beampipe of reduced diameter start of the experiments with charmed probes in 2025.

3.9 The MPD thin-wall beampipe

One of the most critical elements of the NICA MPD project is nine meters long thin-wall UHV compatible beampipe depicted in Fig. 3.9.1. Manufacturing of the MPD beampipe is a very complex. The LHC experiments gained enough experience in design and production of similar unique pipes the outer rare parts of which are made of aluminum while the central part of beryllium. The typical minimal wall thickness reached so far is 800 um both for beryllium and aluminum parts. Russian company Composit – Beryllium Institute has produced two samples of beryllium part 1700 mm in length. The thickness of the wall is 1 mm.

The outer parts of the beam pipe will be made of special alloy of aluminum.

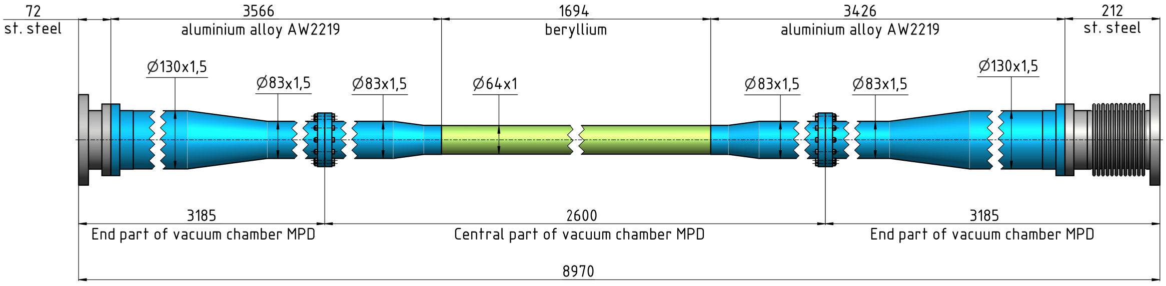

Fig. 3.9.1. A tentative design of the MPD beam pipe. Absent is any indication of the vacuum equipment at the rare ends of the beampipe. According to the integration scenario the beampipe is baked at the vacuum stand and filled in with dry Neon and only then is shipped to the assembly stand c/o the MPD ITS team.

3.10 MPD Data Acquisition (DAQ) system and computer cluster

The core function of the DAQ system is realization of data transfer from the detector to the storage system. It includes the data flow from readout electronics to the First Level Processor (FLP) fabric, to the Event Building (EB), High Level Trigger (HLT) and to the Storage System. Main DAQ components are data transfer networks, data processing servers, online storage system, software packages, network communication protocols and data formats. Readout electronics interface, Clock and time synchronization (Timing) System, Trigger System are also included in MPD DAQ system.

3.10.1 DAQ Electronics

TDC Based Readout used for TOF and FFD subdetectors of MPD. Both subdetectors use similar DAQ architecture – CRU16 as Local Trigger Units (LTU) for trigger distribution and VXS crates for installing Detector Readout Electronics (DRE) –TTVXS and TDC72VHL modules (Fig. 3.10.1). In each VXS crate will be installed one TTVXS module.

There are total of 14 VXS Crates planned for TOF DAQ. In each crate will be installed 1 TTVXS module and 14 TDC72VHL modules. TTVXS module is a Time and Trigger Unit (TTU). It receives trigger information from its LTU, synchronization from Clock and Timing Network (White Rabbit Network) and controlled via Front-End Control Network. Inside VXS crate TTU distribute trigger and synchronous clock to DREs (TDC72VHL). DREs sends busy signals in reply to trigger back to TTU. Also, TTU monitors status of every DRE (voltages, temperature and etc). TTU and DRE sends data via 1Gb Ethernet, 1 link per module.

FFD DAQ is similar to TOF DAQ, but it uses 2 VXS crates and 5 DREs (TDC72VHL) per crate.

TTVXS is a Time and Trigger Unit (TTU) for VXS crate. It distributes trigger information and system synchronous clock to installed payload modules. Also, TTVXS module collects busy information from all payload modules. Connection topology is star. TTVXS and each payload module connects with 1 serial bidirectional link with speed up to 2.5 Gb/s, 1 bidirectional LVDS link, 1 LVDS link for transmitting and 1 LVDS link for receiving. All LVDS links speed is up to 125 Mb/s.

TTVXS has SMBus link to all payload modules for monitoring its status. TTVXS can transmit this information via Ethernet 10/100M.

TTVXS has 4 SFP+ connections for receiving synchronization and receiving trigger information from corresponding networks and send event data to data readout network. Connections speed can be up to 10 Gb/s. This module has 6 programmable input-output LVTTL coaxial connectors. Functions of this connection is not fully defined yet and it is subject to discus.

Fig 3.10.1. TTVXS (left) and TDC72VHL (right) modules

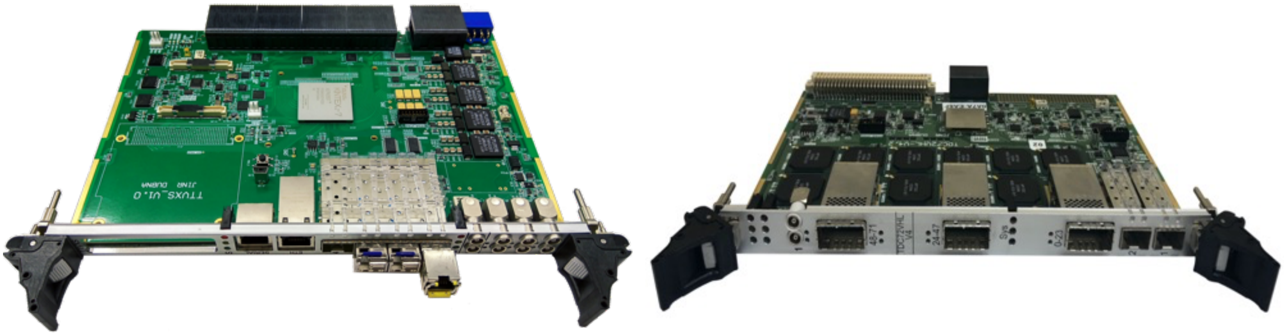

TDC DRE board performs time-stamping of discrete signals (hits) with typical accuracy of 20 ps. It is based on HPTDC chip. Hit timestamps are kept for 104 μs in ring type memory. The total trigger latency should not exceed this value.

120 TDC72VHL modules and 4 TTVXS modules will be produced and tested till the and of 2019 year for MPD TOF testing stand. 80 TDC72VHL modules and 16 TTVXS modules will be produced in 2020.

ADC DRE board is a waveform digitizer. It quantizes analogue input signal and samples it at fixed time intervals. Zero suppression logic is based on baseline estimation and threshold value. Signal shaping is performed in digital form with FIR filters. It allows to reduce the number of waveform points required for digital signal representation with minimum loss of accuracy. The ring type memory allows the read back of last 30 μs of waveforms. It sets the limit on trigger latency to this value.

ADC64ECal electronic module designed for digitizing signal form ECal and FHCal detectors. It's a 64-channels 14bit 62.5 Msps waveform digitizer with Digital Signal Processing core. Every module has 2 optical links (primary and reserve) for time synchronization, trigger distribution and readout data. The board is made in the form factor, which allows to locate the module into the special box for electronics inside the magnet. Electromagnetic tolerant and radiation hard components are applied in the ADC64Ecal. 15 modules are produced and tested. 20 modules will be produced till the end of 2019 year and 100 modules in 2020.

4 modules will be placed inside the one box and custom Liquid Cooling System (LCS) is under design for cooling electronics (Fig. 3.10.2). LCS for 12 electronic modules will be produced and ready for the testing in the second quarter of 2020 year.

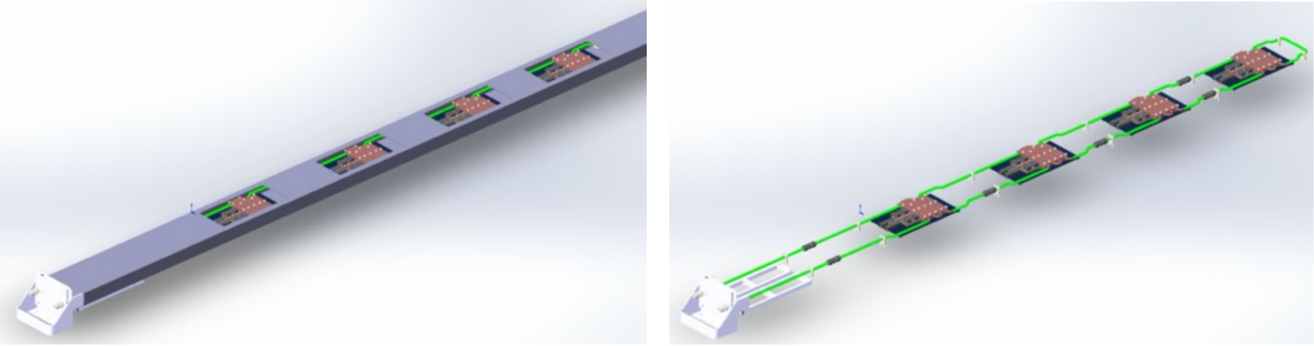

Fig. 3.10.2. Box for electronics with LCS (left) and ADC64Ecal with LCS in the box (right).

At the final configuration of MPD 600 modules ADC64Ecal (Fig. 3.10.3, left) will be used at ECal and 12 modules at FHCal. All these electronics must be synchronized and have the same trigger signal. Therefor CRU-16 is designed (Fig. 3.10.3, right). It's a common readout unit with White Rabbit support. It's capable to synchronize up to 16 modules, provide a trigger signals and collect the data form them. All collected data are transmitting to the switch, using 40 Gbps optical interface. 2 board are produced and tested and 10 modules will be produced in 2020.

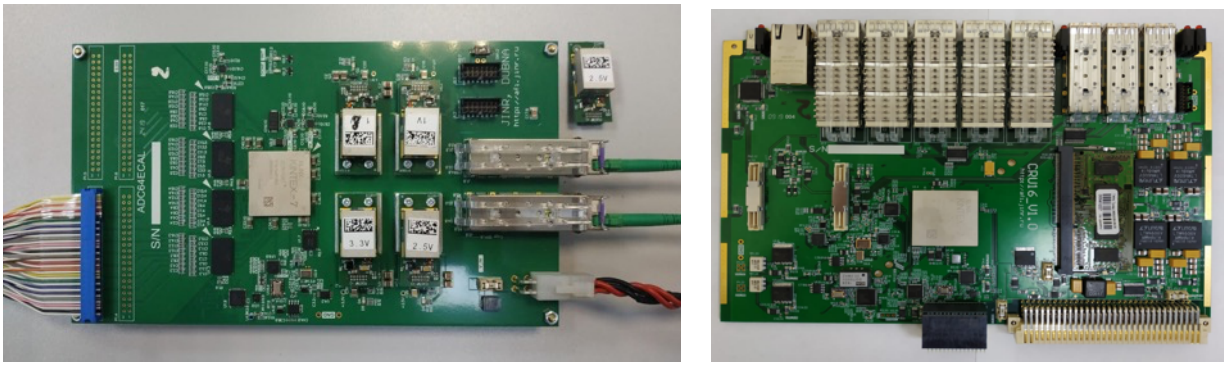

Fig. 3.10.3. ADC64ECal (left) and CRU-16 (right) electronic modules.

3.10.2 MPD DAQ network

On the present time a network equipment has bought for the MPD DAQ network (see network structure in Fig. 3.10.4). It is covering the test run needs, partially.

In 2020 will be planned to purchase:

- computing equipment FLP (480 cores) 10 servers;
- interim data storage TDS (must be required 500 TB of useable data volume) 10 servers;
- network equipment for a data acception from electronics and for a infrastructure needs

in quantity 12 switchs;

-servers for the MPD DAQ Network processes monitoring and logging in quantity 10 pieces.

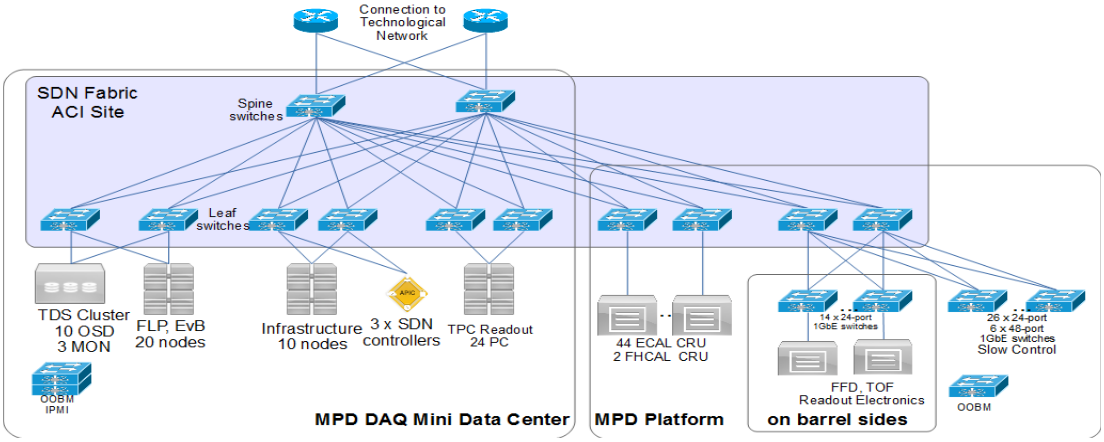

Fig. 3.10.4. MPD DAQ network structure.

Networking devices and DAQ electronics will be placed on and into the Barrel, at MPD platform and inside the MDC (see Fig. 3.10.5). At TPC, ECal and FHCal readout electronics will be placed into the Barrel. The data from these detectors will be transmitted to the network devices for TPC and to the CRU-16 modules for ECal and FHCal by optical links. Network devices and CRU-16 modules will be placed at the MPD platform. All aggregated by CRU-16 modules data will be transmitted to the MDC. Network devices and DRE at TOF and FFD detectors will be placed on the Barrel, around it. The data path is: from the DRE to the Network switches at platform, and from the Network switches to the MCD.

Fig. 3.10.5. MPD DAQ Network and DAQ Electronics location.

3.10.3 MPD Mini Data Center (MCD) and Control Room

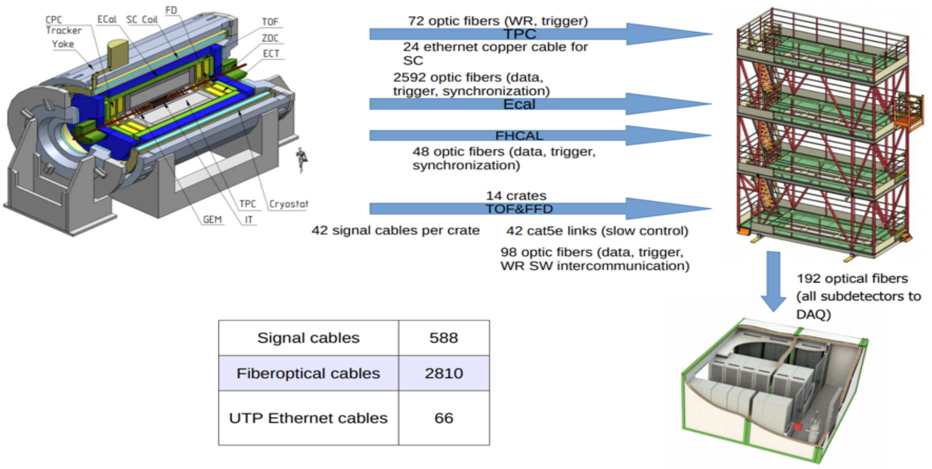

Signal cables	588
Fiberoptical cables	2810
UTP Ethernet cables	66

The contract for MCD and Control Room (see Fig. 3.10.6) production was concluded in 2019. Commissioning the Control Room set with the MCD for a test usage are planned in 2020.

MDC specifications:

- input power consumption – 160 kW;
- IT power consumption – 50 kW (N+1)/70 kWmax;

- rack count – 7 racks;
- redundancy – N+1 (UPS, HVAC);
- battery backup time – 15 minutes;
- rack size – 600 x 1200 x 42U.
- Control Room specifications:
- number of operator places – 20;
- redundancy – N+1 (UPS);
- battery backup time – 15 minutes.

Ventilation, air conditioning, fire extinguishing, access control and video surveillance systems will be present.

White Rabbit provides sub-nanosecond accuracy and picoseconds precision of synchronization for large distributed systems. It also allows for deterministic and reliable data delivery. DRE boards digitize detector signals using common notion of time and frequency provided by the White Rabbit (WR) network. The time reference is provided by GPS/GLONASS receiver and backup precision frequency reference (Cesium or Rubidium clock). Timing Network structure and WR switches test stand are shown in Fig. 3.10.7.

Fig. 3.10.6. MCD (up) and Control Room (down)

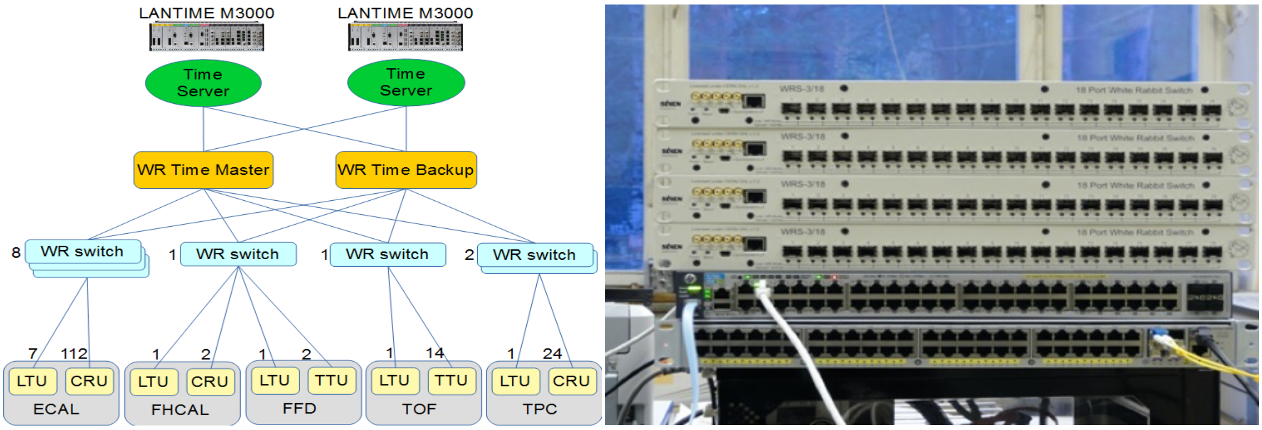

Fig. 3.10.7. The MPD Timing Network structure (left) and WR switches test stand (right)

10 WR switches were purchased till the end of 2019 and 10 will be purchased in 2020.

3.10.4 MPD DAQ software

Each program participating in the experiment has its own configuration. A record in configuration is a data structure composed of a **field** and **value** pairs, named *document,* for example:

Document A : {program name : run control, ← field : value
status: run, ← field : value
devices: {Document B, Document C, …}, ← field : value
… }

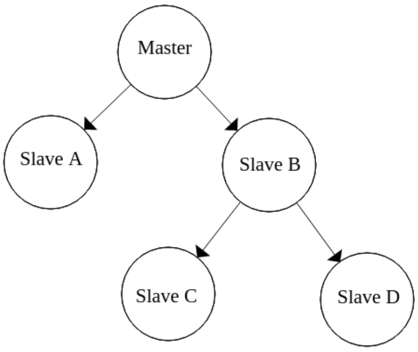

It means that we design data in JSON-like documents. This is more expressive and powerful than the traditional row/record model. A typical number of documents in each program is 10 – 500, depth from 5 and more layers. We entrusted the management of such a data structure to the Mongo document-oriented database, which is open source. Programs participating in the experiment also represent a tree structure, like the left picture. Commands are transmitted from program to program on this tree from the parent program (run control program).

In the first and the second quarter of 2019 in all programs was added a function to recording there configurations to Mongo database. It was introduced a new entity called ***Run***. *Run* is the parallel launch of several programs (typical 10 - 50), which are connected to each other in a tree structure and consistently perform one task. Also, we taught our programs to transfer their configurations up to the tree. What did it give us:

- we know exactly with what configuration programs were launched, and this information will not be lost after experiment.
- now we can restart the *Run* with exactly the same configurations.

In late 2019 – early 2020 planned to develop software for combining all previously written applications under single application monitoring (AM). Assumed, that this program will be able to monitor about 10-50 other programs (subprograms). It will contain the necessary information for a successful reproduction of subprograms.

The main functions will be:

- launch remote programs; aggregation, logging and visual representation of errors that occurred, during *Run;*
- work with the configuration database: applying previously saved configurations to executable subprograms;
- to help user understanding a hierarchical structure of *Run*.

DevFlashProg. This program can connect to ethernet device and write firmware image file into device flash memory and/or verify it. A log information is written in corresponding database after every success write.

PNP protocol. Any program that takes part in a run control system sends specific package to multicast. Another can find out what program is running at this moment and some information about it, host and port of TCP-server for remote control or with outgoing data.

MLDP protocol. All our ethernet devices support MLDP protocol. It allows up to avoid binding devices to the IP-address in programs. MLDP-message contains IP address, serial number, device type and other useful information. All our ethernet devices periodically sends it over multicast. One program can receive it and find out on what address we should establish a connection.

Mstream. This program receives data packages from ethernet device, perform defragmentation of MStream data blocks, packs them into MpdRawData format and transmit them to outgoing TCP-server. In future it is planned to integrate this logic into control programs as separate threads.

Event builder. The task of this program is to collect data from several client programs (mstream program or another event builder), separate event blocks in every data flow, combines them together per events and further retransmits or writes to the file as united data block.

TDC control. This program sets up TDC72VXS device with proper configuration. Among the main parameter there are channel enable, readout window, trigger source. In debug mode it is capable to make specific adjustment of HPTDC setup. Although it starts mstream subprogram for reading data. In the future it is planned to make it as a slave of run control system.

TTVXS control. This program sets up TTVXS device with proper configuration. Among the main parameter there are enable slots of VME crate, trigger source. Although it starts mstream subprogram for reading data from this block. In the future it is planned to make it as a slave of run control system.

ADC64. This program sets up ADC-like devices with proper configuration. Among the main parameter there are channel enable, readout window, trigger source, DSP (digital signal processing) logic and sparse readout. This program can read data from device, visualize them and save data as an ASCII file. It is used just to prepare for run, in run execution adc64-system is used.

Adc64-system. This program writes configuration and handle data readout from list of ADC-like boards with error handle and remote control. This program can be used as slave one in run control system.

mpd-rawstat. This program can perform specific data/device tests: presence of all devices in the final data file, absence of significant time discrepancy, etc. Data can be obtained from reading a file or form specific TCP-server of event builder program (monitor output).

Adc64-viewer. This program is similar to mpd-rawstat, but it performs just quick visualization of any signal from adc-like devices. Data source can be a file or monitor output.

CRU control. At this moment this program is under design. This program will be able to configure corresponding device and integrate other programs into the run control system.

3.11. Engineering Support

The main task, which will be solved at the NICA accelerator complex, requires the design and construction of an experimental setup capable of: registration with high efficiency secondary particles born in the collision of heavy ion beams; identifying the type and determine the energy of particles; restoring the vertices of the primary interaction and the coordinates of the birth of secondary particles – Multi-Purpose Detector MPD. The MPD-PLATFORM (Fig. 3.11.1) is an important part of the NICA project infrastructure. Mechanically connected to the MPD, the PLATFORM is designed to provide working conditions for power supply systems, DAQ electronics, monitoring and control elements of the subdetectors.

Fig. 3.11.1. PLATFORM MPD Mechanical Support Structure with RACK's

3.11.1 Architecture of mechanical structure

The MPD mechanical support consists of:

- RACK – main module of the mechanical structure designed to assemble elements of a system;
- AUXILIARY RACK - COOLING UNIT – air/water heat exchanger designed for cooling equipment installed in the connected RACK;
- UNIT – group of mechanically connected RACKs (4 RACKs with 2 or 3 AUXILIARY RACK - COOLING UNIT);
- CONTAINER – of mechanically connected UNITs (8 RACKs with 5 AUXILIARY RACK - COOLING UNIT) installed at the same level;
- PLATFORM – movable mechanical structure consisting of four levels, called CONTAINERS and connected to MPD.

3.11.2 Technical description of equipment

The RACK (3.11.2) it is a demountable structure consisting of a steel frame, mounting rails with a distance between them 19”, removable front and rear doors and side panels. The doors are equipped with mechanical and electronic locks and are connected by a flexible protective conductor PE Protective Earth. A 600x1200x2200 RACK was selected with a usable height of 47U (1U = 1,75 inches). The total mass of the structure with embedded devices should not exceed 1 500 kg.

Fig. 3.11.2. RACK - the Main Module of the Mechanical Structure, AUXILIARY RACK - COOLING UNIT

The RACK standard equipment:

- **FAS F**ire **A**larm **S**ystem – early fire detection and accurate location of fire hazard at RACK level, active extinguisher system and smoke extraction system;
- **PMS P**LATFORM **M**anagement **S**ystem – real-time remote management and data acquisition;
- **IPD I**ntelligent **P**ower **D**istributor - power supply of devices installed in RACK. The control system performs the optimization of phase loading, provide overcurrent and electrical shock protection, failures detection, automatically switch-on and switch-off power of the devices and remote-control mode;
- **VAC V**entilating and **A**ir **C**onditioning – cooling system with closed air circulation in the RACK;
- **CCAS C**able **C**onnection **A**uthorization **S**ystem – marking cables with micro RFID elements and saving the described data in EqDb;
- **ACS A**ccess **C**ontrol **S**ystem – service technicians access managed by administrator to the RACKs using electronic keys registered in EqDb;
- Free space – 36U.

AUXILIARY RACK - COOLING UNIT 300x1200x47U can be installed with one or two RACKs. The control unit attempts to keep the temperature of the impelled cold air at 22 ° C. The necessary fan speed is determined and controlled by determining the temperature difference between the warm inlet and the cold outlet air (Fig. 3.11.3).

Fig. 3.11.3. Air routing

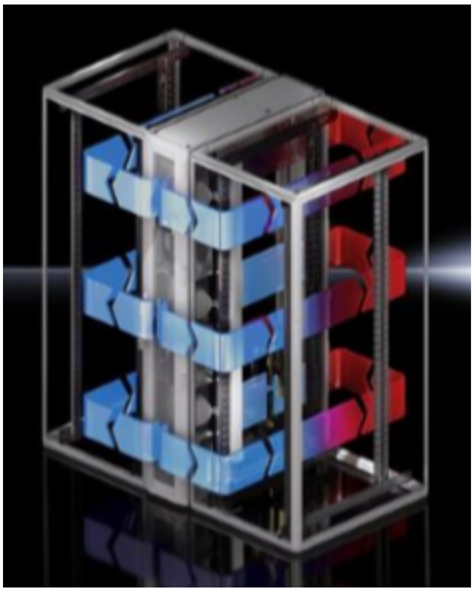

To achieve enough cooling in the server enclosure, it is important to ensure that the cooling air passes through the interior of the built-in units and is unable to flow past at the sides. To ensure targeted air routing in the system, the server enclosure is divided by foam strips into warm air and cold air section. Additionally, the system consisting of LCP DX, server enclosure and cold aisle containment should be well sealed to avoid a decrease of the cooling capacity due to mixing of cold and hot air. In addition, the system consisting of COOLING UNIT and attached RACK should be well sealed to avoid a decrease of the cooling capacity due cold air leakage. Existing cable entry glands are additionally sealed e.g. using suitable brush strips.

CONTAINER is a group of RACKs with its own infrastructure, which includes:

- **FAS - F**ire **A**larm **S**ystem – all closed spaces and cooling ventilation ducts will be equipped with appropriate smoke and fire detectors. All fire detectors will be connected to the global FAS-NICA system with automatic fire brigade notification system;
- **CRWS** - **C**able **R**ace **W**ay **S**ystem – cables arrangement on MPD-PLATFORM;
- **VAC** - **V**entilating and **A**ir **C**onditioning – COOLING UNITs are connected to external Ice-water aggregate;
- **CCTV - C**losed **C**ircuit **T**ele**V**ision – distributed system of weatherproof cameras in many locations, remotely controlled, connected to the CNNet converged IT network with writing data in EqDb;
- **SES** - **S**moke **E**xtraction **S**ystem – connection with smoke exhaust ventilation of the NICA complex building;
- **SAS** - **S**ound **A**lert **S**ystem – audio messages to personnel about hazards and the manner of the required response. Warnings should be accompanied by a light form e.g. flashing light with warning lamps.

PLATFORM is a four-tier steel structure, with a CONTAINER installed on each level.

LEVEL 1 (ELECTRIC DISTRIBUTOR) – power equipment, supplying MPD and the Platform itself. Power Supply automatically connect the PLATFORM NICA-MPD to one of two (working and emergency) Power Supply Lines 3 x 380 V, 50 Hz, 800 A (400kW). Further power distribution will be performed by a typical block provides 3 x 380 V, 50 Hz and 25 A at the output, which is enough to power one standard RACK.

LEVELs 2, 3 and 4 are for the SSC Slow Control System and DCS Detector Control System of the MPD-NICA project. The desired power consumption of the LEVELs 2 - 4 is about 200 kW.

3.11.3 Management

The control of the RACK takes place centrally from the Panel Operator in the WinCC SIEMENS SCADA system. There are two types of RACKs that can be handled remotely:

- RACK MASTER – manages all installed RACKs;
- RACK SLAVE – controlled from the MASTER RACK.

To facilitate the management of IT, a CLUSTER is a group of RACKS or devices installed in different RACKS, functionally designed for the same task and logically combined in the IT system that controls their structure.

EqDB – Equipment Database ORACLE. This EqDb system allows you to register administrative information, such as orders, deliveries and detector construction processes, the cost of its production, any movements of components for testing or maintenance. EqDb has a built-in connection authorization mechanism based on RFID Radio Frequency IDentification technology. EqDb works online with a slow control system and is an important element of technical support for the entire MPD-NICA project.

*CNNet **C**onvergent IT **N**ICA **Net**work* – interface for connecting the NICA-MPD-PLATFORM with the rest of the JINR network.

- remote administration at local and global levels;
- a virtual private network channel connecting CNNet to other cooperating DaCe Data Center, such as the WUT Warsaw University of Technology.

3.12 Integration in MPD

The installation of the TOF will begin after the finishing of the ECal installation. Each module will be inserted in their position on both sides of the yoke of magnet. This will be done by means of a mobile support structure. The structure is equipped with adjustable rails of the same kind used inside the MPD barrel. To insert a module into the barrel it is enough to suspend the support structure with the hall crane in front of the chosen services sector and connect the rails together to form a unique sliding line that will allow pushing the module into the right position.

The design of part of integration equipment if finished. The production and assembling of integration devices in the MPD hall should be finished in summer 2020. The Milestones of the MPD assembling is shown in table 3.12

Publications and Talks (2016-2020), MPD Subdetectors

TPC

Publications for 2016-2020

1. STATUS OF THE TIME PROJECTION CHAMBER FOR THE MPD/NICA PROJECT.
A.Averyanov et al, // International Journal of Humanities and Natural Sciences; ISSN:2500-1000, eISSN:2500-1086, "Capital", V. 1, part 2, pp.208-213, 2016.

http://intjournal.ru/wp-content/uploads/2016/11/Averyanov.pdf

2. TIME PROJECTION CHAMBER FOR MULTI-PURPOSE DETECTOR AT NICA.
A. Averyanov et al. // Acta Physica Polonica B (Proceedings Supplement), ISSN:1899-2358, Institute of Physics Jagellonian University, V.9, No.2, pp.155-164, 2016.

http://www.actaphys.uj.edu.pl/fulltext?series=Sup&vol=9&page=155

3. Time Projection Chamber for Multi Purpose Detector at NICA, Technical Design Report, rev.04. A. Averyanov et al. // Laboratory of High Energy Physics JINR, Dubna, 2016.

http://nica.jinr.ru/files/TDR_MPD/TpcTdr_26-05-2016.pdf

4. SAMPA chip: a new ASIC for the ALICE TPC and MCH upgrades.
S.H.I. Barboza, M. Bregant, V. Chambert, B. Espagnon, H.D. Hernandez Herrera, S.M. Mahmood,D. Moraes, M.G. Munhoz, G. Noël, A. Pilyar[1], P. Russo, B.C.S Sanches, G.J. Tambave,K.M.M. Tun-Lanoë, W. van Noije, A. Velure, S. Vereschagin[1], T.O. Weber and S. Zaporozhets[1] // J. Instrum. 2016. V. 11. C02088.

5. Front-End Electronics development for TPC detector in the MPD/NICA project.
G.Cheremukhina, S.Movchan, S.Vereschagin, S.Zaporozhets, // Journal Instrument, 12, C06031, 2017.

6. TPC status for MPD experiment of NICA project.

A.Averyanov et al.// Journal of Instrumentation (JINST), IOP Publishing Ltd and Sissa Medialab srl, V.12, No.06, C06047, 2017.

http://iopscience.iop.org/article/10.1088/1748-0221/12/06/C06047

7. SAMPA Chip: the New 32 Channels ASIC for the ALICE TPC and MCH Upgrades.

---

[1] JINR, LPHE, Dubna, Russia

J. Adolfsson (Lund U.),.., A. Pilyar (Dubna, JINR),.., S. Vereschagin (Dubna, JINR), S. Zaporozhets (Dubna, JINR) et al. // Journal of Instrumentation, 12-04-C04008 , ISSN:1748-0221, IOP Publishing, 2017.

8. Time-Projection Chamber Development for the Multi-Purpose Detector in the NICA Project. *A.V.Averyanov, et al. //* Physics of Particles and Nuclei, ISSN:1063-7796, Pleiades Publishing Ltd., V.49, No.4, pp.746-752, 2018.

https://link.springer.com/article/10.1134/S1063779618040093

9. Time Projection Chamber for Multi Purpose Detector at NICA,

Technical Design Report, rev.05 (v.6).

A. Averyanov et al. // Laboratory of High Energy Physics JINR, Dubna, 2017.

http://mpd.jinr.ru/wp-content/uploads/2017/05/TDR_TPC_v6_2017.pdf

10. Front-end electronics development for TPC detector in the MPD/NICA project.
G.Cheremukhina, S. Movchan, S. Vereschagin and S. Zaporozhets // J. Instrum. 2017,V. 12, C06031.

11. Readout electronics for TPC detector in the MPD/NICA project.
S.Movchan, A.Pilyar, S.Vereschagin, S.Zaporozhets. // Proceedings of the XXVI International Symposium on Nuclear Electronics & Computing (NEC'2017), Becici, Budva, Montenegro, September 25 - 29, 2017.

12. Time-Projection Chamber Development for Multi-Purpose Detector of NICA Project.
A. Averyanov et al. // Physics of Particles and Nuclei, ISSN:0367-2026, eISSN:1814-7445, JINR Publisher, V. 49, N 4, pp.1313-1325, 2018.

http://www1.jinr.ru/Pepan/v-49-4/49_Averyanov.pdf

13. Readout Electronics for TPC Detector in MPD/NICA Project.

G. Cheremukhina et al. // Springer Processings in Physics 212, Volume 1, pp.195-200, Aug. 2018.

https://link.springer.com/chapter/10.1007%2F978-981-13-1313-4_39

14. Front-End Electronics based on PASA and ALTRA chips.

A.Averyanov et al. // Addendum A1 to TPC/MPD TDR v.07, 2019.

http://mpd.jinr.ru/wp-content/uploads/2019/01/TpcTdrv07-AddA1-FEE.pdf

15. Time Projection Chamber for Multi Purpose Detector at NICA, Technical Design Report, rev.07. *A.Averyanov et al.* // Laboratory of High Energy Physics JINR, Dubna, 2019.

http://mpd.jinr.ru/wp-content/uploads/2019/01/TpcTdr-v07.pdf

16. Time-projection chamber for Multi-Purpose Detector of NICA project at JINR.

S. Vereschagin et al. // Nuclear Inst. and Methods in Physics Research A, Elsevier Science Limited, V.958, Article 162793, pp. 1-3, April 2020.

https://doi.org/10.1016/j.nima.2019.162793

Presentations at scientific conferences and seminars

1. TPC MPD/NICA readout electronics.

S.Vereschagin on behalf of the TPC-MPD/NICA collaboration // 119th session of the Scientific Council, JINR, Dubna, Russia, February 18 – 19, 2016.

2. Time Projection Chamber (TPC) status for (MPD) experiment at ion collider NICA.

A. Bazhazhin on behalf of the TPC-MPD/NICA collaboration // V annual conference of young scientists and specialists “Alushta-2016”, June 5-12, Alushta, Russia, 2016.

https://indico.jinr.ru/event/89/registrations/190/

3. Test results of the time-projection chamber (TPC) prototype for a multi-purpose detector (MPD) of the NICA megaproject.

A. Bazhazhin on behalf of the TPC-MPD/NICA collaboration // 50-th Annual Winter School on Physics, Petersburg Nuclear Physics Institute NRC KI, Saint-Petersburg, Russia, February 29 – March 5, 2016.

http://hepd.pnpi.spb.ru/WinterSchool/archive/2016/program_school.html

4. Time-projection chamber prototype (TPC) for multi-purpose detector (MPD) of NICA project. Prototype test results.

A. Bazhazhin on behalf of the TPC-MPD/NICA collaboration // 22 all-Russian scientific conference of physics-students and young scientists, Association of physics-students and young scientists of Russia, Rostov-on-Don, Russia, April 21-28, 2016.

5. Time-projection chamber (TPC) status for multi-purpose detector (MPD) of NICA project.

A. Bazhazhin on behalf of the TPC-MPD/NICA collaboration // L PNPI School on condensed state physics (CSP-2016)], PNPI NRC KI, Saint-Petersburg, Zelenogorsk, Russia, March14-19, 2016.

http://fks2016.pnpi.spb.ru/uploads/attachment/48/Бажажин_1.pdf

6. Simulation results of electric field shape in a drift volume of Time-projection chamber (TPC) for Multi-purpose detector (MPD) of NICA project.

A. Bazhazhin on behalf of the TPC-MPD/NICA collaboration // L PNPI School on condensed state physics (CSP-2016), PNPI NRC KI, Saint-Petersburg, Zelenogorsk, Russia, March 14-19, 2016.

http://fks2016.pnpi.spb.ru/uploads/attachment/46/Бажажин_5.pdf

7. The Time-Projection Chamber (TPC) for MPD/NICA experiment.

S.Vereschagin on behalf of the TPC-MPD/NICA collaboration // The 16th JINR-ISU Baikal Summer School on Physics of Elementary Particles and Astrophysics, village Bol`shie Koty (Big Cats) on the shores of the lake Baikal, Russia, July 8-15, 2016.

8. TPC readout chamber electronics for MPD.

S.Vereschagin // Laboratory seminar, LHEP, March 11, 2016.

9. TPC MPD/NICA readout electronics.

S.Vereschagin on behalf of the TPC-MPD/NICA collaboration // The XX International Scientific Conference of Young Scientists and Specialists (AYSS-2016), March 14-18, 2016.

10. Crosstalk and noise measurements of a charge-sensitive amplifier input path.

S.Vereschagin // V annual conference of young scientists and specialists “Alushta-2016”, June 5-12, OMUS, Alushta, Russia, 2016.

11. Crosstalk and noise measurements of a charge-sensitive amplifier input path.

S. Vereshagin on behalf of the TPC-MPD/NICA collaboration // Poster on the 45th regular meeting of the PAC for Particle Physics, 20-21 June 2016.

12. Front-end electronics development for TPC detector in the MPD/NICA project.

S. Vereschagin on behalf of the TPC-MPD/NICA collaboration // International Conference on Instrumentation for Colliding Beam Physics (INSTR17), Budker Institute of Nuclear Physics, Novosibirsk, Russia, February 27 – March 3, 2017.

https://indico.inp.nsk.su/event/8/session/9/contribution/43/material/slides/0.pdf

13. TPC status for MPD experiment at NICA project.

S.Movchan on behalf of the TPC-MPD/NICA collaboration // International Conference on Instrumentation for Colliding Beam Physics (INSTR17), Budker Institute of Nuclear Physics, Novosibirsk, Russia, February 27 – March 3, 2017.

http://indico.inp.nsk.su/event/8/session/3/contribution/131/material/slides/0.pdf

14. Time-projection chamber (TPC) status for multi-purpose detector (MPD) of NICA mega-project.

A. Bazhazhin on behalf of the TPC-MPD/NICA collaboration // VI annual conference of young scientists and specialists “Alushta-2017”, JINR, Alushta, Russia, June 12-19, 2017.

https://indico.jinr.ru/event/158/contributions/987/

15. Time-projection chamber (TPC) status for multi-purpose detector (MPD) of NICA mega-project.

A. Bazhazhin on behalf of the TPC-MPD/NICA collaboration // 51-th Annual Winter School of St.Petersburg Nuclear Physics Institute NRC KI, Saint-Petersburg, Russia, February 27 – March 4, 2017.

http://hepd.pnpi.spb.ru/WinterSchool/archive/2017/program_school.html

16. Status of Time Projection Chamber (TPC) for Multi-Purpose Detector (MPD) of NICA mega-project.

A. Bazhazhin on behalf of the TPC-MPD/NICA collaboration // 17th JINR-ISU Baikal Summer School on Physics of Elementary Particles and Astrophysics, JINR, Irkutsk State University, Irkutsk, Russia, July 13-20, 2017.

17. TPC assembly tolling and procedure.

A. Bazhazhin and V.V. Chepurnov on behalf of the TPC-MPD/NICA collaboration // The XXI International Scientific Conference of Young Scientists and Specialists (AYSS-2017), JINR, OMUS, Dubna, Russia, October 2-6, 2017.

18. Readout Electronics for the TPC Detector in the MPD/NICA Project.

S. Vereschagin on behalf of the TPC-MPD/NICA collaboration // The International conference on Technology and Instrumentation in Particle Physics 2017 (TIPP-2017), Beijing, China, May 22-26, 2017.

19. Time-projection chamber development for Multi-Purpose Detector in the NICA project.

S. Vereschagin on behalf of the TPC-MPD/NICA collaboration // International Session-Conference of the Section of Nuclear Physics of the Physical Sciences Department of the Russian Academy of Sciences "Physics of fundamental interactions" dedicated to 50th anniversary of Baksan Neutrino Observatory, June 6-8, Nalchik, Russia, 2017.

20. Readout electronics for TPC/MPD of NICA project.
S. Vereschagin on behalf of the TPC-MPD/NICA collaboration // VI annual conference of young scientists and specialists “Alushta-2017”, JINR, Alushta, Russia, June 12-19, 2017.
21. Readout electronics for the TPC/MPD of NICA project.
S. Vereschagin on behalf of the TPC-MPD/NICA collaboration // Poster, 47th meeting of the PAC for Particle Physics, 26 June, Dubna, Russia, 2017.
22. Time projection camber development for multi-purpose detector in the NICA project.
S. Vereschagin on behalf of the TPC-MPD/NICA collaboration // Scientific-methodological seminar, LHEP, September 14, 2017.
23. Readout electronics for TPC detector in the MPD/NICA project.
S. Vereschagin on behalf of the TPC-MPD/NICA collaboration // 26th Symposium on Nuclear Electronics and Computing - NEC'2017, September 28, Budva, Montenegro, 2017.
24. Status of Time Projection Chamber (TPC) for Multi-Purpose Detector (MPD) of NICA mega-project.
A. Bazhazhin on behalf of the TPC-MPD/NICA collaboration // 52nd Winter School of Perersburg Nuclear Physics Institute named by B.P.Konstantinov of National Research Centre “Kurchatov Institute”, Saint-Petersburg, Russia, February 26 – March 4, 2018.
25. Status of Time Projection Chamber (TPC) development for MPD NICA project.
A. Bazhazhin on behalf of the TPC-MPD/NICA collaboration // 24 Scientific conference of physics-students and young scientists, Association of physics-students and young scientists of Russia, Tomsk, Russia, March 31– April 7, 2018.
26. MPD/NICA TPC status (15.08.2018).
S.Movchan on behalf of the TPC-MPD/NICA collaboration // The XIV-th International School-Conference "The Actual Problems of Microworld Physics", Grodno, Belarus, August 12-24, 2018.
27. TPC assembly tolling and procedure.
A. Bazhazhin on behalf of the TPC-MPD/NICA collaboration // The XIV-th International School-Conference "The Actual Problems of Microworld Physics", Grodno, Belarus, 12-24 Aug., 2018.
28. Readout electronics for TPC detector in the MPD/NICA project.
S. Vereschagin on behalf of the TPC-MPD/NICA collaboration // Poster, RAD2018, June 6 – 22, Ohrid, Macedonia, 2018..
29. Status of the TPC for the MPD/NICA experiment.
A. Bazhazhin on behalf of the TPC-MPD/NICA collaboration // 53 Winter School of Perersburg Nuclear Physics Institute named by B.P.Konstantinov of National Research Centre “Kurchatov Institute”, Saint-Petersburg, Russia, March 2 – 7, 2019.
30. Статус некоторых узлов и вспомогательных установок для время-проекционной камеры (TPC) многоцелевого детектора (MPD) проекта NICA.
A. Bazhazhin on behalf of the TPC-MPD/NICA collaboration // 25th Scientific conference of physics-students and young scientists, Association of physics-students and young scientists of Russia, Luspy, Crimea, Russia, April 19-26, 2019.

31. Status of the TPC for the MPD/NICA experiment.

Bazhazhin A. on behalf of the TPC-MPD collaboration // 9th International Conference "Modern Problems of Nuclear Physics and Nuclear Technologies", Tashkent, Uzbekistan, September 24-27, 2019.

32. MPD/NICA TPC status (24.10.2019).

Presented by Sergey Movchan. Collaboration of TPC-MPD/NICA // III NICA days 2019 and IVth MPD Collaboration Meeting, Warsaw University of Technology, Faculty of Physics, Warsaw, Poland, October 21-25, 2019.

https://indico.cern.ch/event/802303/contributions/3614119/attachments/1934315/3204930/38_Movchan_TPC_status_fro_Warsaw_v03_23_10_2019.pdf

33. Time-projection chamber development for Multi-Purpose Detector of NICA project,

Stepan Vereschagin, on behalf of the TPC/MPD group Dubna, JINR // VCI2019 - The 15th Vienna Conference on Instrumentation, Vienna University of Technology, Venna, Austria, February 18-22, 2019.

https://indico.cern.ch/event/716539/contributions/3246145/attachments/1796077/2927947/Poster_VCI2019_Vereschagin.pdf

34. Test results of the SAMPA-based Front End Cards with Readout Chambers for the NICA TPC.

O. Fateev on behalf of the TPC/MPD group, LHEP, JINR // ISBN 978-1-7281-2574-9IEEE XXVIII International Scientific Conference Electronics - ET2019, Technical University of Sofia, Faculty of Electronic Engineering and Technologies, Bulgaria Delft University of Technology, the Netherlands, Sozopol, Bulgaria, September 16-18, 2019.

35. FRONT-END ELECTRONICS FOR TPC/MPD DETECTOR OF NICA PROJECT.

Stepan Vereschagin, on behalf of the TPC/MPD group, LHEP, JINR // The 27th International Symposium on Nuclear Electronics and Computing (NEC`2019), JINR, CERN, Budva, Becici, Montenegro, 2019.

https://indico.jinr.ru/event/738/session/16/contribution/115/material/slides/0.pdf

36. Front-End Electronics development status for TPC/MPD detector of NICA project.

S.Vereschagin on behalf of the TPC/MPD group // Poster, 51st meeting of the PAC for Particle Physics, Dubna, Russia, June 19, 2019.

37. MPD/NICA TPC status (25.02.2020).

Sergey Movchan on behalf of the TPC-MPD/NICA collaboration // International Conference "Instrumentation for Colliding Beam Physics" (INSTR20), Novosibirsk, Russia, February 24-28, 2020.

https://indico.inp.nsk.su/event/20/session/2/contribution/101/material/slides/0.pdf

38. Front-End Electronics development for TPC/MPD detector of NICA project.

Stepan Vereschagin on behalf of the TPC/MPD group, LHEP, JINR // International Conference "Instrumentation for Colliding Beam Physics" (INSTR20), Novosibirsk, Russia, February 24-28, 2020.

https://indico.inp.nsk.su/event/20/session/8/contribution/96/material/slides/0.pdf

TOF

The list of the International Conference Talks in 2017-2019

Participation in scientific events (international, invited report):

1. CREMLIN WP7 "Super c-tau factory workshop", Budker INP, Novosibirsk, Russia
TOF based on MRPC for MPD NICA, V. Babkin on behalf of the TOF group of the MPD collaboration., 2018

Participation in scientific events (international, oral report):

1. THE XIII WORKSHOP ON RESISTIVE PLATE CHAMBERS AND RELATED DETECTORS (RPC2016), Ghent University, Ghent, Belgium
Development of the MRPC for the TOF system of the MultiPurpose Detector., V.A. Babkin, S.N. Bazylev, M.G. Buryakov, P.O. Dulov, V.M. Golovatyuk, S.P. Lobastov, M.M. Rumyantsev, A.V. Schipunov, A.V. Shutov, I.V. Slepnev, V.M. Slepnev, A.V. Terletskiy, S.V. Volgin, 2016

2. International Session-Conference of the Section of Nuclear Physics of the Physical Sciences Department of the Russian Academy of Sciences "Physics of fundamental interactions" dedicated to 50th anniversary of Baksan Neutrino Observatory, Physical Sciences Department of the Russian Academy of Sciences, Nalchik, Russia
MultiPurpose Detector - MPD, V. Babkin on behalf of the MPD/NICA collaboration, 2017

3. The 2nd International School on Heterogeneous Computing Infrastructure NEC 2017, JINR LIT, NRC «Kurchatov Institute», TPU, The Institute of Cybernetics, Budva, Montenegro
MultiPurpose Detector - MPD, V. Babkin on behalf of the MPD/NICA collaboration., 2017

4. NICA days 2017, JINR, Warsaw, Poland
Time-of-Flight Identification System of the MPD and BM@N Experiments., V. Babkin, M. Rumyantsev, V. Golovatyuk, A. Dmitriev , M. Buryakov, P. Dulov, 2017

5. The first Collaboration meeting of the MPD and BM@N experiments at the NICA Facility, JINR, Dubna, Russia
Status of TOF, V. Babkin on behalf of the TOF group of the MPD collaboration., 2018

6. 2nd Collaboration meeting of the MPD and BM@N experiments at the NICA Facility, JINR, Dubna, Russia
MPD: TOF status, On behalf of the TOF group of the MPD collaboration, 2018

7. 3rd Collaboration meeting of the MPD and BM@N experiments at the NICA Facility, JINR, Dubnba, Russia
TOF construction status, V.A. Babkin on behalf of the TOF group of the MPD, 2019

8. III NICA days 2019 and IVth MPD Collaboration Meeting, Warsaw University of Technology, Faculty of Physics, Warsaw, Poland
Current status of the Time-of-Flight system of the MPD, V. Babkin on behalf of the TOF group of the MPD collaboration, 2019

9. International Conference "Instrumentation for Colliding Beam Physics" (INSTR20), Budker Institute of Nuclear Physics (BINP) and Novosibirsk State University (NSU), Novosibirsk, Russia, Novosibirsk, Russia
Time-of-flight system of the MultiPurpose Detector at NICA, V. Babkin on behalf of the TOF group of the MPD collaboration, 2020

Participation in scientific events (international, poster presentation):

Posters

1. Instrumentation for Colliding Beam Physics (INSTR17), Budker Institute of Nuclear Physics, and Novosibirsk State University,, Novosibirsk, Russia
Status of the Time-of-Flight system of the MPD, V. Babkin on behalf of the TOF group of the MPD collaboration, 2017

2. The European Physical Society Conference on High Energy Physics (EPS-HEP 2019), Department of Physics and Astronomy of Ghent University, Гент, Бельгия
Time-of-flight particles identification in the MultiPurpose Detector at NICA, V. Babkin, M. Buryakov, A. Dmitriev, V. Dronik, V. Golovatyuk, A. Kluev, S. Lobastov, A. Mudrokh, R. Nazhmudinov, A. Oleinik, M. Rumyantsev and K. Vokhmyanina, V. Babkin on behalf of the TOF group of the MPD collaboration, 2019

Participation in scientific events (Russian, invited report):

1. 22nd All-Russian Scientific Conference of Physics Students (VNKSF-22), Association of Physicist Students of Russia (ASF), Rostov-on-Don, Russia

The study of the properties of dense baryonic matter on the Multipurpose Detector MPD of the NICA accelerator complex at the High-Voltage Physics Institute of JINR, V.A. Babkin from the NICA Collaboration, 2016

Participation in scientific events (Russian, oral report):

1. 4th Meeting of the Nuclotron Beam Consumers, VBLHEP, JINR, Dubna, Russia

Test results of detectors for MPD and BM @ N on the MPD Test Channel installation. ", V.A. Babkin from the TOF MPD and BM @ N group, Report on the operation of the installation in the 52nd session of the Nuclotron., 2016

FFD

Publications in peer-reviewed journals

1. Fast detectors for the MPD/NICA time-of-flight system.

V. Babkin, S. Bazylev, O. Batenkov, P. Dulov, V. Golovatyuk, S. Lobastov, V. Petrov, M. Rumyantsev, A. Schipunov, A. Shutov, I. Slepnyov, V. Slepnyov, A. Veschikov, S. Volgin, V. Y и др., Bulgarian Chemical Communications, ISSN:0324-1130, 47, Special Issue-B, 215-221, 2015

2. Development and study of picosecond start and trigger detector for high-energy heavy ion experiments.

V.I. Yurevich, Nuclear Instruments & Methods in Physics Research A, A787, 308-311, 2015

3. Picosecond Cherenkov detectors for high-energy heavy ion experiments at LHEP/JINR.

V. I. Yurevich, O. I. Batenkov, Nuclear Instruments & Methods in Physics Research A, http://dx.doi.org/ 10.1016/j.nima.2015.12.049, 2016

4. Cherenkov and scintillation detectors with MCP-PMT and SiPM readout for MPD and BM@N experiments at JINR.

V.I. Yurevich, G.N. Agakichiev, S.V. Sergeev, D.N. Bogoslovski, V.Yu. Rogov, S.P. Lobastov, G.S. Averichev, V.V. Tikhomirov, A.A. Timoshenko, Nuclear Instruments & Methods in Physics Research A, Изд:Elsevier, 912, 294-297, 2018

5. Development of trigger and start detectors for experiments with high-energy heavy ions at the Joint Institute for Nuclear Research.

V. I. Yurevich, G. N. Agakichiev, S. V. Sergeev, D. N. Bogoslovski, S. P. Lobastov, V. Yu. Rogov, G. S. Averichev, V. V. Tikhomirov, A. A. Timoshenko, O. I. Batenkov, International Journal of Modern Physics:Conference Series, Изд:World Scientifiec, 48, 1860122 1-9, 2018

6. Beam Tests of Cherenkov Detector Modules with Picosecond Time Resolution for Start and L0 Trigger Detectors of MPD and BM@N Experiments.

V. I. Yurevich, O. I. Batenkov, G. N. Agakichiev, G. S. Averichev, V. A. Babkin, S. N. Basilev, D. N. Bogoslovsky, L. G. Efimov, S. P. Lobastov, I. A. Philippov, A. A. Povtoreyko, и др.,

Letters ECHAI (Письма в ЭЧАЯ), T.12, №6, C.778-785, 2015.

7. L0 trigger unit prototype for BM@N setup.

O.I. Batenkov, D.N. Bogoslovski, V.Y. Rogov, S.V. Sergeev, V.I. Yurevich, Письма в ЭЧАЯ, T.13, № 5, C.547-550, 2016.

Materials of scientific events (international)

Oral report:

1. The 2017 International Conference on Applications of Nuclear Techniques (CRETE17), Crete, Greece

Development of trigger and start detectors for experiments with high-energy heavy ions at the Joint Institute for Nuclear Research.

V. I. Yurevich, G. N. Agakichiev, S. V. Sergeev, D. N. Bogoslovski, S. P. Lobastov, V. Yu. Rogov, G. S. Averichev, V. V. Tikhomirov, A. A. Timoshenko, O. I. Batenkov, World Scientific, International Journal of Modern Physics: Conference Series, 48, 2017.

2. The 2019 International Conference on the Applications of Nuclear Techniques (CRETE19), Crete, Greece

Development of scintillation detectors with SiPM readout for the NICA project.

V. I. Yurevich , S. A. Sedykh, S. V. Sergeev, D. N. Bogoslovski, V. Yu. Rogov, V. V. Tikhomirov, N. A. Lashmanov, International Journal of Modern Physics: Conference Series, 2019 (in publication).

Poster Report:

3. 13th Pisa meeting for advanced detectors, INFN, La Biodola, Isola d`Elba, Italy.

Picosecond Cherenkov detectors for heavy ion experiments at LHEP/JINR, V.I. Yurevich, O.I. Batenkov, 2015

4. 54th International Winter Meeting on Nuclear Physics , Bormio, Italy.

Forward production of neutrons in fragmentation of high energy heavy nuclei, V. I. Yurevich, 2016.

5. The International Conference on New Developments In Photodetection – NDIP 17, Tours, France.

Cherenkov and scintillation detectors with MCP-PMT and SiPM readout for MPD and BM@N experiments at JINR, V.I. Yurevich, G. Agakichiev, S.V. Sergeev, D.N. Bogoslovskiy, V.Yu.

Rogov, G.S. Averichev, V.V. Tikhomirov, A.A. Timoshenko, Nuclear Instruments & Methods in Physics Research A, 912, P.294-297, 2017.

6. VIII International Youth Scientific School-Conference "Modern Problems of Physics and Technology", Moscow, Russia

RESEARCH OF THE NUCLEAR TRIGGER - NUCLEAR INTERACTIONS OF THE BM @ N EXPERIMENT USING THE GEANT4 + QGSM PROGRAM PACKAGE, 141-142, Modern Problems of Physics and Technology. VIII International Youth Scientific School-Conference, April 15-20, 2019. Book of abstracts. Part 2. Moscow. MEPhI. 2019, V.2, p.356, 2019.

7. The International Conference on Instrumentation for Colliding Beam Physics (INSTR20). Novosibirsk, Russia February 24–28, 2020.

Fast Interaction Trigger for MPD Experiment at NICA. V. I. Yurevich, S. A. Sedykh, S. V. Sergeev, V. Yu. Rogov, V. V. Tikhomirov, N. A. Lashmanov, A. A.Timoshenko, N. A. Kozlenko.

Electronic Publications:

1. L0 TRIGGER ELECTRONICS FOR THE BM@N SETUP IN RUN MARCH 2017.

Dmitriy Bogoslovski, Victor Rogov, Sergey Sergeev, Vladimir Yurevich, CEUR Workshop Proceedings, 2017.

2. Study of the trigger on nucleus-nucleus interactions for the BM@N experiment using a Geant4 + QGSM software package.

N. A. Lashmanov, S. A. Sedykh, V. I. Yurevich, Journal of Physics: Conference Series 1439 (2020) 012004 IOP Publishing doi:10.1088/1742-6596/1439/1/012004, 2020.

FHCal

1. A.Timoshenko et al., Forward hadron calorimeter **for MPD/NICA experiment**, **Nucl.Instrum.Meth. A936 (2019) 133-135,** DOI: 10.1016/j.nima.2018.10.068
2. A.Ivashkin et al., Determination *of* geometry of heavy ion collisions with forward fadron calorimeter (FHCal) at MPD/NICA. **EPJ Web of Conferences 204, 07002 (2019)** https://doi.org/10.1051/epjconf /201920407002.
3. A.Ivashkin et al., Compact segmented hadron calorimeter for detection of low energy spectators at MPD/NICA facility, **Nucl.Instrum.Meth. A958 (2020) 162**240 , https://doi.org/10.1016/j.nima.2019.05.081.
4. A.Strizhak and A.Ivashkin, Test of modules for Forward Hadron Calorimeter at MPD/NICA facility, **AIP Conference Proceedings 2163, 030013 (2019)**; https://doi.org/10.1063/1.5130099
5. N.Karpushkin, F.Guber and A.Ivashkin, Application of the Prony least squares method for fitting signal waveforms measured by sampling ADC, **AIP Conference Proceedings 2163, 030006 (2019)**; https://doi.org/10.1063/1.5130092

6. Study of nuclear fragmentation at MPD/NICA, M.B. Golubeva, A.P. Ivashkin, A.B. Kurepin (Moscow, INR). 2017. 4 pp. Published in **EPJ Web Conf. 138 (2017) 11001**
7. Forward hadron calorimeter at MPD/NICA M. Golubeva (Moscow, INR) et al.. 2017. 4 pp., Published in **J.Phys.Conf.Ser. 798 (2017) no.1, 012074**

8. V.Mikhaylov et at, Characterisation of SiPM radiation hardness for application in hadron calorimeters at FAIR, CERN and NICA, Published in **JINST 15 (2020) no.02, C02005** DOI: 10.1088/1748-0221/15/02/C02005
9. D. Finogeev et al., The Construction and Parameters of Forward Hadron Calorimeter (FHCAL) at MPD/NICA. Published in **KnE Energ.Phys. 3 (2018) 149-153** DOI: 10.18502/ken.v3i1.1737

Conferences

1. A.Ivashkin, Compact segmented hadron calorimeter for detection of low energy spectators at MPD/NICA facility, 15th Vienna conference on instrumentation, VCI-2019, Vienna, Austria, poster report.

2. N.Karpushkin, Application of the Prony least squares method for fitting signal waveforms measured by sampling ADC, the XXIII International Scientific Conference of Young Scientists and Specialists (AYSS-2019), Dubna, Russia, oral report.

3. A. Strizhak, Test of modules for Forward HadronCalorimeter at MPD/NICA facility, the XXIII International Scientific Conference of Young Scientists and Specialists (AYSS-2019), Dubna, Russia, oral report.

4. A.Izvestnyy, Performance of Forward Hadron Calorimeter at MPD/NICA, Fairness-2019, Genova, Italy, oral report.

5. A.Ivashkin and M.Golubeva, Study of energy distributions in FHCal, NICA days 2019, Warsaw, Poland, oral report.

6. A.Ivashkin and A.Strizhak, Status of FHCal, NICA days 2019, Warsaw, Poland, oral report.

7. P.Parfenov, Centrality Determination in Heavy-ion Collisions with MPD (NICA), NICA days 2019, Warsaw, Poland, oral report.

8. A.Ivashkin, Amplitude and time parameters of modules for hadron calorimeter at MPD/NICA, The International Conference "Instrumentation for Colliding Beam Physics" (INSTR-2020), Novosibirsk, Russia, poster report.

9. A.Timoshenko et al., *Forward* hadron *calorimeter* at MPD/NICA. 14th Pisa Meeting on Advanced Detectors, Italy. May 27- June 02, 2018. Poster

10. A.Ivashkin et al., Determination of *geometry* of heavy ion collisions with Forward Hadron Calorimeter (FHCal) at MPD/NICA. "XXIVth International Baldin Seminar on High Energy Physics Problems "Relativistic Nuclear Physics and Quantum Chromodynamics", September 17 - 22, 2018. Oral report

4. Recent results of MPD performance and feasibility study

During 2016-20 a comprehensive program of MPD detector performance and feasibility studies was carried out. The results of these studies have been presented at many international conferences and published in refereed journals. Below, we summarize several selected results of this activity.

4.1 MPD tracking and particle ID performance.

Monte-Carlo simulations aimed in the optimization of the MPD design and performance study have been performed within a dedicated software framework - MpdRoot [1]. It includes an interface to a number of heavy ion event generators (UrQMD, DCM-LAQGSM, PHSD and others) and to the GEANT3 or GEANT4 transport packages. To obtain a realistic detector responses very detailed description of all the elements for each of the subdetectors was provided.

The track and vertex reconstruction methods are based on the Kalman filtering technique [2]. The implementation details can be found in Ref. [3]. The efficiency of track reconstruction is plotted as functions of transverse momentum and pseudorapidity in Fig. 4.1.1 for charged particles with at least 15 measured points in the TPC. One can see that the reconstruction quality remains quite high within the pseudorapidity range of |□| < 1.5 (with the efficiency near 100% and decent resolution) for both the primary and secondary particles with the secondary track sample on the plots containing particles produced within 50 cm of the interaction point.

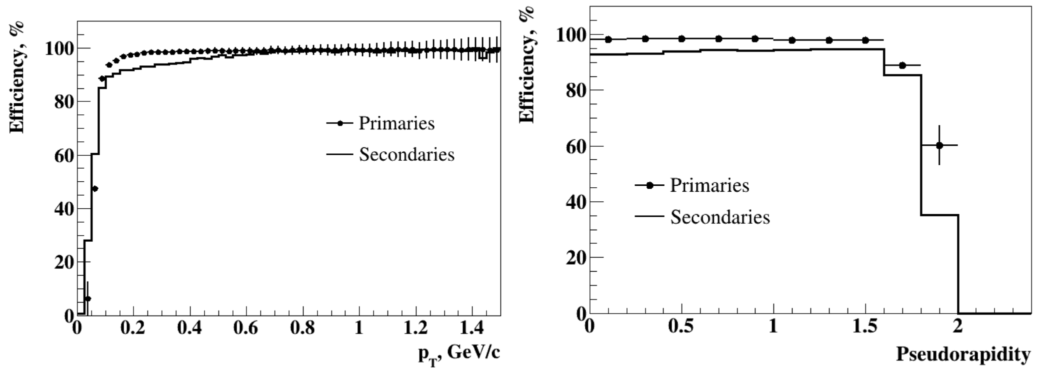

Fig. 4.1.1. Track reconstruction efficiency for particles with the number of measured points in the TPC (hits) greater than 14: (left) as a function of p_t for |□|<1.3; (right) as a function of □ $p_t > 0.1$ GeV/c. Symbols and lines present primary and secondary particles, respectively. Secondary particles were produced within 50 cm from the interaction point.

An important characteristic of a detector is its ability to reconstruct vertices. It depends on the achievable accuracy of track pointing to the production point. Figure 4.1.2 (left panel) demonstrates the precision of the reconstructed interaction point (along the beam direction) as a function of the charged track multiplicity in the event. As can be seen, the accuracy of the primary vertex reconstruction varies from about 150 to 700 □m in central and peripheral collisions, respectively.

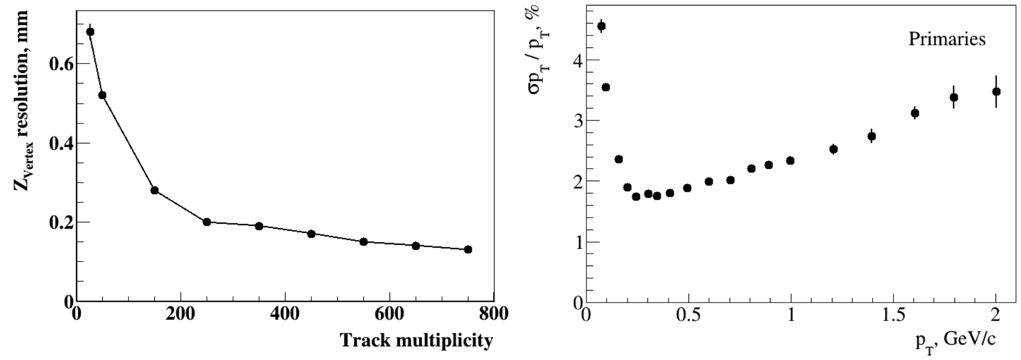

Fig. 4.1.2. Longitudinal position error of the reconstructed primary vertex as a function of track multiplicity.

The calculated relative momentum uncertainty $\Delta p_t/p_t$ is shown in Fig. 4.1.2 (right panel) as a function of p_t. It is seen from the plot that the resolution of less than 3% can be achieved at pt < 1.5 GeV/c.

Particle identification (PID) in the MPD experiment will be achieved by using the information about the energy losses (dE/dx) in the TPC gas and the time-of-flight from the TOF detector. For optimal performance the PID procedure should rely on a good knowledge of the detector characteristics such as the momentum dependence of the average energy loss as well as the variation of the <dE/dx> and mass-squared resolutions for each particle specie. Based on this information a vector of probabilities to be a particle of a particular sort is assigned to each track and the highest probability defines the particle specie. As was demonstrated in Ref. [4], the achieved accuracy of the energy determination using the truncation value of 30%, i.e. rejecting 30% of the hits with the largest energy deposit before obtaining the mean value, is 6-7% (see Fig.

4.1.3), allowing discrimination of charged pions from kaons up to momenta of 0.7 GeV/c and kaons from protons up to 1.1 GeV/c.

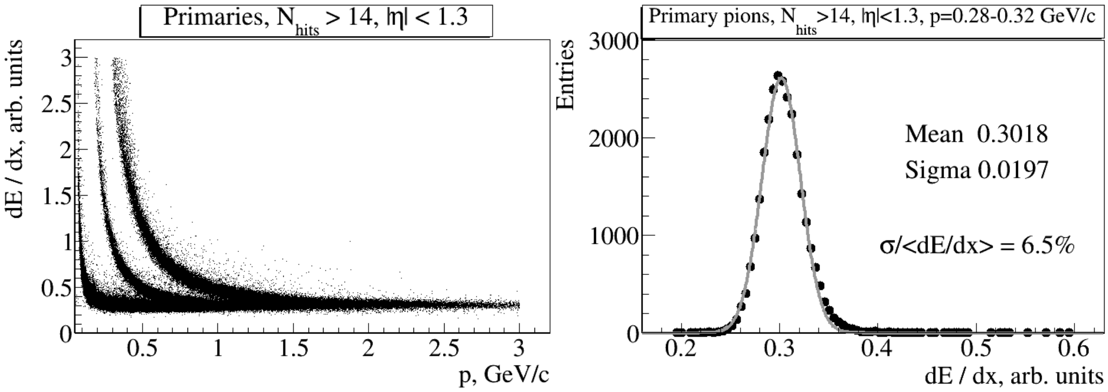

Fig. 4.1.3. (Left panel) Specific energy loss <dE/dx> as a function of momentum. (Right panel) Energy loss distribution for pions with p = 0.28-0.32~GeV/c fitted to the Gaussian.

The MPD TOF system (made of Multigap Resistive Plate Chambers - MRPCs) provides both the time and coordinate measurements with the accuracy of 80 ps and 0.5 cm, respectively. The MPD TOF performance for discrimination of hadrons in minimum bias Au+Au collisions at 9 GeV is demonstrated in Fig. 4.1.4, where on the left panel mass-squared as a function of the total momentum for positively charged hadrons from Au+Au collisions is shown, while on the right panel the fraction of the correctly identified particles is plotted as a function of momentum (dark symbols). This fraction is above 90% for protons and positively charged pions up to p=2.5 GeV/c, while the percentage of the cases with a wrong identification is below 10%. As can be see, we are able to identify charged kaons up to momentum of 1.7 GeV/c with an approximately 80% efficiency and 20% contamination at the PID limit. Making the selection criteria for kaons tighter, the achieved contamination level can be decreased further resulting in a lower value for the PID efficiency.

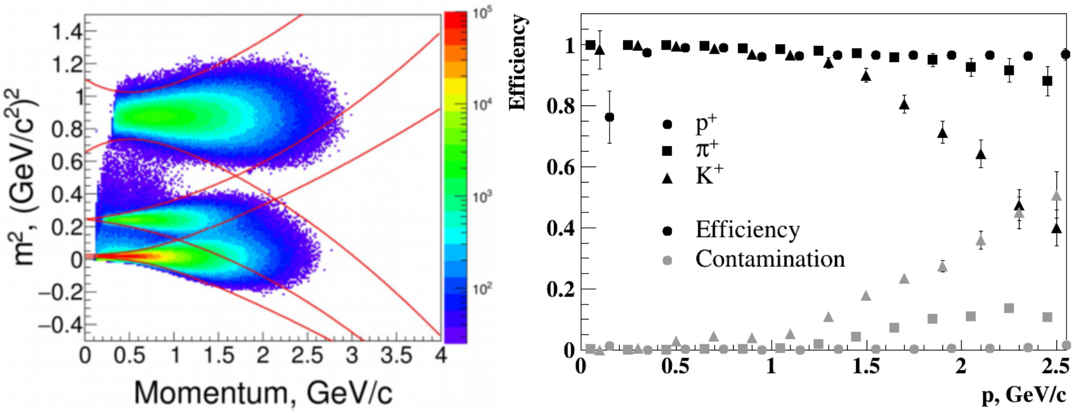

Fig. 4.1.4. (Left panel) Mass-squared as a function of the total momentum for positively charged hadrons from Au+Au collisions. (Right panel) Particle identification efficiency for positively charged hadrons (dark symbols) and a fraction of wrongly identified species (grey symbols) in Au+Au collisions at 9 GeV.

4.2. Bulk properties: hadron spectra, yield, and ratios

At NICA, a systematic study of particle yields and ratios will be performed as a function of collision energy, centrality, and kinematic variables (rapidity, transverse momentum, and azimuthal angle). The results of such a multi-parametric scan within the NICA energy range will be compared with the measurements in A+A (p+p) collisions at RHIC and SPS and to model calculations. For the discussed hadron measurements, the MPD detector will provide large and uniform acceptance for identified hadron species (see Fig. 4.2.1), allowing reconstruction of the total yields of mesons.

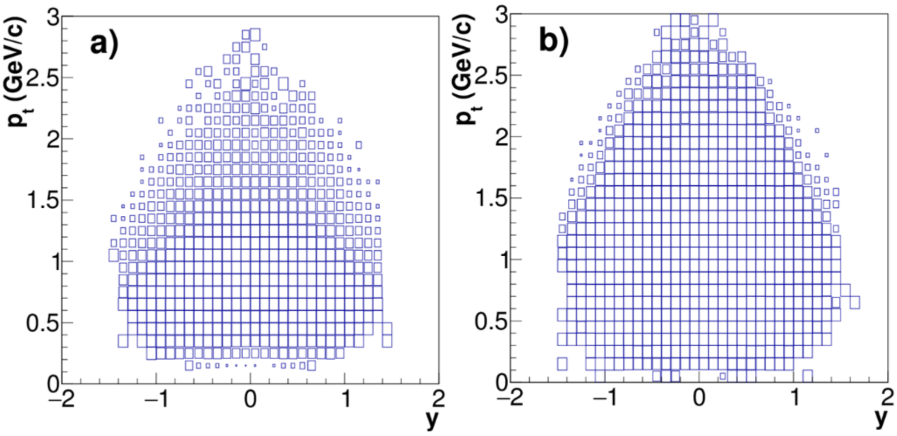

Fig. 4.2.1. The MPD phase space coverage in terms of rapidity and transverse momentum in Au+Au collisions at 8.8 GeV for identified K^+ (a) and π^+ (b). Note that the CM beam rapidity at this energy y_{beam}=2.2.

For the First-Day Physics period one among the probes will be the study of the production of charged pions and kaons near the maximum in the strangeness-to-entropy ratio (kaon-to-pion ratio has a non-monotonic behavior described as the "Horn" near the onset of the deconfinement phase transition at collision energy of about 8-9 GeV). In order to estimate the sensitivity of the proposed MPD detector setup to the potential phase transformation signals in dense nuclear matter via the ratio of strange hadrons to pions, a detailed Monte-Carlo study has been performed with the PHSD event generator, implementing both deconfinement and chiral symmetry restoration effects. We used data sets of 0-5% central Au+Au events at 5 collision energies (4, 6.2, 7.6, 8.8, 12.3 GeV) of 50 kEvents each. As an example, the invariant transverse momentum spectra of identified K+ in rapidity bins are shown in Fig. 4.2.2 (left panel). As can be seen, with the suggested MPD setup we are able to measure hadron spectra up to pT=2.5 GeV/c. In order to obtain the yield of hadrons in rapidity bins dN/dy, the reconstructed pT spectra need to be extrapolated into unmeasured transverse momentum regions exploiting information on the spectral shape. For this, spectra were tested against a hydrodynamically inspired blast-wave (BW) model (dashed lines indicate the fit results). The results on dN/dy as a function of rapidity for positively charged pions and kaons are plotted in Fig. 4.2.2 (right panel). The quoted uncertainties are the quadratic sums of the statistical and systematic uncertainties.

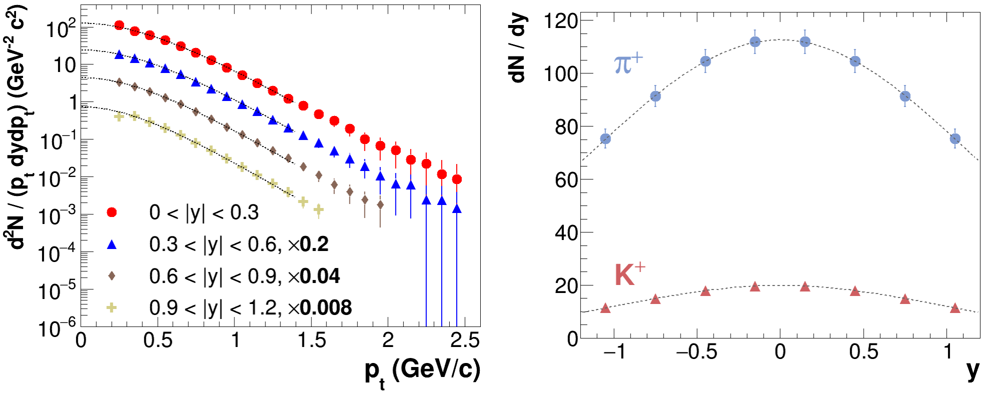

Fig. 4.2.2. (Left panel) Invariant pT spectra of K+ from central Au+Au at 8.8 GeV. The midrapidity spectra are drawn to scale; other distributions are scaled down by successive powers of five for clarity. Dashed lines indicate the used fit function. (Right panel) Rapidity distributions of □+ and K+ from central Au+Au collisions at 8.8 GeV.

From Gaussian fits (see dashed lines) we found, that from 70% to 90% of the final state phase space for the case of K+ (from 60% to 80% for the case of p+) can be covered by the measurements. Moreover, in the extrapolation to the full yield an error in the mean multiplicity of less than 4% for kaons and 3% for pions can be achieved. These errors were estimated as the difference between the value from the full integral of the rapidity spectra and the true multiplicity from the event generator. Thus, the suggested MPD setup has good perspectives for measuring hadroproduction in A+A collisions potentially unveiling the properties of phase transformation in dense baryon matter at NICA.

4.3. MPD performance for measurement of (multi)strange hyperon production

A PHSD data set of $2 \cdot 10^6$ Au+Au minimum bias events at 11 GeV was partitioned into four centrality bins in terms of the impact parameter interval. Hyperon reconstruction analysis was performed in several transverse momentum intervals of 0.5 GeV/c width. We reconstruct (multi)strange hyperons by combining charged tracks reconstructed in the TPC, first to select a V0-candidate (a characteristic topology of the two opposite charge daughter tracks) and then to match it with one of the secondary pion or kaon candidate. To guarantee that track combinations are associated with real decays we applied several selection criteria. To ensure that the charged tracks are secondary ones, distinct cuts were applied on the minimum value of the impact parameters to the primary vertex. In addition, a pair of tracks was rejected if the distance of closest approach (DCA) in space between the two opposite charged tracks was larger than a given value. Once the secondary vertex position was defined, only those falling within a fiducial region starting from a given distance from the main vertex were kept. Finally, the invariant mass was calculated under the proper hypothesis. The exact values of selection cuts were found by performing a multidimensional scan over the whole set of selection criteria with a requirement to maximize the invariant mass peak significance

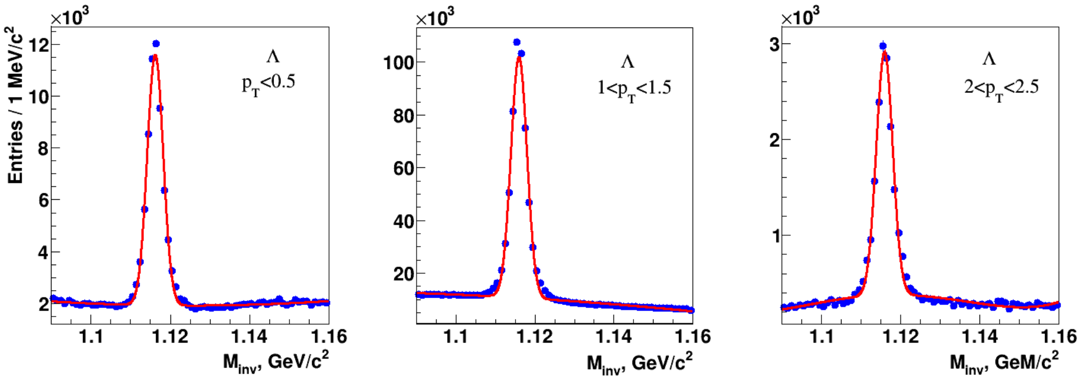

Fig. 4.3.1. Invariant mass spectra of charged pions and protons in several transverse momentum intervals.

In Fig. 4.3.1 invariant mass spectra of charged pion and proton candidates in several transverse momentum bins are shown. The raw yields of (anti)hyperons were then corrected for the detector acceptance and the reconstruction efficiency.

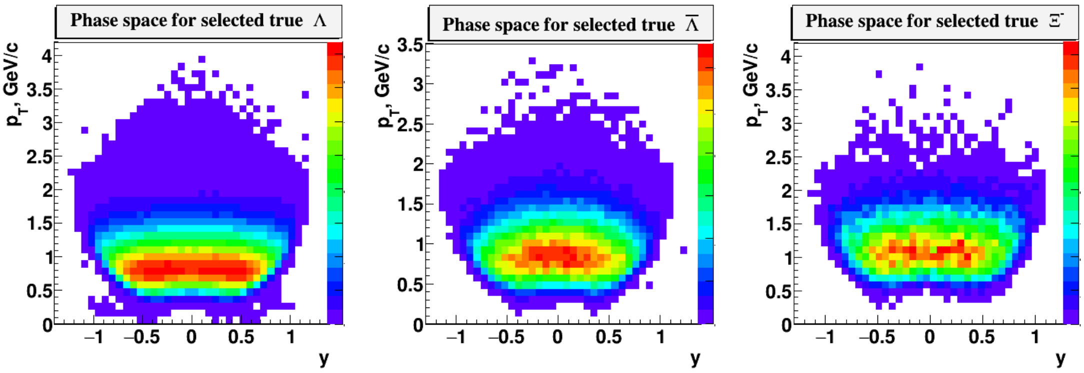

Fig. 4.3.2. MPD detector phase-space for hyperons in central Au+Au collisions at 11 GeV.

In Fig. 4.3.2, the MPD detector phase-space for hyperons is plotted in terms of rapidity and transverse momentum. As one can see, the proposed detector setup has a sufficient coverage to study both the longitudinal and transverse distributions of (anti)hyperons. As an example, in Fig. 4.3.3 the invariant transverse momentum spectra are shown for Lambda in the most central and the most peripheral centrality bin. The distributions were obtained after correcting the raw particle yields in pT bins by acceptance and efficiency factors determined as described above. The reconstructed yields are plotted with symbols and initial spectra from the model are drawn as histograms. As one can see, the difference between the initial spectra (from the model) and the reconstructed ones is small; the averaged point-by-point difference does not exceed 2%. The reconstructed data are indicated by symbols, while histograms represent the spectra from the model. The solid lines are the thermal fits used for the extrapolation.

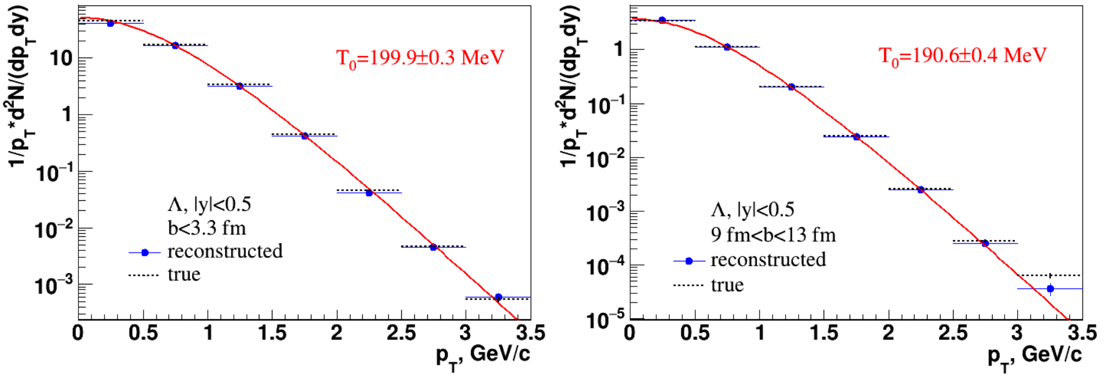

Fig. 4.3.3. The transverse momentum spectra of Lambda within the rapidity range (|y| < 0.5) for 0-5% (left panel) and 30-80% (right panel) central Au+Au collisions at 11GeV.

In order to evaluate expected statistics and phase space coverage at the experiment start-up for rare hyperons (for example anti-Omega) we used the PHSD minimum bias event sample of 8 million Au+Au at 11 GeV. The similar scanning procedure as for Lambda hyperons was used to find the significance maximum. The resulting invariant mass peak can be seen in Fig. 4.3.4 (left panel) along with the rapidity - transverse momentum phase space distributions for correctly reconstructed hyperons after final selection (right panel). One can see that the invariant mass peaks are clearly visible and the detector provides sufficient hyperon coverage at mid-rapidity.

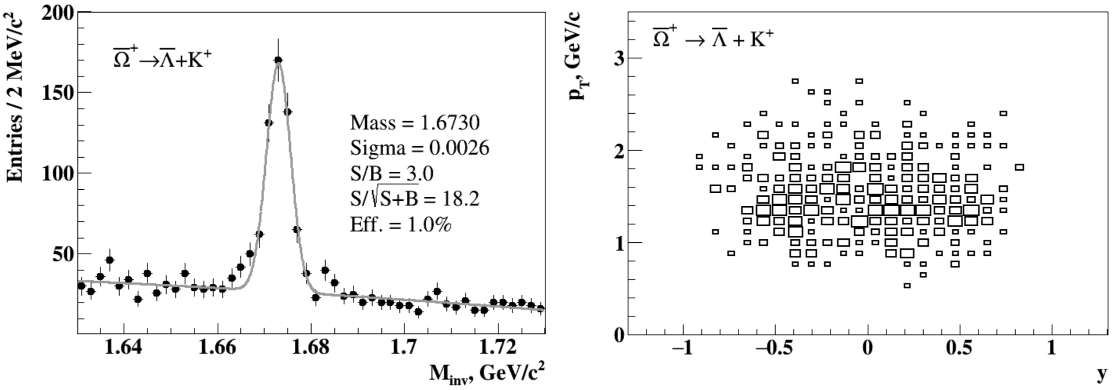

Fig. 4.3.4. Reconstructed invariant mass of anti-Omega (left) and its phase-space (right).

4.4. Direct and elliptic flow measurements at NICA/MPD

The anticipated performance of the MPD detector for the directed flow measurements of charged pions, kaons and protons is demonstrated in the Fig. 4.4.1. A sample of 5M minimum-bias Au+Au collisions at 5 GeV (left panel) and 11 GeV (right panel) simulated with UrQMD event generator was used for the analysis. The MPD detector response was simulated using GEANT4 toolkit and the resulting signals from the detector subsystems were used as input information for the full reconstruction procedure, which includes the realistic particle identification in TOF and TPC detectors (|η|<1.5) of MPD. The first order event plane was reconstructed using the energy deposition of particles detected in the forward hadronic calorimeters (FHCaL), located at (2 < | η |< 5).

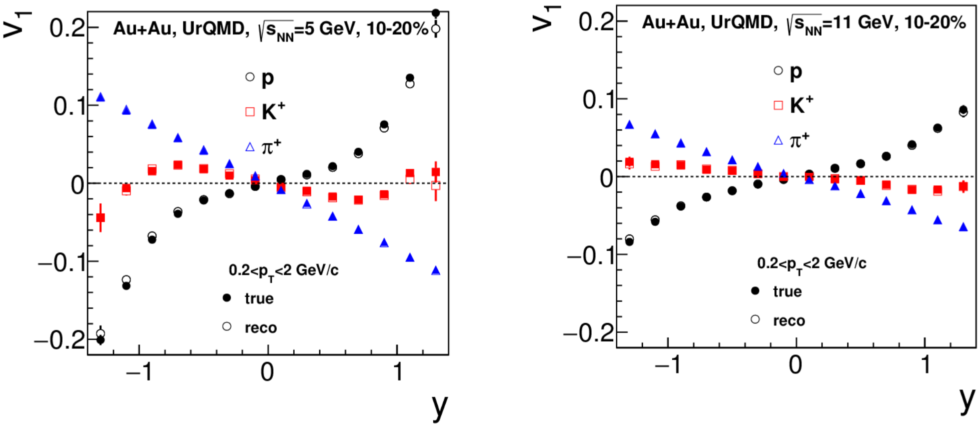

Fig. 4.4.1. Directed flow v_1 for charged pions, kaons and protons as a function of rapidity for Au+Au collisions at 5 GeV (left) and 11 GeV (right). The results from the UrQMD model are marked as true, and the ones from the full reconstruction procedure are marked as reco.

As know from existing experimental data, the excitation function of the directed and elliptic flow from mid-central Au+Au collisions indicate a strong non-monotonic behavior at energies of accelerator facility NICA, thus, the high-statistics differential measurements of v_n as a function of centrality, pT, rapidity for different particle species anticipated from the MPD expected to provide the valuable information about the properties of strongly interacting matter in this domain of QCD phase diagram.

4.5. Study of electron-positron pairs in A+A collisions at NICA/MPD

A detailed description of the analysis procedure and results can be found in Ref. [5]. Experimental study of dileptons in heavy-ion collisions is a challenging task, because of a huge combinatorial background of uncorrelated lepton pairs from the Dalitz decays of π^0 and γ-γ conversions. The main goal of this study was to investigate MPD detector performance for low-mass dilepton measurements in terms of hadron suppression factor, signal-to-background ratio and invariant mass resolution. We used in this study central (0-3 fm) Au-Au collisions at the center-of-mass energy of 7 GeV from the UrQMD generator in combination with the cocktail of vector mesons from the Pluto event generator. The used detector set-up includes the Time Projection Chamber (TPC), Time-Of-Flight system (TOF) and Electromagnetic Calorimeter (EMC) covering the pseudorapidity range $|\eta|<1.2$. The particles were transported through the detector by the Geant 3.21 code, the track reconstruction was based on the Kalman filtering technique. All the reconstructed in the TPC tracks were then extrapolated to the TOF detector and matched with TOF hits. The efficiency of track matching with TOF was found to be of about 90% at $p_T>0.4$ GeV/c, and the transverse momentum resolution appeared to be better than 3% for tracks with pT below 1 GeV/c. Electron identification was achieved by using combined information about the specific energy loss dE/dx from TPC, time-of-flight from TOF and E/p from EMC. The achieved overall hadron rejection factor was about 3200. The conversion pairs were rejected by a cut, making use of the fact that the magnetic field is orthogonal to the dilepton's momenta plane. This selection was complemented by a cut on the radial position of the production point. In addition, in order to suppress electrons (positrons) from the conversion further we applied a transverse momentum cut: 0.2<pT<2 GeV/c.

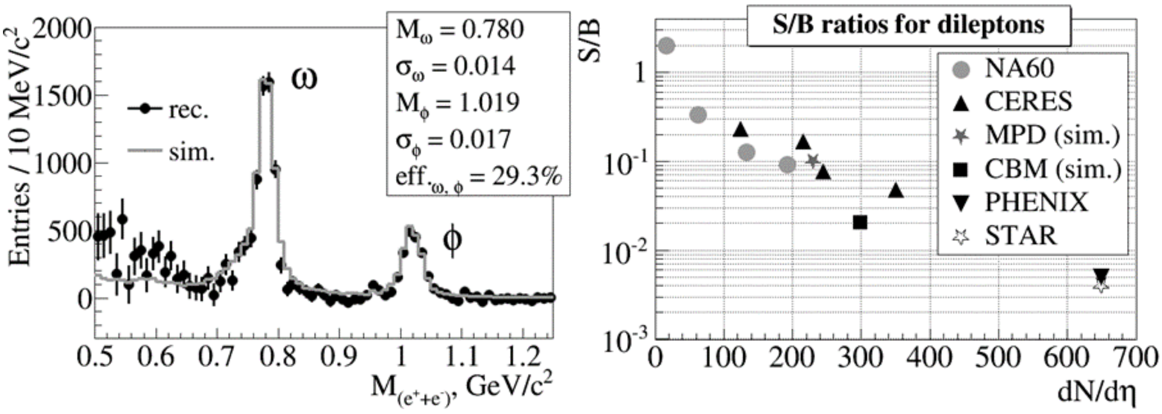

Fig.4.5.1.(Left) Background-subtracted invariant mass distributions of electron-positron pairs from central Au+Au collisions at MPD.(Right) Signal-to-Background (S/B) ratio from heavy-ion experiments as a function of total charged multiplicity.

In Fig. 4.5.1 (left panel) a background-subtracted invariant mass distributions of electron-positron pairs in the pseudorapidity window |η|<1.0 is plotted. A rough estimate of invariant mass resolution of the MPD setup was made by fitting the dileptons spectra at the poles for vector mesons: RMS of 14 and 17 MeV were obtained for the omega- and phi-meson pole, respectively. The overall (integrated over the invariant mass window of 0.2-1.5 GeV/c^2) signal-to-background ratio was found to be close to 10%. The obtained results for the signal-to-background ratio are shown in Fig. 4.5.1 (right panel) along with the published data from other experiments. The expected parameters of the MPD setup are among the best over the world.

REFERENCES

[1] https://git.jinr.ru/nica/mpdroot

[2] Fruhwirth, R., Nucl. Instr. and Meth. A 262 (1987) 444.

[3] Gertsenberger K., Merts S., Rogachevsky O. and Zinchenko A., Eur. Phys. J. A 52 (2016) 214.

[4] Kolesnikov V., Mudrokh A., Vasendina V. and Zinchenko A., Phys. Part. Nucl. Lett. Vol. 16 (2019) 6.

[5] V. Vasendina et al. Phys. Part.Nucl. Lett. 2013, V. 10, pp. 769-777.

5.0. Milestones of MPD assembling in 2020-2021

Year 2020

1. March 1st - - MPD Hall and pit are ready to store and unpack Yoke parts
2. April – May - Magnet Yoke is assembled for alignment checks
3. June - Solenoid is ready for transportation from ASG (Italy)
4. July - August - Solenoid is in Dubna
5. August-Sept - Assembling of Magnet Yoke and Solenoid at JINR
6. July- Sept - Preparation for switching on the Solenoid
7. Oct-Nov - Magnetic Field measurement
8. December - Installation of Support Frame.

Year 2021

9. Jan - Jul 2021 - Installation of subsystems, Electronics Platform, Cabling
10. Aug 2021 -Commissioning
11. Oct 2021 -Readiness for Cosmic Ray tests

6.0. Funding

Cost Estimate in 2020-2025

	Expenditure items	Full cost	1st year (2021)	2d year (2022)	3d year (2023)	4th year (2024)	5th year (2025)
	Direct expenses for the Project						
1	Nuclotron, Collider, hours	10250	0	250	2500	3500	4000
2	Computing (processor* hour), mln.	165,6	10,8	18,0	28,8	50,4	57,6
3	Computing communication						
4	Technical Design, hours	40000	10000	10000	10000	5000	5000
	Experimental Workshop,hours						
6	Materials k$	17750	3500	2250	2300	3500	6200
7	Equipment k$	6108	1203	945	640	1900	1420
8	Payment for research carried out under contracts k$	2650	750	550	550	400	400
9	Travel allowance, including: k$	950	200	180	180	190	200
	в т.ч.						
	а) non-rouble zone countries	660	120	120	120	150	150
	б) rouble zone countries	140	30	30	30	25	25
	в) protocol-based	140	30	30	30	25	25
	Total direct expenses	27458	5653	3925	3670	5990	8220